2007-03

Study of the utility of NWP forecast guidance and simple ocean modeling as a tool for planning during reactive situations

Jones, Robert David.

Monterey, California. Naval Postgraduate School

NAVAL POSTGRADUATE SCHOOL

MONTEREY, CALIFORNIA

THESIS

STUDY OF THE UTILITY OF NWP FORECAST GUIDANCE AND SIMPLE OCEAN MODELING AS A TOOL FOR PLANNING DURING REACTIVE SITUATIONS

by

Robert David Jones

March 2007

Thesis Advisor:	Peter S. Guest
Second Reader:	Timothy P. Stanton

THIS PAGE INTENTIONALLY LEFT BLANK

REPORT DOCUMENTATION PAGE		Form Approved OMB No. 0704-0188

1. AGENCY USE ONLY *(Leave blank)*	2. REPORT DATE	3. REPORT TYPE AND DATES COVERED
	March 2007	Master's Thesis

4. TITLE AND SUBTITLE Study of the Utility of NWP Forecast Guidance and Simple Ocean Modeling as a Tool for Planning During Reactive Situations	5. FUNDING NUMBERS
6. AUTHOR(S) LCDR Robert David Jones, USN	
7. PERFORMING ORGANIZATION NAME(S) AND ADDRESS(ES) Naval Postgraduate School Monterey, CA 93943-5000	8. PERFORMING ORGANIZATION REPORT NUMBER
9. SPONSORING /MONITORING AGENCY NAME(S) AND ADDRESS(ES) N/A	10. SPONSORING/MONITORING AGENCY REPORT NUMBER

11. SUPPLEMENTARY NOTES The views expressed in this thesis are those of the author and do not reflect the official policy or position of the Department of Defense or the U.S. Government.

12a. DISTRIBUTION / AVAILABILITY STATEMENT	12b. DISTRIBUTION CODE
Approved for public release; distribution is unlimited.	A.

13. ABSTRACT (maximum 200 words)

The utility of using a numerical weather prediction (NWP) forecast model as an input to a simple ocean model for planning during reactive situations is studied. An oceanographic experiment called the Maud Rise Nonlinear Equation of State Study (MaudNESS) was conducted from June to September of 2005 over the Maud Rise in the eastern Weddell Sea. Archived Antarctic Mesoscale Prediction System (AMPS) Polar MM5 forecast fields from MaudNESS were compared to observed conditions during MaudNESS. AMPS was found to have problems with cloud and moisture parameters, but represented the overall synoptic situation. AMPS forecast and observed forcing fields (as well as increased values for both) were input into a simple one dimensional ocean model at three locations in the Maud Rise area of differing stability. The ocean model was found to have good utility as a planning tool for short term reactive situations where a high degree of accuracy is not needed.

14. SUBJECT TERMS Maud Rise Nonlinear Equation of State Study, MaudNESS, Antarctic Mesoscale Prediction System, AMPS, Polar MM5, PMM5	15. NUMBER OF PAGES 137
	16. PRICE CODE

17. SECURITY CLASSIFICATION OF REPORT	18. SECURITY CLASSIFICATION OF THIS PAGE	19. SECURITY CLASSIFICATION OF ABSTRACT	20. LIMITATION OF ABSTRACT
Unclassified	Unclassified	Unclassified	UL

NSN 7540-01-280-5500 Standard Form 298 (Rev. 2-89)
Prescribed by ANSI Std. 239-18

THIS PAGE INTENTIONALLY LEFT BLANK

Approved for public release; distribution is unlimited

STUDY OF THE UTILITY OF NWP FORECAST GUIDANCE AND SIMPLE OCEAN MODELING AS A TOOL FOR PLANNING DURING REACTIVE SITUATIONS

Robert David Jones
Lieutenant Commander, United States Navy
B.S., University of Idaho, 1994

Submitted in partial fulfillment of the
requirements for the degree of

MASTER OF SCIENCE IN METEOROLOGY AND PHYSICAL OCEANOGRAPHY

from the

NAVAL POSTGRADUATE SCHOOL
March 2007

Author: Robert David Jones

Approved by: Peter S. Guest
Thesis Advisor

Timothy P. Stanton
Second Reader

Philip A. Durkee
Chairman, Department of Meteorology

THIS PAGE INTENTIONALLY LEFT BLANK

ABSTRACT

The utility of using a numerical weather prediction (NWP) forecast model as an input to a simple ocean model for planning during reactive situations is studied. An oceanographic experiment called the Maud Rise Nonlinear Equation of State Study (MaudNESS) was conducted from June to September of 2005 over the Maud Rise in the eastern Weddell Sea. Archived Antarctic Mesoscale Prediction System (AMPS) Polar MM5 forecast fields from MaudNESS were compared to observed conditions during MaudNESS. AMPS was found to have problems with cloud and moisture parameters, but represented the overall synoptic situation. AMPS forecast and observed forcing fields (as well as increased values for both) were input into a simple one dimensional ocean model at three locations in the Maud Rise area of differing stability. The ocean model was found to have good utility as a planning tool for short term reactive situations where a high degree of accuracy is not needed.

THIS PAGE INTENTIONALLY LEFT BLANK

TABLE OF CONTENTS

LIST OF FIGURES

THIS PAGE INTENTIONALLY LEFT BLANK

LIST OF TABLES

ACKNOWLEDGMENTS

First and foremost, I would like to thank my thesis advisor, Professor Peter Guest of the Naval Postgraduate School Meteorology Department, for allowing me to use and modify several of his programs, and for guidance and direction throughout this process. Next, I would like to thank Dr. Miles McPhee of McPhee Research Company for allowing me the use of his 1-D ocean model, as well as guidance and instruction on its operation. Also, thanks to Professor Timothy Stanton and Professor William Shaw of the Naval Postgraduate School Oceanography Department, for assistance in selecting CTD locations and sanity checking my ocean results, and to Professor Arlene Guest of the Naval Postgraduate School Oceanography Department for her MATLAB expertise and assistance. Finally I would like to thank Mr. Kevin Manning of the Mesoscale and Microscale Meteorology Division at the National Center for Atmospheric Research for his knowledge and guidance with regards to the Antarctic Mesoscale Prediction System.

THIS PAGE INTENTIONALLY LEFT BLANK

I. INTRODUCTION AND BACKGROUND

The purpose of this research was to explore the feasibility of inputting numerical weather prediction (NWP) model forecast data into a simple ocean model, and then using the results of the ocean model in a reactive situation (best placement of a research vessel for investigating a desired oceanographic event, or best placement of fleet assets during an anti-submarine warfare (ASW) prosecution).

The opportunity to conduct this research came after the conclusion of the Maud Rise Nonlinear Equation of State Study (MaudNESS). MaudNESS took place during June to September 2005 (Southern Hemisphere winter season) in the eastern Weddell Sea (see Figure 1) in the vicinity of the Maud Rise (a seamount in the eastern Weddell Sea). The seamount rises from the seafloor (at a depth of approximately 5000 meters) to approximately 1600 meters below the surface of the ocean, and is approximately 100 kilometers in diameter. Muench et al. (2001) describe an isolated column of water partially trapped over the Maud Rise (resulting from impingement of combined Weddell Sea Warm Deep Water (WDW) and Circumpolar Deep Water (CDW)) which is characterized as a Taylor column. The Taylor column is colder, less saline, and slightly denser than surrounding waters, and tends to block horizontal flow over the Maud Rise. They describe a "halo" around the Maud Rise (ring shaped closed circulation about the Rise of relatively warm and saline combined WDW and CDW), which is the result of the regional southwestward flow being accelerated around the periphery of the Taylor column. Surrounding regional flow then continues southwestward playing a role in the formation of a warm pool southwest of the Maud Rise.

The area around the Maud Rise has been known to be the site of formation for large polynyas. The Weddell Polynya formed there in the mid 1970's and persisted for several seasons, with cooling effects on WDW lasting for at least a decade. Another polynya was seen in satellite imagery late in the winter season of 1994. WDW directly feeds Antarctic Deep Water (AADW) which is extremely important to global

thermohaline structure, therefore potentially significantly altering global deep water production.

It is believed that thermobaricity (dependence of thermal expansion coefficient of seawater on pressure), cabbeling (dependence of thermal expansion coefficient of seawater on temperature), and other nonlinearities in the equation of state for seawater play an important role as preconditioners for deep convection to occur. In the case of the area around the Maud Rise, this deep convection is sometimes strong enough to counteract the stabilizing effect of buoyancy flux from ice melt (positive salinity flux). McPhee states in the MaudNESS cruise report (obtained from http://fish.cims.nyu.edu /project_maudness/field_campaign.html) that:

> The Maud Rise Nonlinear Equation of State Study (MaudNESS) was developed to investigate upper ocean mixing in the low-stability regime found in the Maud Rise region.

Stanton describes on his website (http://www.oc.nps.navy.mil/~stanton/thermo /Maudness/IntroductionMain.html) "the objectives of the experiment is to answer two sets of questions:

> 1.) What are the mechanisms by which nonlinearities in the equation of state work to break down the stratification of the Weddell Sea near Maud Rise? What are the relative roles of thermobaricity, cabbeling, and other NES issues? We will address these questions through detailed measurements of the small scale mixing processes in the upper ocean near Maud Rise and high resolution modeling of these processes. The goal is to produce parameterizations suitable for larger scale numerical models, and
>
> 2.) How do the ocean circulation, ice and atmospheric forcing act to modulate and localize these processes? We will address this question by measuring the regional circulation and its variability near Maud Rise and by regional modeling of this circulation which incorporates the mixing parameterizations".

During the MaudNESS deployment aboard the Research Vessel Ice Breaker (RVIB) Nathaniel B. Palmer, Antarctic Mesoscale Prediction System (AMPS) NWP

model forecast data were used in a simple ocean model to attempt to locate areas of possible deep convection. For the first time, this ocean model output was used as a planning tool for ship location and experimental purposes. Unfortunately, no deep convection was encountered during the MaudNESS deployment, as the Antarctic winter in 2005 was much milder than normal.

This study was completed using archived AMPS data, ship observation data, and various seawater temperature and salinity profiles obtained during MaudNESS. Section II compares AMPS model output to observed conditions, both through time series and statistical analysis. Section III employs AMPS forecast, observed conditions, and variations of both as input to a simple one dimensional ocean model.

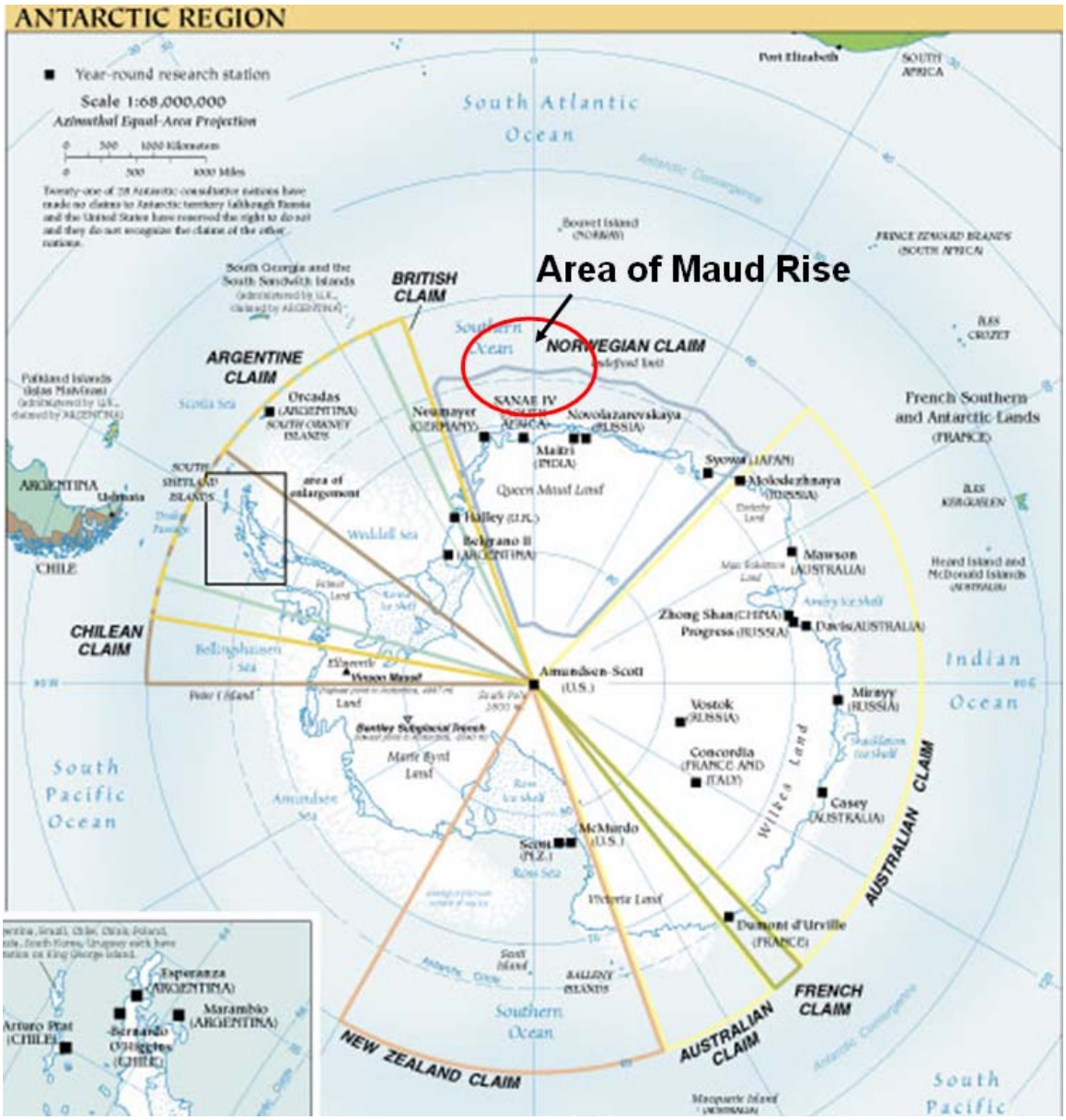

Figure 1. Antarctic region with Maud Rise area highlighted (After: https://www.cia.gov/cia/publications/factbook/reference_maps/antarctic.html).

II. ATMOSPHERIC MODEL VERSUS OBSERVATIONS

A. AMPS PMM5 NUMERICAL WEATHER PREDICTION MODEL

The numerical weather prediction (NWP) forecast model used during the MaudNESS deployment was the Antarctic Mesoscale Prediction System (AMPS). AMPS utilizes a polar version of the Pennsylvania State University-National Center for Atmospheric Research (NCAR) fifth generation mesoscale model (MM5). The MM5 was modified for polar environments by the Polar Meteorology Group of the Byrd Polar Research Center at Ohio State University. Significant modifications made include improvements to cloud-radiation interaction, modified explicit ice phase microphysics, optimized boundary layer turbulence parameterization, sea ice surface type, and improved treatment of heat transfer through snow and ice surfaces.

AMPS is initialized twice daily (00Z and 12Z) at the Mesoscale and Microscale Meteorology (MMM) Division of NCAR. The AMPS model is currently run in six domains (Figure 2). AMPS model data used on the MaudNESS deployment was from domain two, which at the time was run at a slightly coarser resolution of 30 kilometers. The model employs a terrain following staggered vertical grid, with thirty-two full sigma levels and thirty-one half sigma levels (half sigma levels are defined half way between full sigma levels). The lowest half sigma level is approximately thirteen meters above the surface (value used for bulk method used in this paper). The initial boundary conditions are driven by the National Center for Environmental Prediction's (NCEP) Global Forecasting System (GFS). Bromwich et al. (2005) state that:

> The observations available for assimilation include reports from radiosondes, surface SYNOP reports, automatic weather station (AWS) observations, ship reports, and buoys. Satellite-derived cloud-track winds are also assimilated in the 90-km grid. The system ingests sea ice data daily from the National Snow and Ice Data Center for its fractional sea ice depiction.

Radiosonde data obtained during MaudNESS were received by MMM for assimilation into AMPS. It is unknown, however, if any data were missed or discarded through error checking procedures (Manning, 2007, personal communication).

In May 2004 Three Dimensional Variational Data Assimilation (3DVAR) became the default analysis technique for AMPS MM5 initialization.

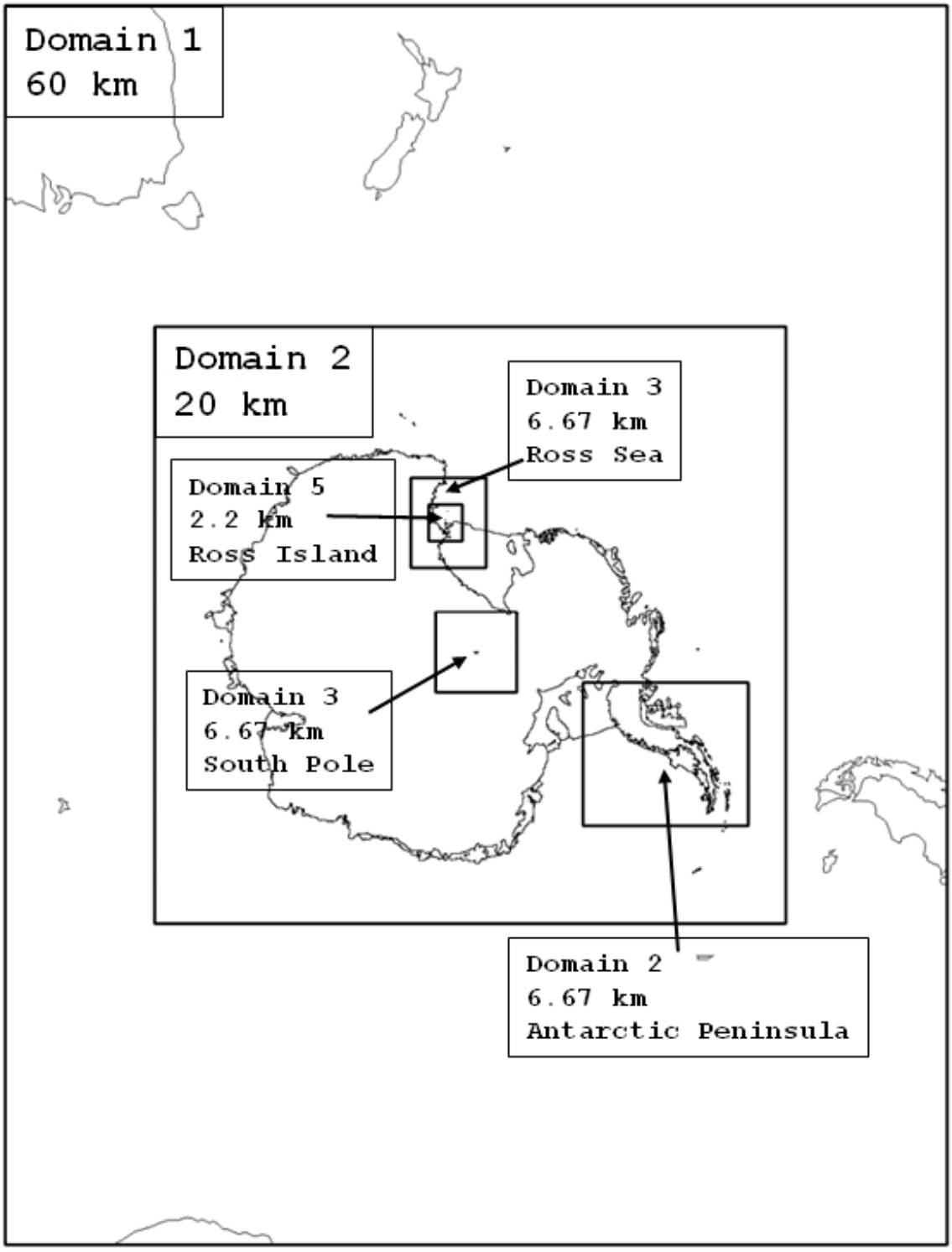

Figure 2. AMPS domains and horizontal resolutions. (After: http://www.mmm.ucar.edu/rt/mm5/amps/, 2007)

B. OBSERVATIONAL WEATHER DATA

The following shipboard meteorological data was collected every second, and averaged over ten second intervals:

-Port and starboard wind speed (maximum, minimum, and average)

-Port and starboard wind direction and standard deviation

-Temperature, degrees Celsius, maximum and minimum

-Relative humidity, single sample point, maximum and minimum

-Barometric pressure (a five millibar bias was added to all observed surface pressure values due to instrument error. This error was verified by rawinsonde data).

-Precision Spectral Pyranometer (PSP) (short wave radiation)

-Precision Infrared Radiometer (PIR) (long wave radiation

In addition, long wave and short wave radiation was measured using Eppley PIR and PSP sensors from the aft center of the helicopter deck (more accurate than ship PSP and PIR sensors, as they were cleaned and cleared of salt and ice daily). The sensors were mounted on gimbels so that they were level to approximately two degrees at all times. Data were collected every second and averaged into one minute records. Rawinsondes were also launched at a minimum of twice daily to collect upper air atmospheric profiles.

C. COMPARISONS AND STATISTICS BETWEEN MODELED AND OBSERVED WEATHER DATA

In order to achieve the stated purpose of this research, it was first necessary to determine how well the AMPS model performed. This was achieved by comparing archived AMPS model data with observational data gathered during the MaudNESS deployment. To ensure complete overlap between AMPS and observational data, the time period of comparison was limited to 1200Z 30 July 2005 to 1200Z 10 September 2005 (Julian dates 211.5 to 253.5). During this time period the Research Vessel entered

the ice on 30 July 2005, began ice egress on 4 September 2005 (Julian day 247) and exited the ice on 8 September 2005 (Julian day 251).

The 12Z model run was sent to the Research Vessel daily and included forecasts in three hour time steps out to 120 hours. For this paper, continuous AMPS time series were created by combining daily forecast data beginning at 1200Z (time zero) and ending at 0900Z the following day (time twenty-one). Ship meteorological data were collected every second and averaged over a ten second interval. For the chosen period of comparison this resulted in approximately 360 AMPS data points and almost 65,000 observational data points. Using a simple MATLAB routine, observational data were merged with AMPS data (by Julian date) to provide a direct comparison between the two. Parameters chosen for comparison include surface pressure, near surface air temperature, relative humidity, specific humidity, wind speed and direction, downwelling long wave radiation, downwelling short wave radiation, latent heat flux, and sensible heat flux.

Time series plots were then created for meteorological parameters, radiation, and heat fluxes for the entire period and weekly. Scatter plots were created comparing observed versus AMPS data for correlation analysis.

For each parameter, a differential value was obtained by subtracting observation data values from AMPS model data values, and plotted as a distribution density. Statistical parameters such as minimum, maximum, mean, median, and root mean squared (RMS) error were calculated for AMPS data, observation data, and the differential data. In addition, correlation coefficient (R) and correlation coefficient squared (R^2) were calculated for the differential data.

1. Surface Pressure

AMPS surface pressure was found to agree with observational relatively well. Time series plots (Figures 3 and 4) show AMPS over forecasting surface pressure on Julian days 220 to 223 and under forecasting surface pressure after Julian day 250. This can also be clearly seen on a scatter plot of observed versus AMPS surface pressure (Figure 5) and a differential distribution plot (Figure 6).

Basic statistics for AMPS and observation surface pressure are shown in Table 1. Statistics run on differential values (AMPS minus observation) are shown in Table 2. Evaluation of statistical and correlation data indicate that AMPS was handling the synoptic pattern relatively well.

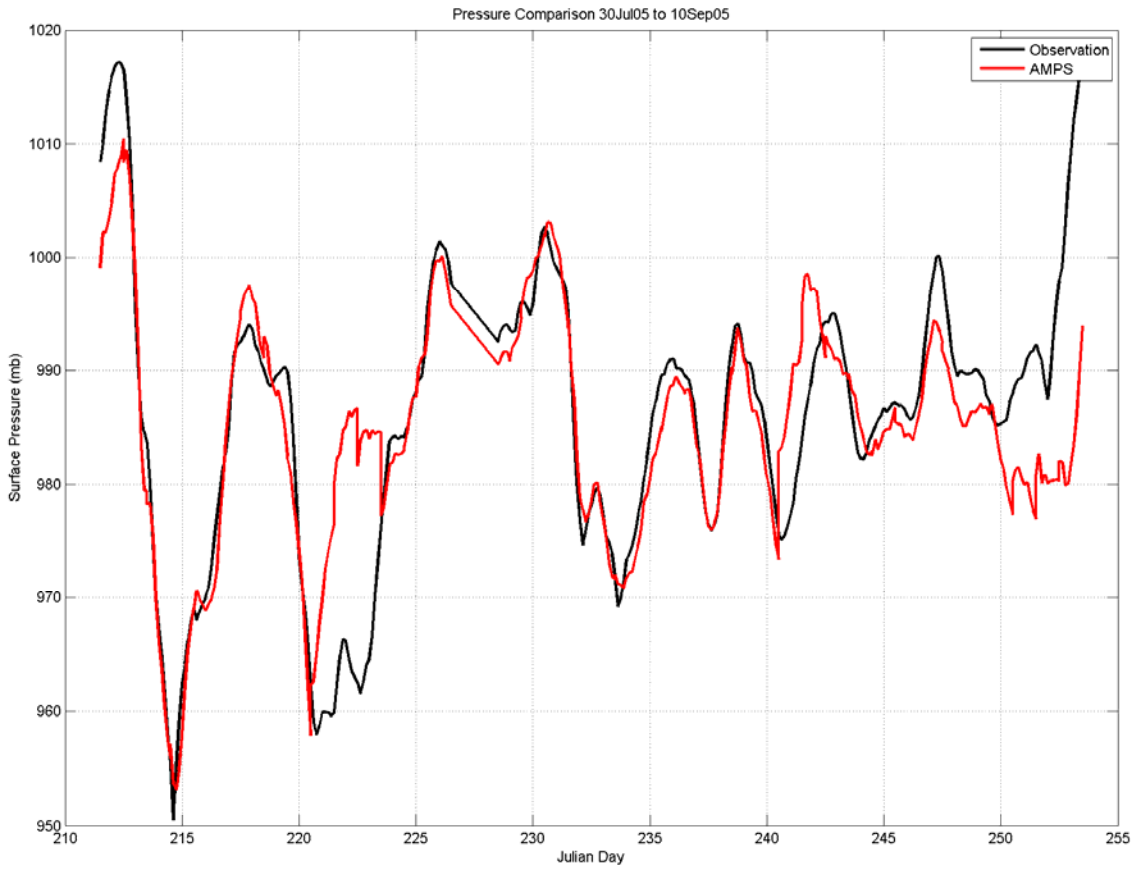

Figure 3. Surface pressure time series 30 July 2005 to 10 September 2005. Black line is observational data and red line is AMPS data.

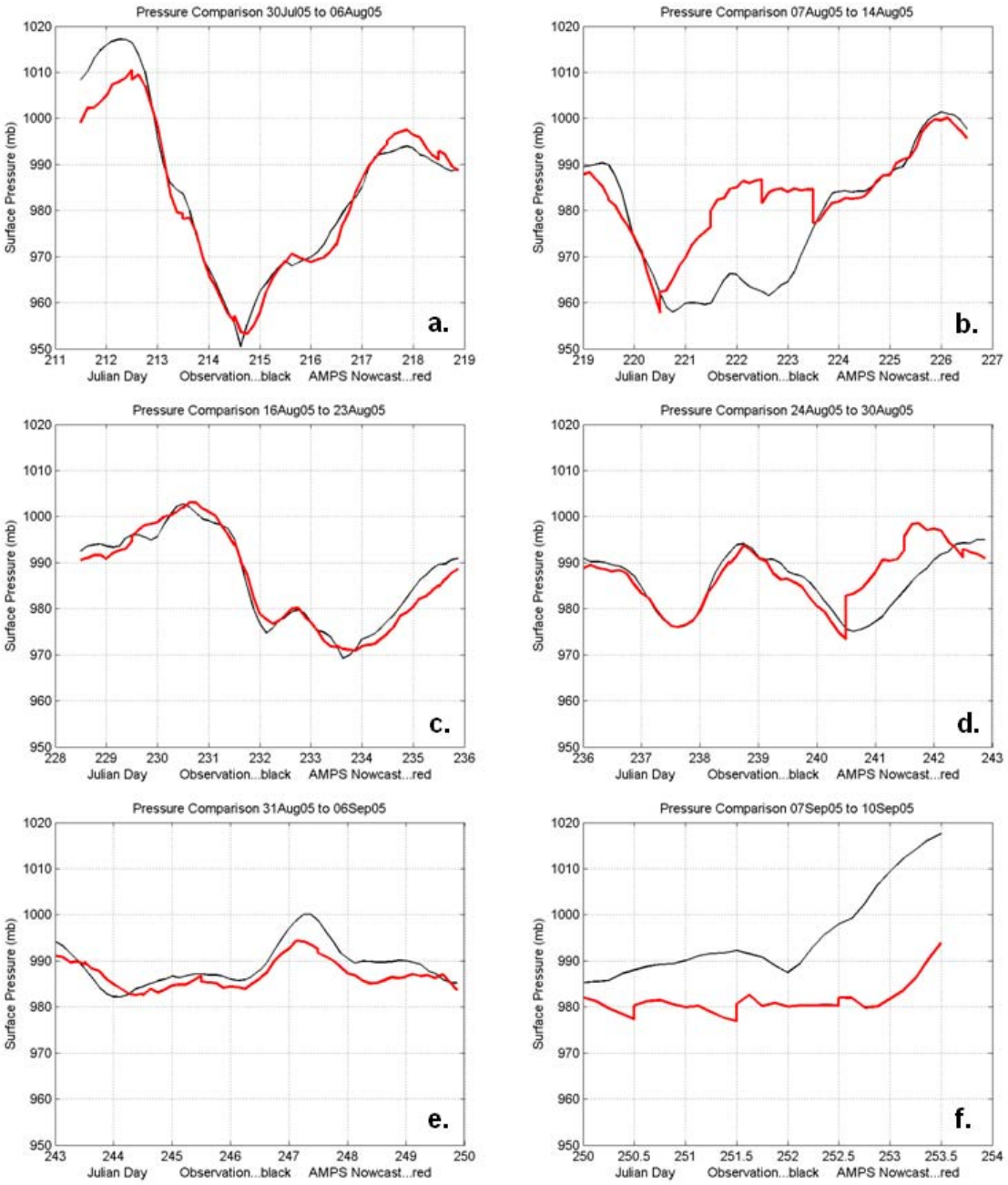

Figure 4. Surface pressure weekly time series. Black line is observational data and red line is AMPS data. a.) 30Jul05 to 06Aug05, b.) 07Aug05 to 14Aug05, c.) 16Aug05 to 23Aug05, d.) 24Aug05 to 30Aug05, e.) 31Aug05 to 06Sep05, and f.) 07Sep05 to 10Sep05.

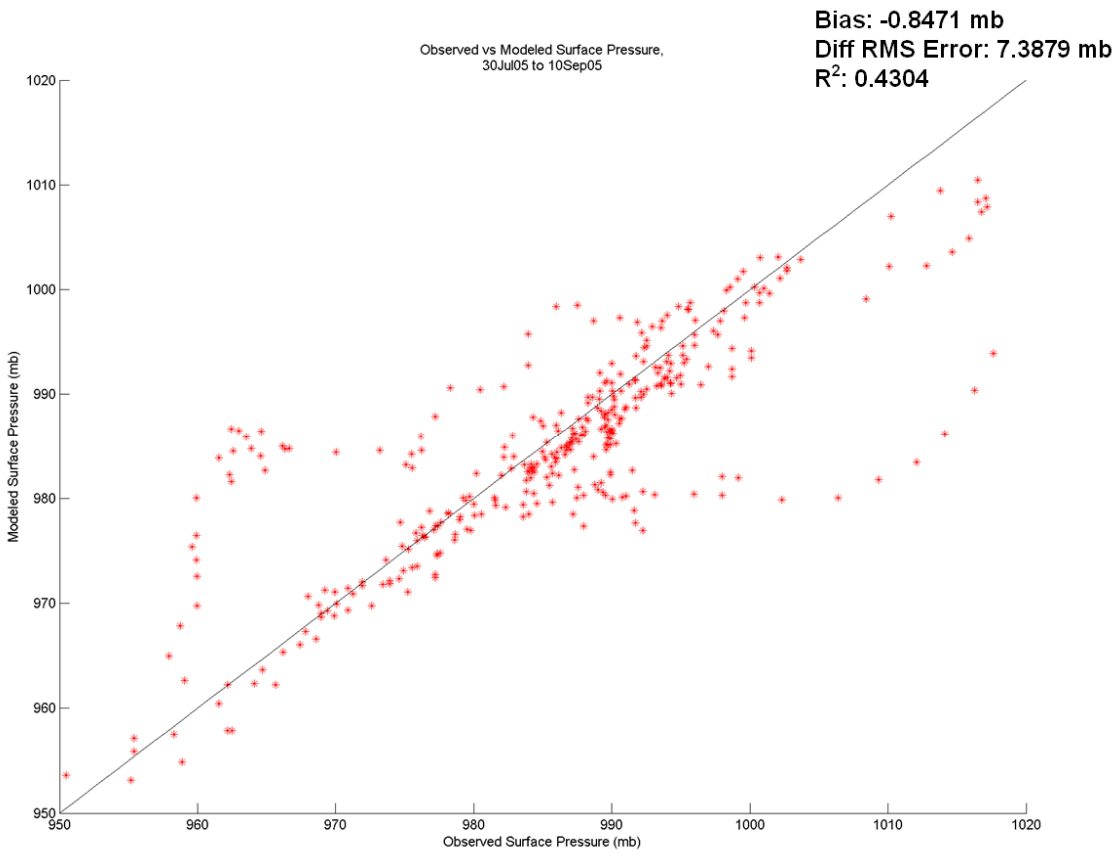

Figure 5. Scatter plot of observed versus modeled surface pressure with correlation line equal to one drawn. Values for bias, differential root mean squared error, and correlation coefficient squared (R^2) are shown in the upper right hand corner.

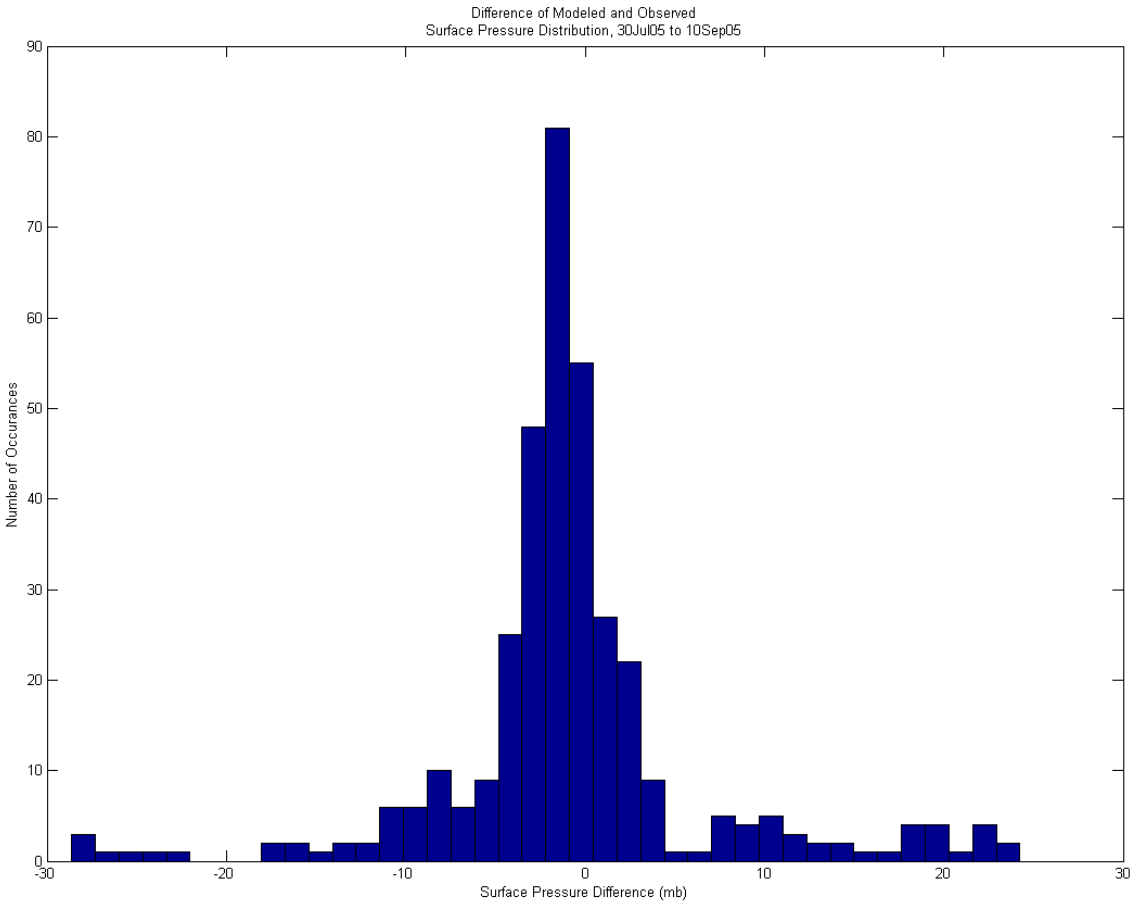

Figure 6. Distribution plot of AMPS surface pressure minus observation surface pressure.

	Number of data points	Min	Max	Mean	Median	RMS Error
AMPS Surface Pressure (mb)	360	953.2	1010.5	984.8	985.1	10.1
Observation Surface Pressure (mb)	360	950.5	1017.6	985.6	987.5	12.6

Table 1. Minimum, maximum, mean, median, and root mean squared values for AMPS derived surface pressure (row one) and observation surface pressure (row two).

	Number of data points	Min	Max	Bias	MS Diff Error	R	R^2
AMPS Surf Press minus Observation Surf Press (mb)	360	-28.6339	24.2523	-0.8471	7.3879	0.656	0.4304

Table 2. Minimum, maximum, bias, differential mean squared error, correlation coefficient (R), and correlation coefficient squared (R^2) for AMPS minus observation surface pressure.

2. Near Surface Air Temperature

As can be seen in Figures 7 and 8, near surface air temperature was quite often over forecast by AMPS. This can also be visualized in Figure 9 where a majority of the points fall above the correlation line, and in Figure 10 where the distribution density is skewed to the positive differential side.

Basic statistics for AMPS and observation near surface air temperature are given in Table 3 and for differential data in Table 4.

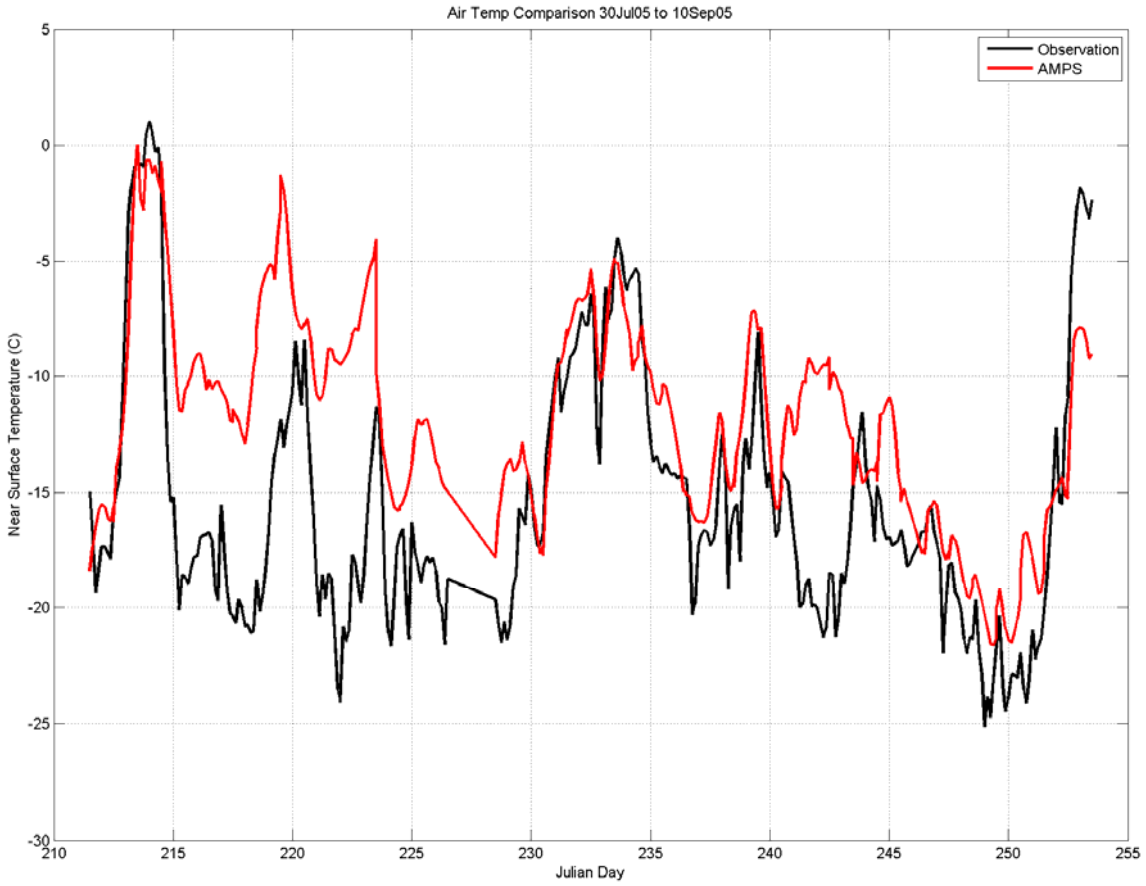

Figure 7. Near surface air temperature time series 30 July 2005 to 10 September 2005. Black line is observational data and red line is AMPS data.

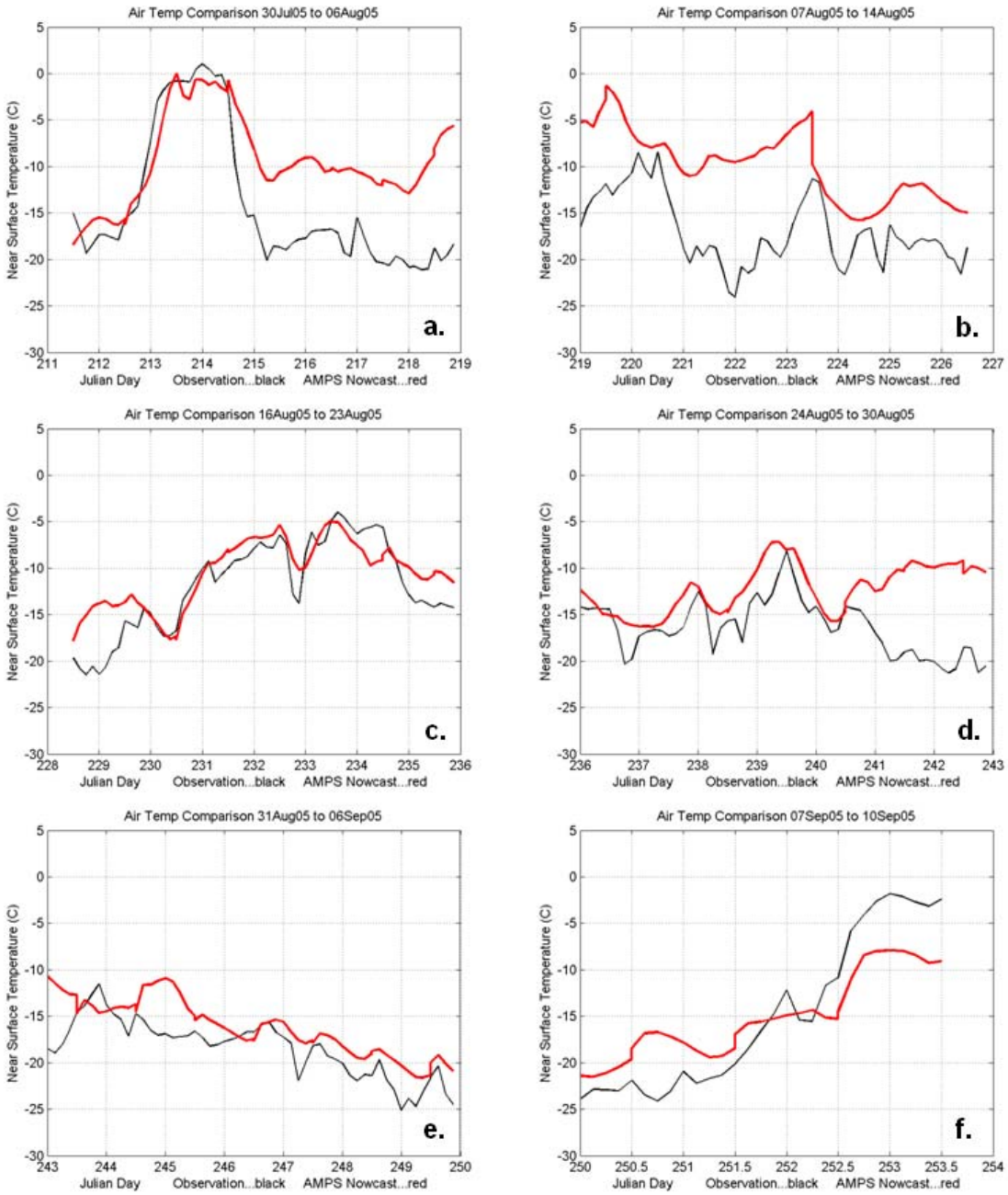

Figure 8. Near surface air temperature weekly time series. Black line is observational data and red line is AMPS data. a.) 30Jul05 to 06Aug05, b.) 07Aug05 to 14Aug05, c.) 16Aug05 to 23Aug05, d.) 24Aug05 to 30Aug05, e.) 31Aug05 to 06Sep05, and f.) 07Sep05 to 10Sep05.

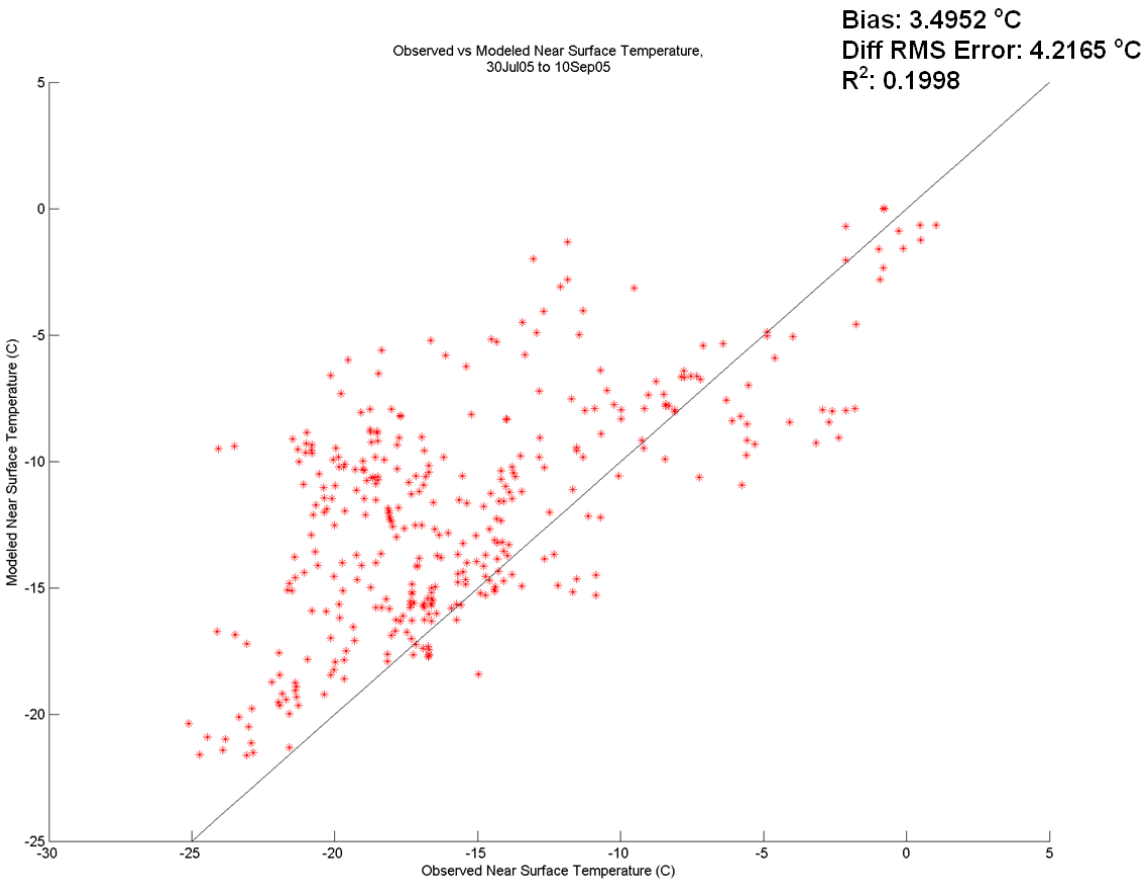

Figure 9. Scatter plot of observed versus modeled near surface air temperature with correlation line equal to one drawn. Values for bias, differential root mean squared error, and correlation coefficient squared (R^2) are shown in the upper right hand corner.

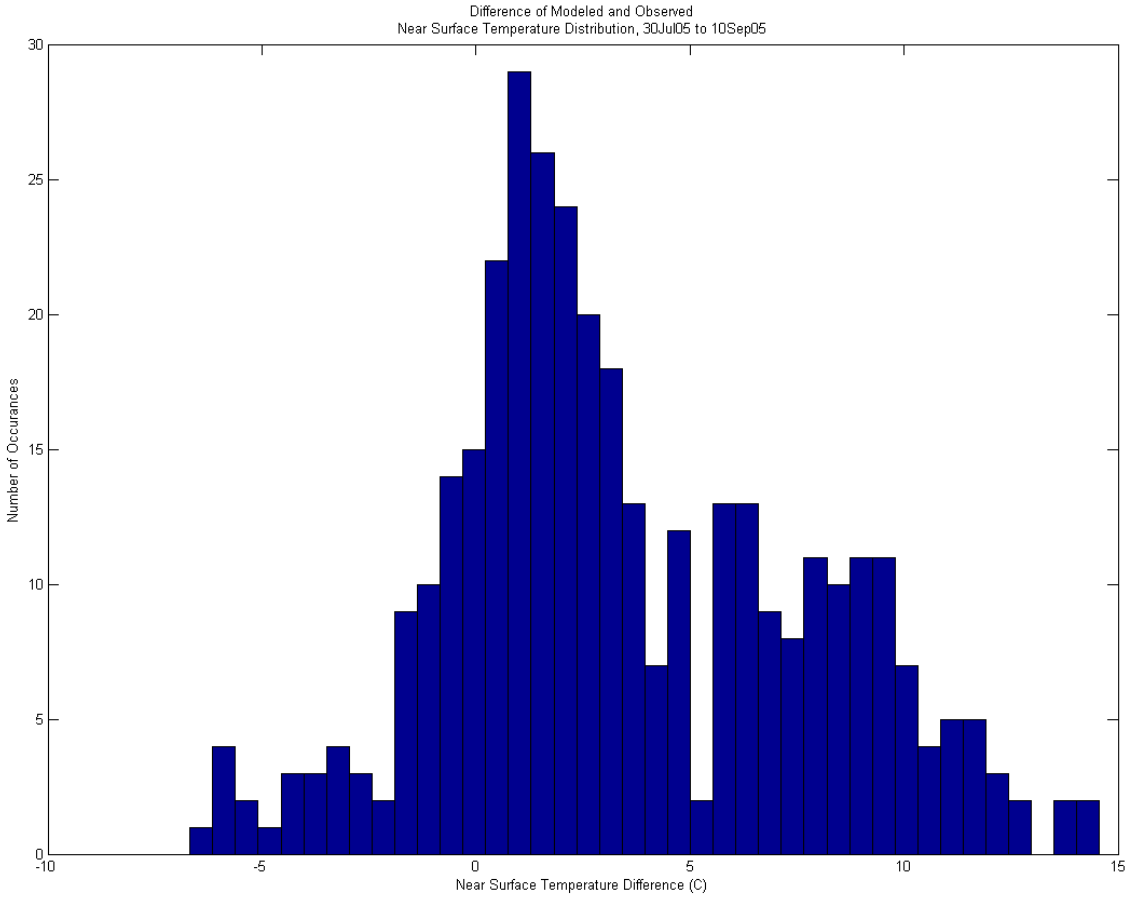

Figure 10. Distribution plot of AMPS near surface air temperature minus observation near surface air temperature.

	Number of data points	Min	Max	Mean	Median	RMS Error
AMPS Air Temperature (^{o}C)	360	-21.5971	0.0274	-11.862	-11.8007	4.5652
Observation Air Temperature (^{o}C)	360	-25.1	1.03	-15.3572	-16.72	5.5524

Table 3. Minimum, maximum, mean, median, and root mean squared values for AMPS derived near surface air temperature (row one) and observation near surface air temperature (row two).

	Number of data points	Min	Max	Bias	MS Diff Error	R	R^2
AMPS Air Temp minus Observation Air Temp (^oC)	360	-6.6809	14.5713	3.4952	4.2165	0.4469	0.1998

Table 4. Minimum, maximum, bias, differential mean squared error, correlation coefficient (R), and correlation coefficient squared (R^2) for AMPS minus observation near surface air temperature.

3. Relative Humidity

AMPS relative humidity was found to have no correlation to observed relative humidity, as can be seen in time series (Figures 11 and 12) and scatter plots (Figure 13). Based on this, differential distribution density (Figure 14) and basic statistical analysis (Tables 5 and 6), it was determined that AMPS had no skill in forecasting relative humidity.

A comparison of relative humidity with respect to ice was also performed with similar results. Relative humidity with respect to ice was calculated as follows:

$$RH_{ice} = RH\left(\frac{e_s}{e_{s_{ice}}}\right) \quad (1)$$

where RH_{ice} is relative humidity with respect to ice, RH is relative humidity, e_s is saturation vapor pressure (both AMPS values and observed), and e_{sice} is saturation vapor pressure with regards to ice (Both AMPS values and observed).

Time series (Figure 15) showed that overall, observed values of relative humidity with respect to ice were at saturation up to Julian day 250. AMPS relative humidity with respect to ice did not follow this trend, with values as low as 65 % to values as high as 125%. A scatter plot (Figure 16) of observed versus AMPS relative humidity with respect to ice showed no clear trends along a one-to-one correlation line. A differential distribution density plot (Figure 17) also showed wide variability between modeled and observed values, and a slight trend towards negative differences. Basic statistics and correlation are shown in Tables 7 and 8. Note that the correlation coefficient shown in

Table 8 is much less than 1 (0.0041) indicating no correlation between modeled and observed relative humidity with respect to ice.

The final comparison was based on Andreas et al. (2002) which found that in a polar environment relative humidity with respect to ice was almost always near one hundred percent. With this in mind, equation (1) was rearranged to solve for RH with RH_{ice} set at one hundred percent (using AMPS derived saturation vapor pressure values). Time series comparisons of observed relative humidity and relative humidity calculated from relative humidity with respect to ice at saturation are shown in Figure 18. Relative humidity calculated from relative humidity with respect to ice followed observed relative humidity close than AMPS forecast relative humidity, but missed all of the drying trends seen in the observed values. The scatter plot shown in Figure 19 shows a slight increase in grouping around a one-to-one correlation line, and differential distribution density (Figure 20) shifted slightly away from negative differences. Basic statistics and correlation are shown in Tables 9 and 10. Correlation coefficient and correlation coefficient squared (0.2842 and 0.0808 respectively) indicate slightly better correlation when relative humidity with respect to ice is set to saturation than straight AMPS output.

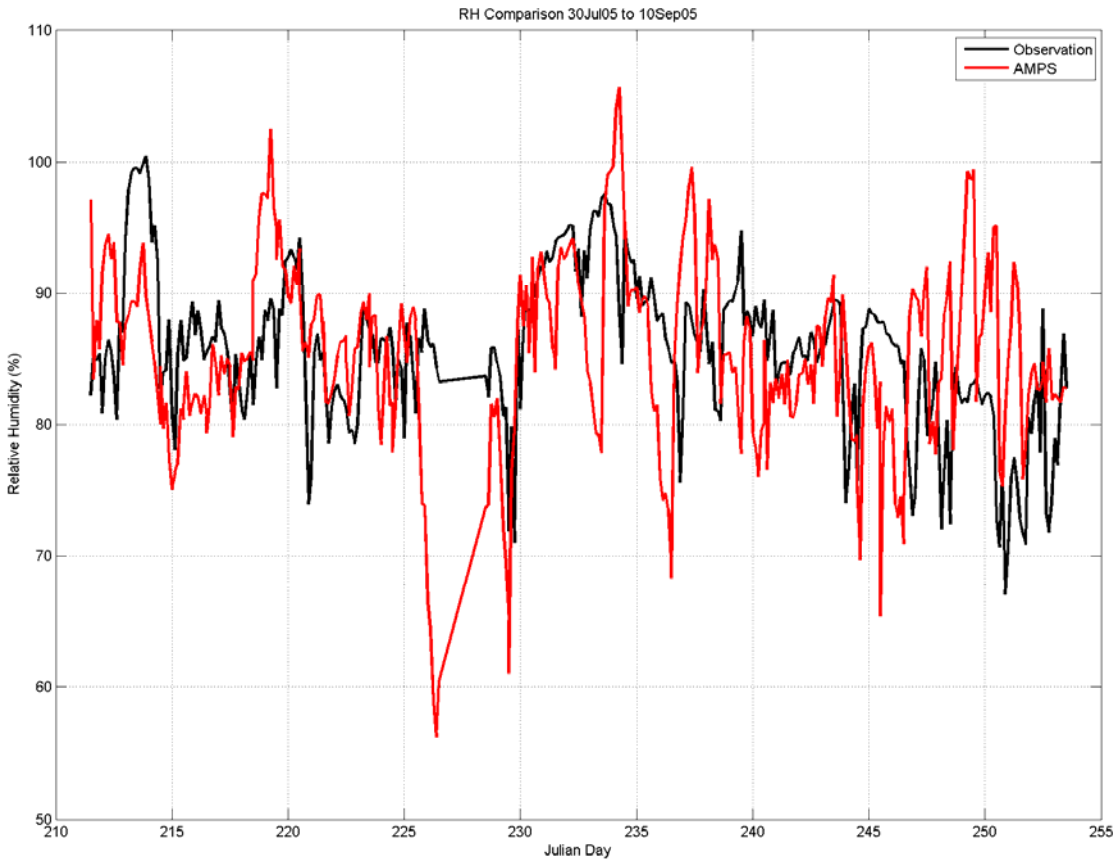

Figure 11. Relative humidity time series 30 July 2005 to 10 September 2005. Black line is observational data and red line is AMPS data.

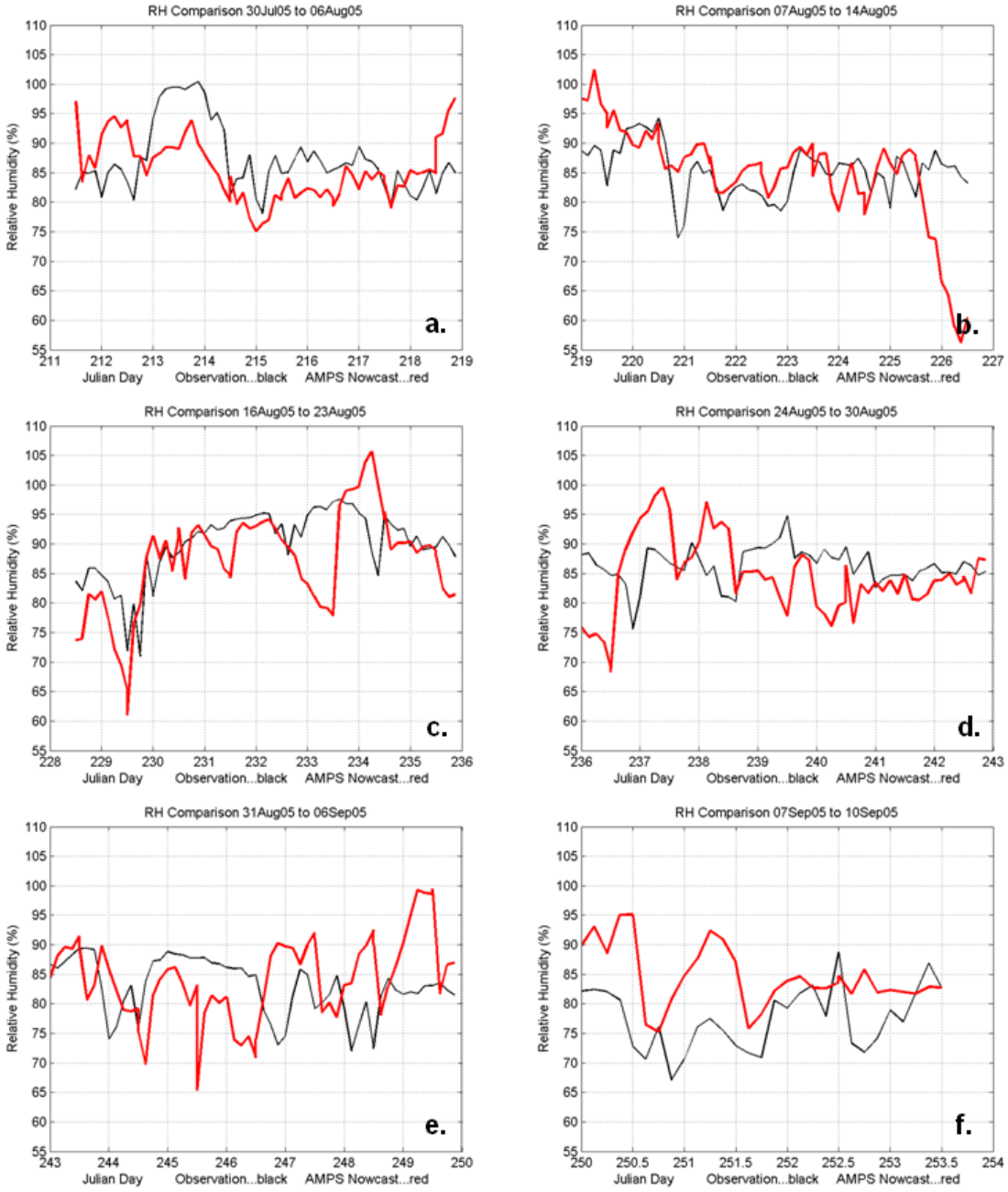

Figure 12. Relative humidity weekly time series. Black line is observational data and red line is AMPS data. a.) 30Jul05 to 06Aug05, b.) 07Aug05 to 14Aug05, c.) 16Aug05 to 23Aug05, d.) 24Aug05 to 30Aug05, e.) 31Aug05 to 06Sep05, and f.) 07Sep05 to 10Sep05.

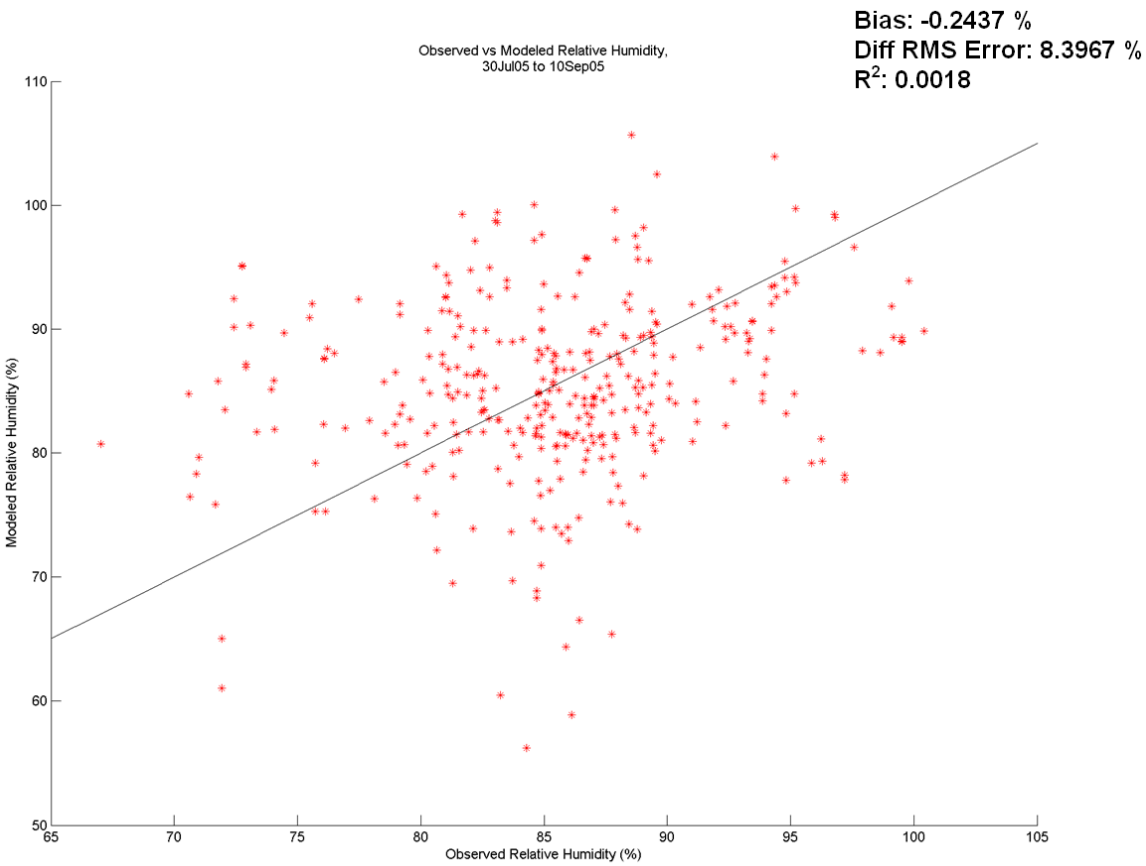

Figure 13. Scatter plot of observed versus modeled relative humidity with correlation line equal to one drawn. Values for bias, differential root mean squared error, and correlation coefficient squared (R^2) are shown in the upper right hand corner.

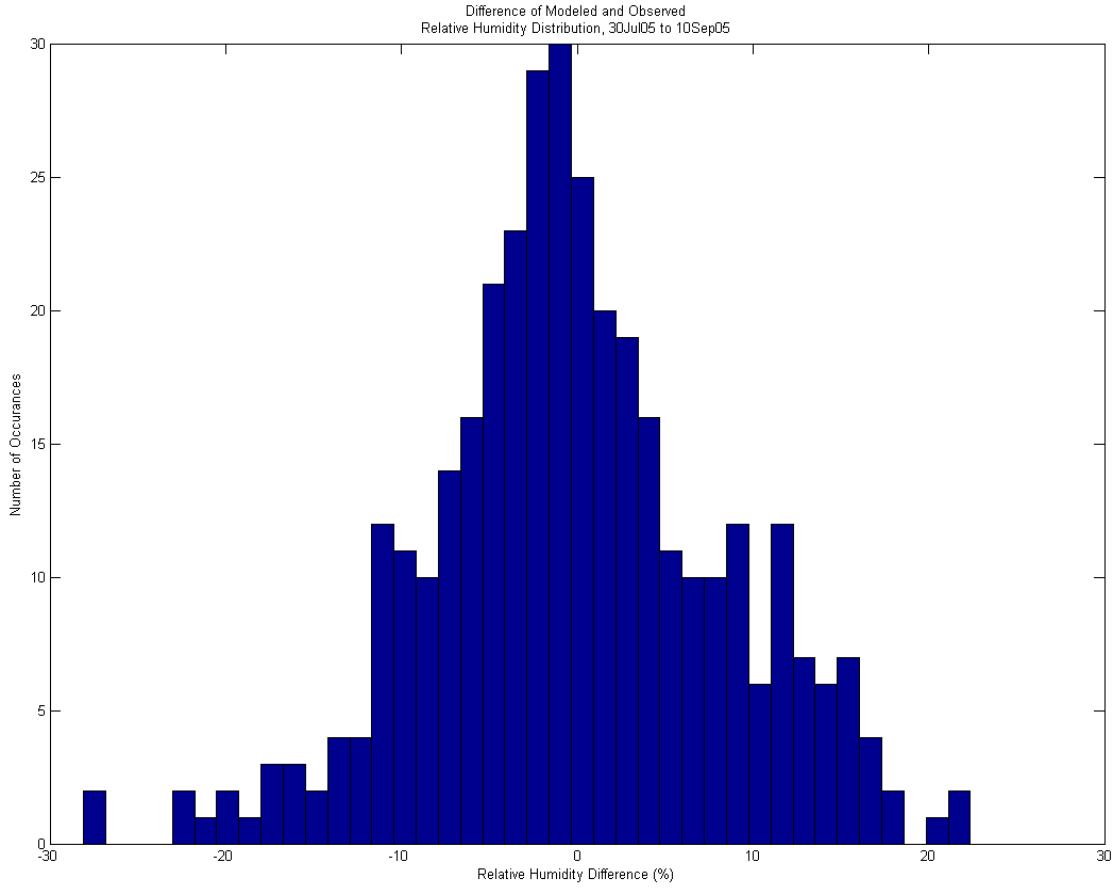

Figure 14. Distribution plot of AMPS relative humidity minus observation relative humidity.

	Number of data points	Min	Max	Mean	Median	RMS Error
AMPS Relative Humidity (%)	360	-21.5971	0.0274	85.3236	85.2671	7.2404
Observation Relative Humidity (%)	360	-25.1	1.03	85.5672	85.67	6.003

Table 5. Minimum, maximum, mean, median, and root mean squared values for AMPS derived relative humidity (row one) and observation relative humidity (row two).

	Number of data points	Min	Max	Bias	MS Diff Error	R	R^2
AMPS Air Temp minus Observation Air Temp (°C)	360	-28.0775	22.371	-0.2437	8.3967	0.0427	0.0018

Table 6. Minimum, maximum, bias, differential mean squared error, correlation coefficient (R), and correlation coefficient squared (R^2) for AMPS minus observation relative humidity.

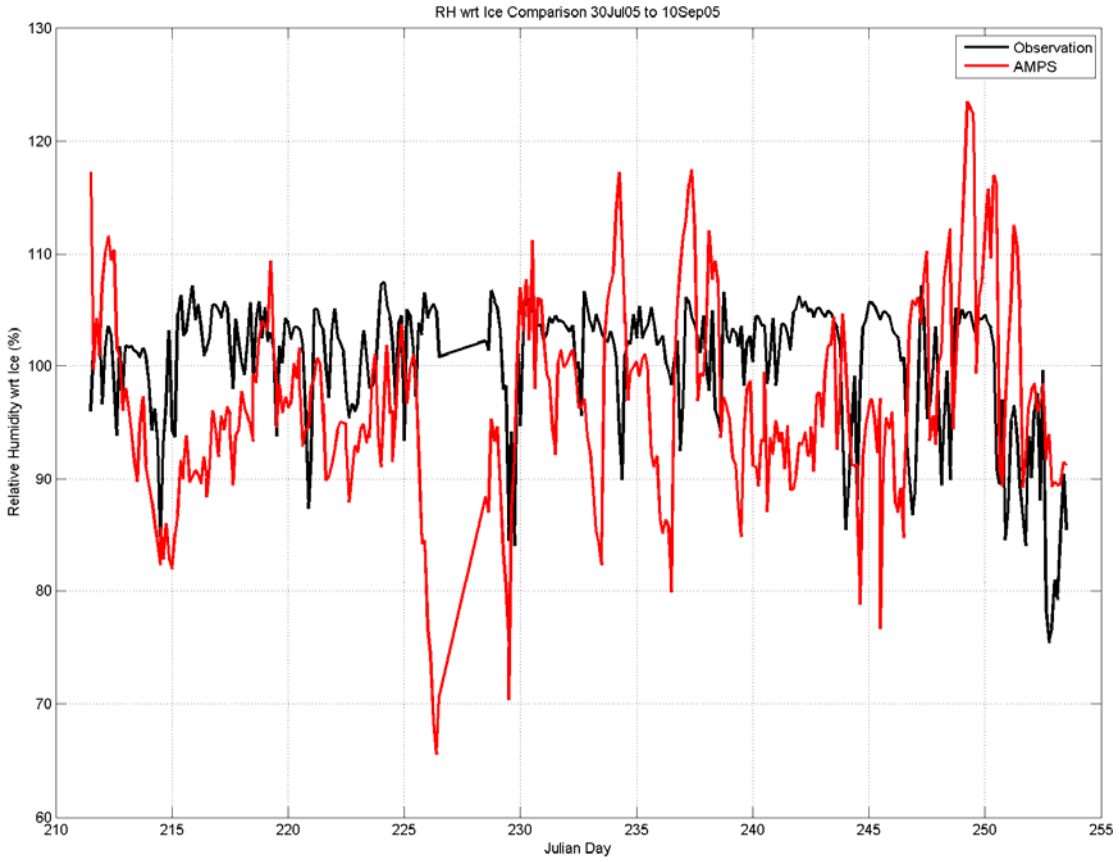

Figure 15. Relative humidity with respect to ice time series 30 July 2005 to 10 September 2005. Black line is observational data and red line is AMPS data.

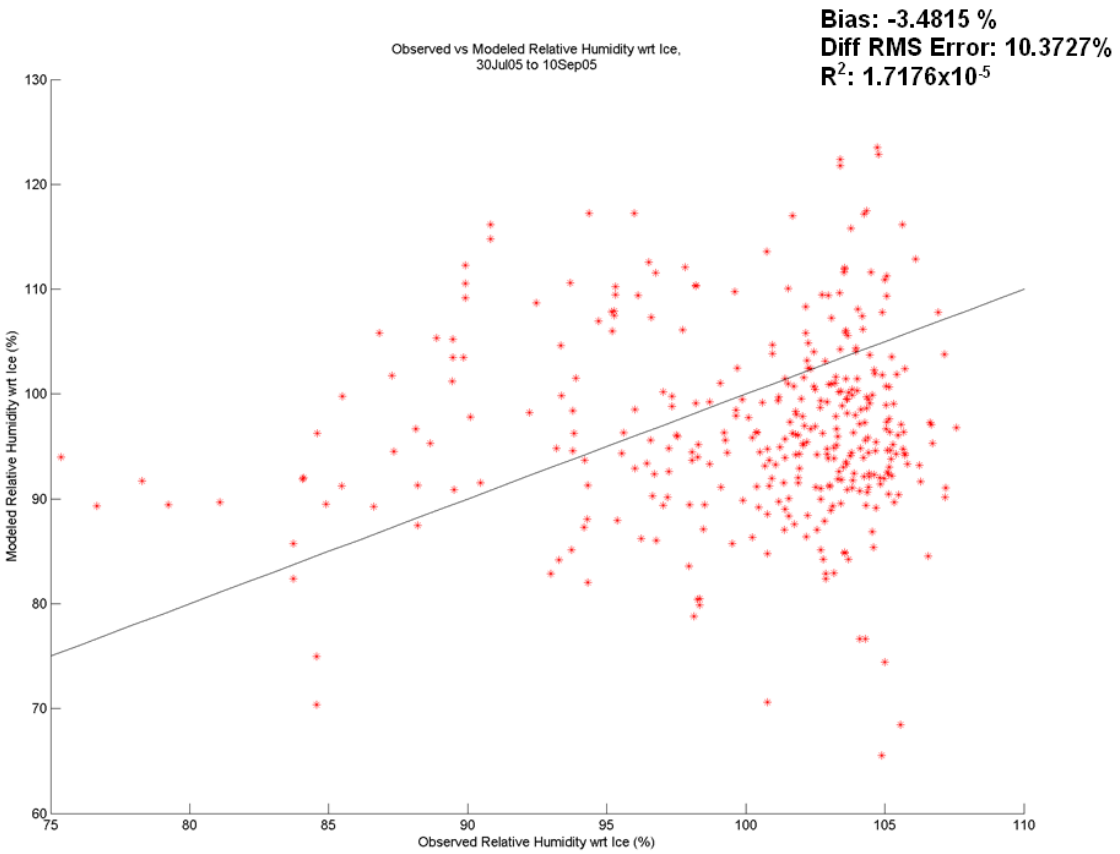

Figure 16. Scatter plot of observed versus modeled relative humidity with respect to ice with correlation line equal to one drawn. Values for bias, differential root mean squared error, and correlation coefficient squared (R^2) are shown in the upper right hand corner.

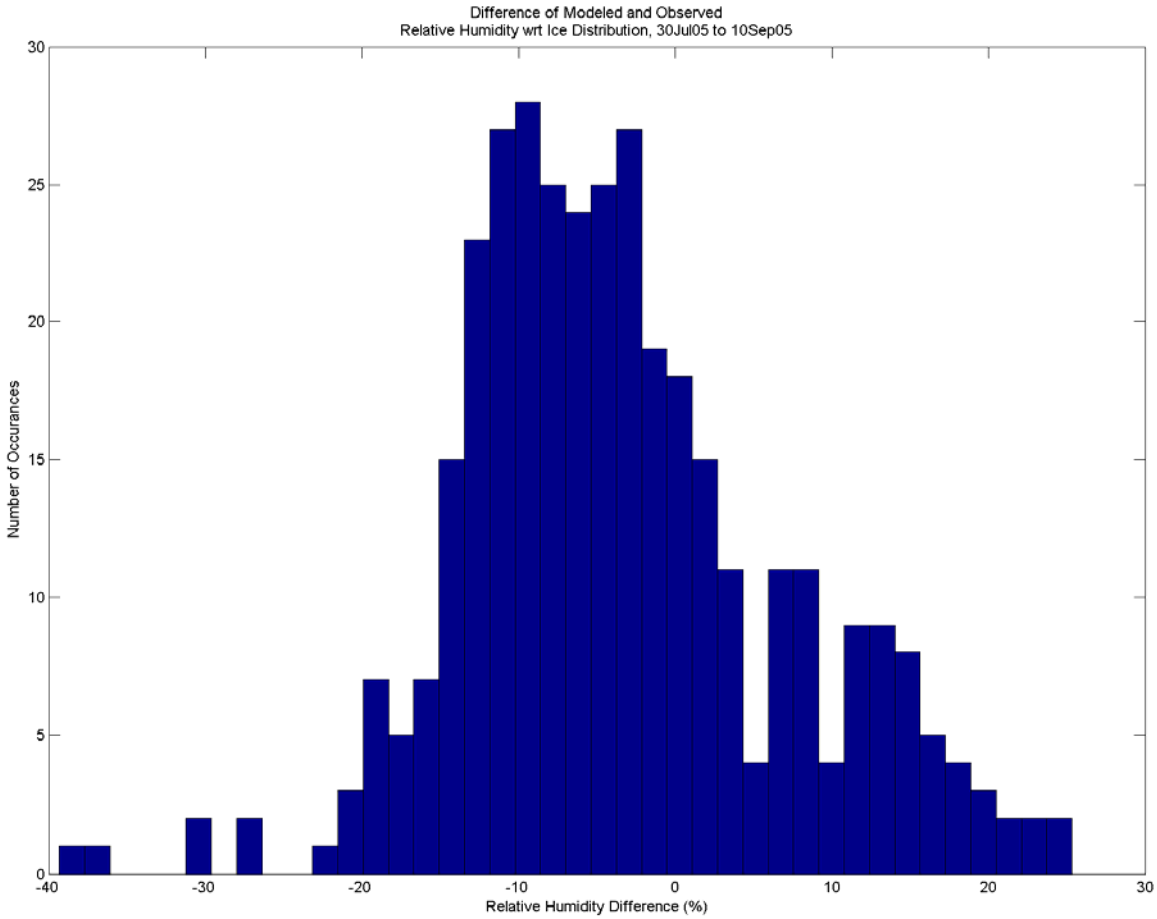

Figure 17. Distribution plot of AMPS relative humidity with respect to ice minus observation relative humidity with respect to ice.

	Number of data points	Min	Max	Mean	Median	RMS Error
AMPS Relative Humidity of Ice(%)	360	65.5469	123.5048	96.6991	95.8189	8.9648
Observation Relative Humidity of Ice(%)	360	75.378	107.5769	100.1805	102.2276	5.8268

Table 7. Minimum, maximum, mean, median, and root mean squared values for AMPS derived relative humidity with respect to ice (row one) and observation relative humidity with respect to ice (row two).

	Number of data points	Min	Max	Bias	MS Diff Error	R	R^2
AMPS RH of Ice minus Ob RH of Ice (%)	360	-39.3284	25.3316	-3.4815	10.3727	0.0041	1.72E-05

Table 8. Minimum, maximum, bias, differential mean squared error, correlation coefficient (R), and correlation coefficient squared (R^2) for AMPS minus observation relative humidity with respect to ice.

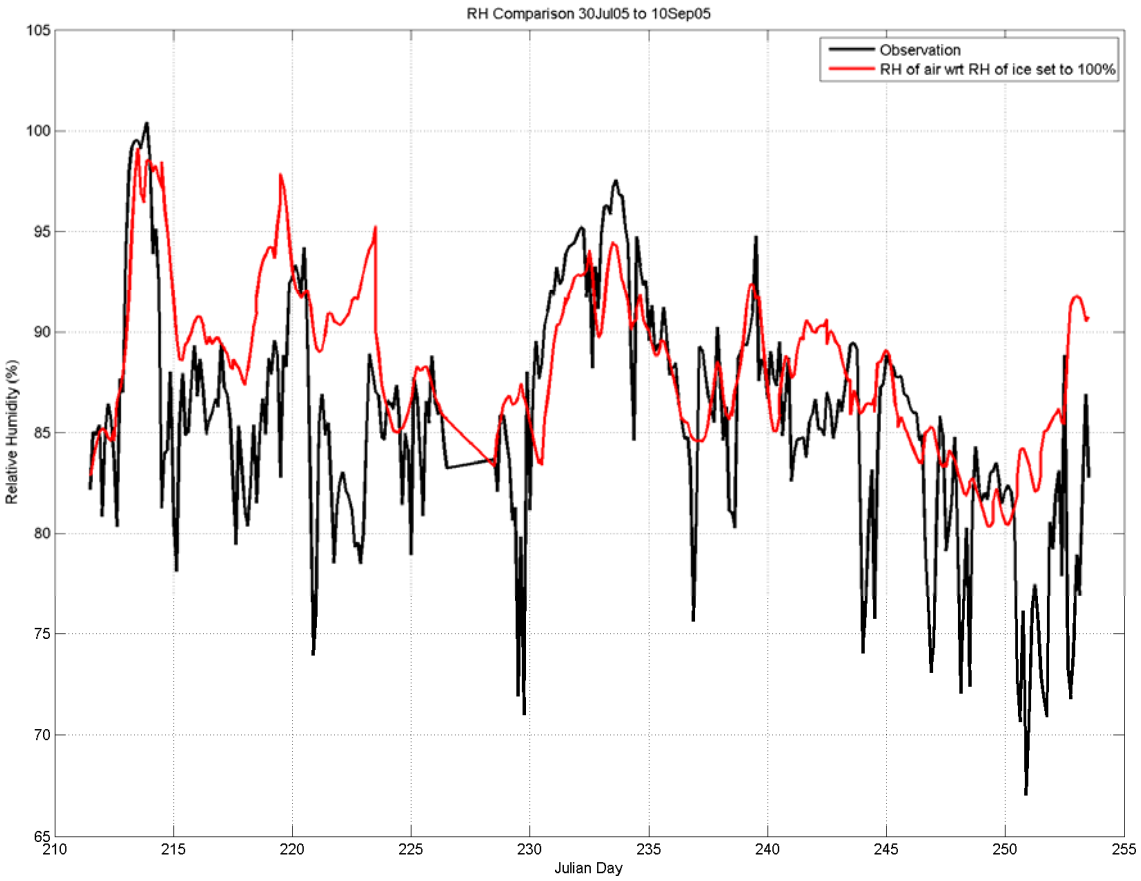

Figure 18. Relative humidity time series 30 July 2005 to 10 September 2005. Black line is observation, red line is relative humidity calculated from relative humidity of ice at saturation.

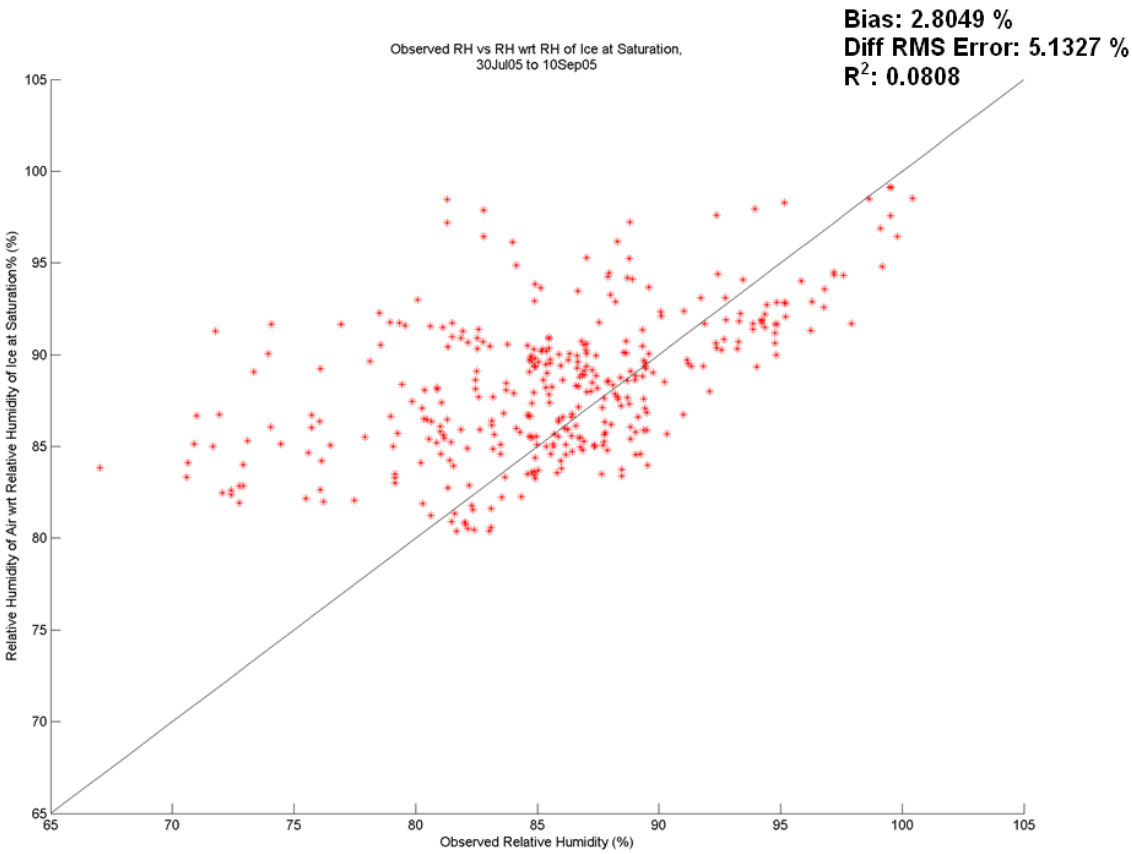

Figure 19. Scatter plot of observed relative humidity versus relative humidity calculated from relative humidity of ice at saturation, with correlation line equal to one drawn. Values for bias, differential root mean squared error, and correlation coefficient squared (R^2) are shown in the upper right hand corner.

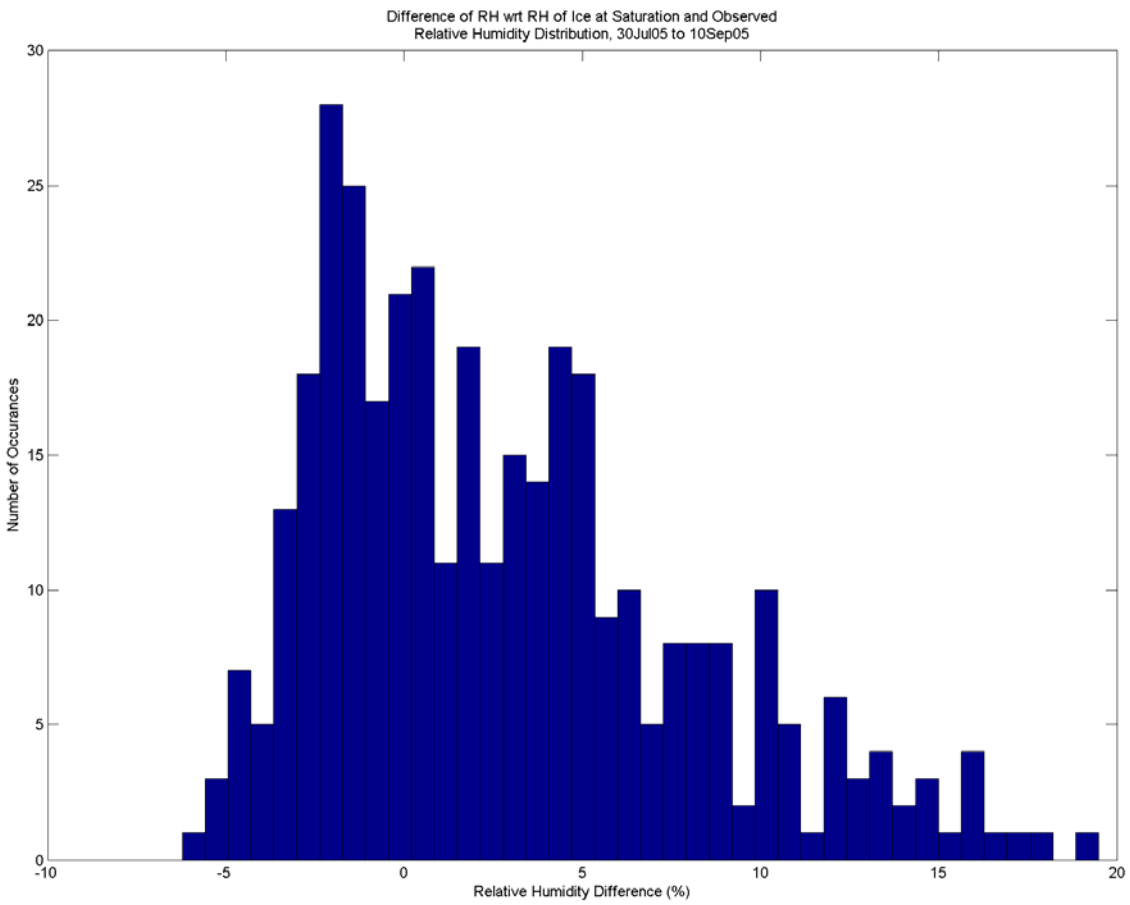

Figure 20. Distribution plot of relative humidity calculated from relative humidity of ice at saturation minus observation relative humidity.

	Number of data points	Min	Max	Mean	Median	RMS Error
Relative Humidity wrt Relative Humidity of Ice at Saturation (%)	360	80.3716	99.1549	88.3721	88.3215	3.9406
Observation Relative Humidity (%)	360	67.03	100.43	85.5672	85.67	6.003

Table 9. Minimum, maximum, mean, median, and root mean squared values for relative humidity calculated from relative humidity of ice at saturation (row one) and observation relative humidity (row two).

	Number of data points	Min	Max	Bias	MS Diff Error	R	R^2
RH wrt RH of Ice at Saturation minus Observation RH (%)	360	-6.2233	19.4923	2.8049	5.1327	0.2842	0.0808

Table 10. Minimum, maximum, bias, differential mean squared error, correlation coefficient (R), and correlation coefficient squared (R^2) for relative humidity calculated from relative humidity of ice at saturation minus observation relative humidity.

4. Specific Humidity

Specific humidity, with a dependence on air temperature, followed a similar trend of being over forecast by AMPS. This can be visualized in time series (Figures 21 and 22), scatter (Figure 23) differential distribution density (Figure 24) plots, and basic statistics (Tables 11 and 12).

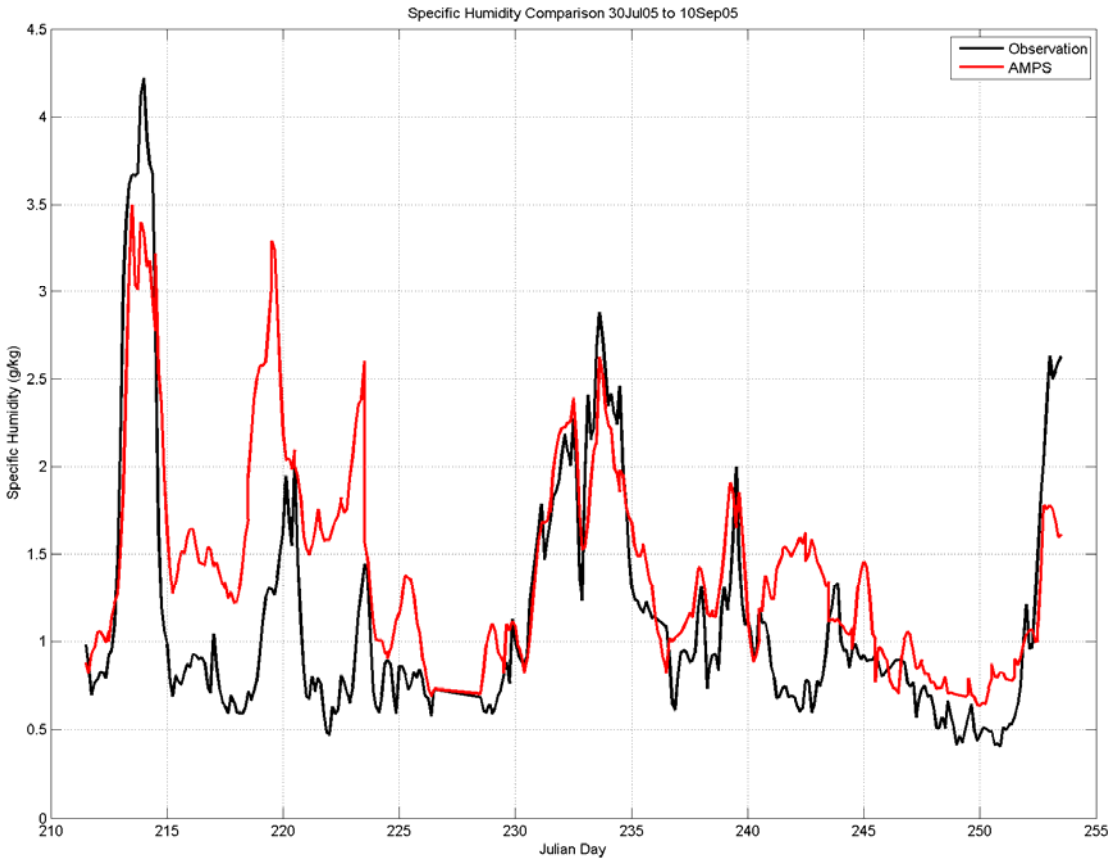

Figure 21. Specific humidity time series 30 July 2005 to 10 September 2005. Black line is observational data and red line is AMPS data.

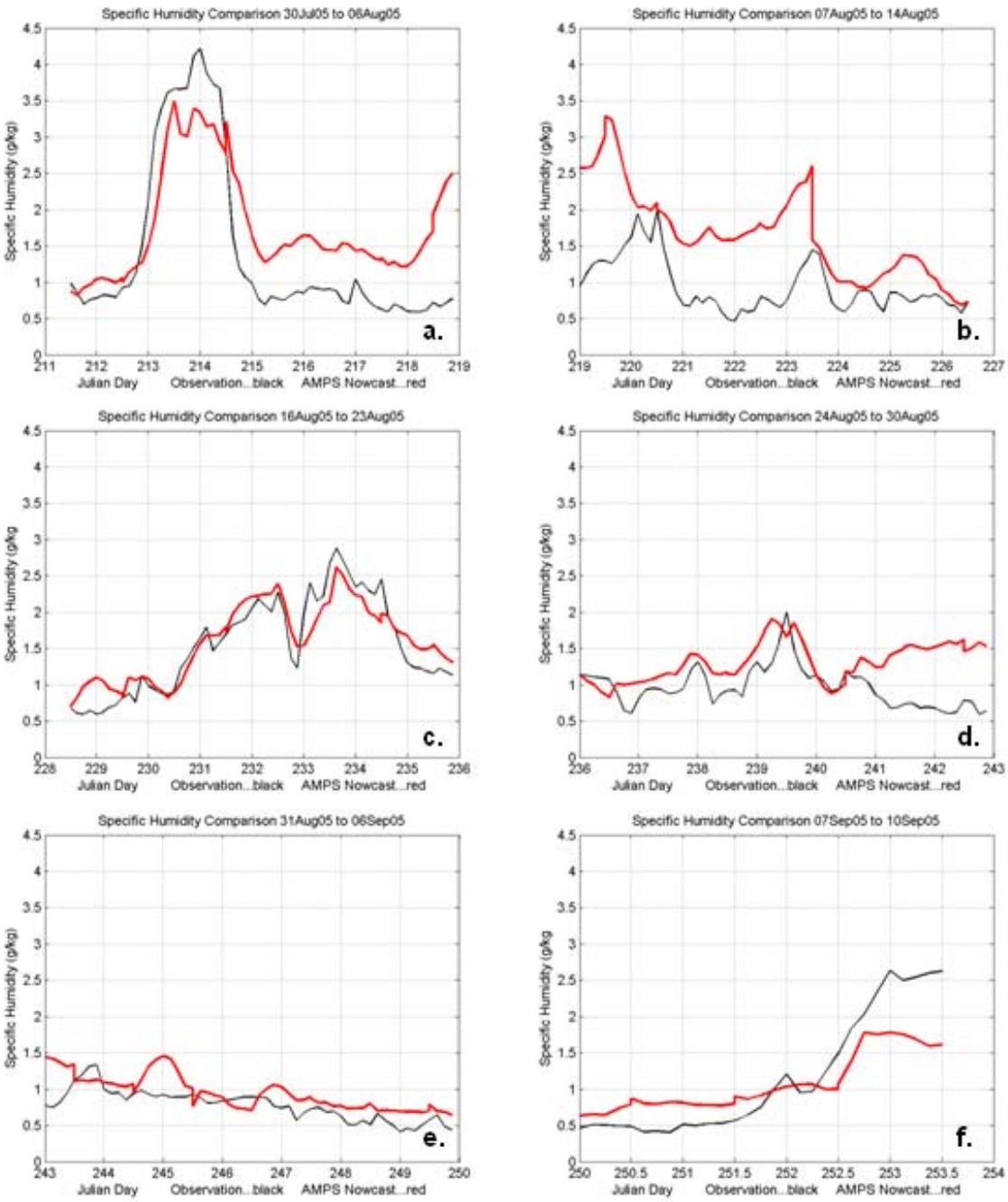

Figure 22. Specific humidity weekly time series. Black line is observational data and red line is AMPS data. a.) 30Jul05 to 06Aug05, b.) 07Aug05 to 14Aug05, c.) 16Aug05 to 23Aug05, d.) 24Aug05 to 30Aug05, e.) 31Aug05 to 06Sep05, and f.) 07Sep05 to 10Sep05.

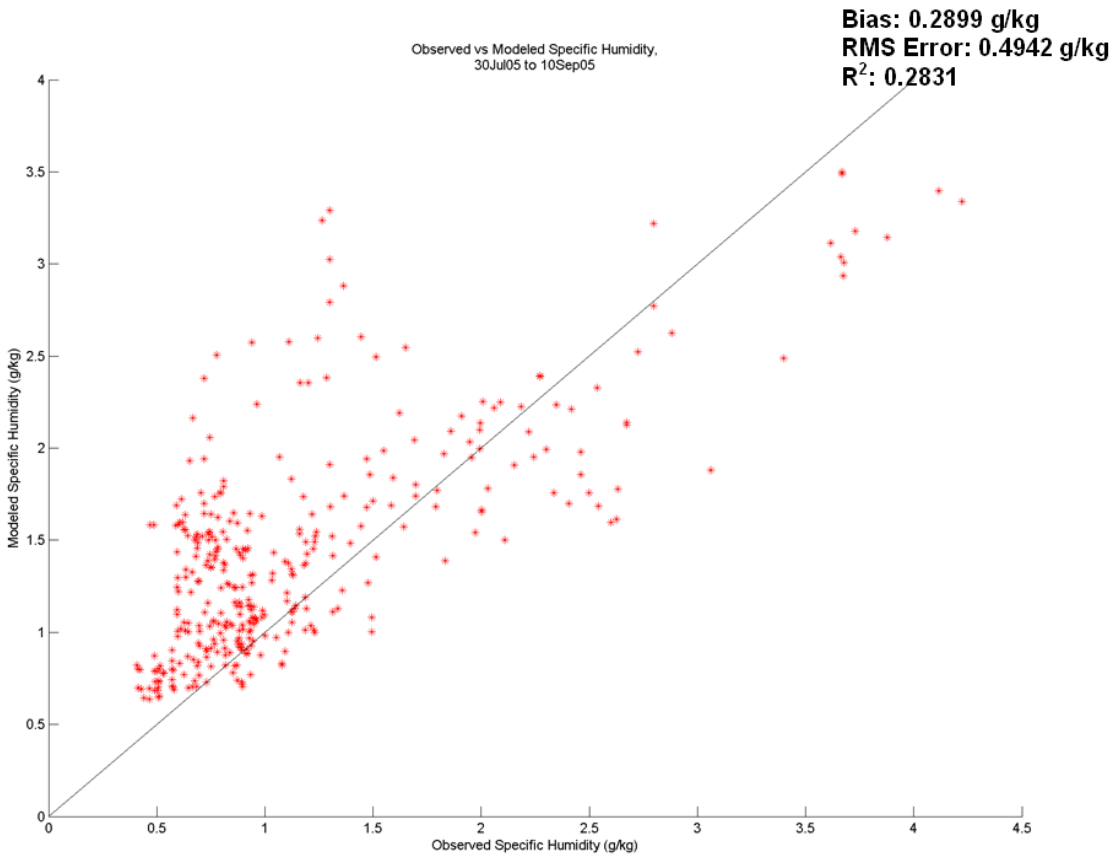

Figure 23. Scatter plot of observed versus modeled specific humidity with correlation line equal to one drawn. Values for bias, differential root mean squared error, and correlation coefficient squared (R^2) are shown in the upper right hand corner.

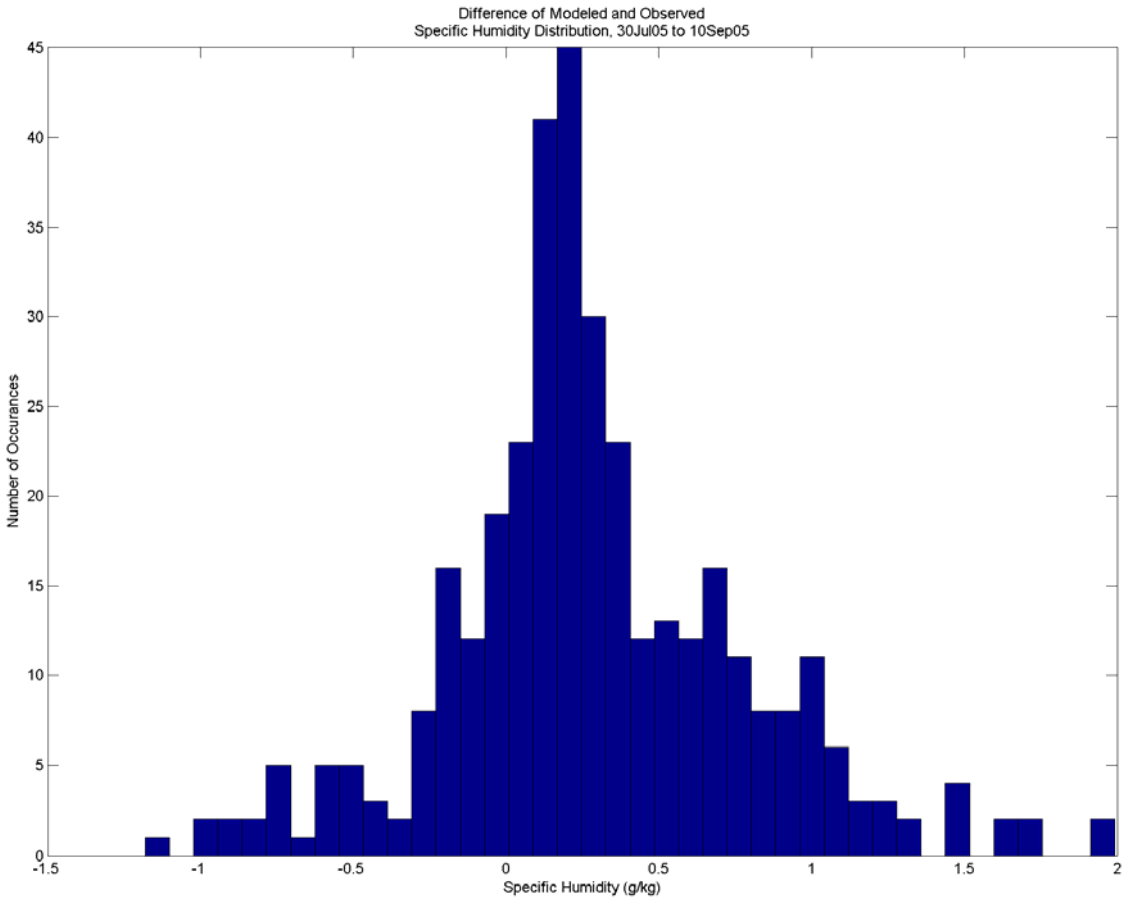

Figure 24. Distribution plot of AMPS specific humidity minus observation specific humidity.

	Number of data points	Min	Max	Mean	Median	RMS Error
AMPS Specific Humidity (g/kg)	360	0.6371	3.4982	1.4369	1.3426	0.6012
Observation Specific Humidity (g/kg)	360	0.4069	4.2216	1.147	0.8938	0.7125

Table 11. Minimum, maximum, mean, median, and root mean squared values for AMPS derived specific humidity (row one) and observation specific humidity (row two).

	Number of data points	Min	Max	Bias	MS Diff Error	R	R^2
AMPS Spec Humidity minus Ob Spec Humidity (g/kg)	360	-1.1812	1.9932	0.2899	0.4942	0.5321	0.2831

Table 12. Minimum, maximum, bias, differential mean squared error, correlation coefficient (R), and correlation coefficient squared (R^2) for AMPS minus observation specific humidity.

5. Near Surface Wind Speed

Near surface wind speed time series (Figures 25 and 26) showed that AMPS forecast values tended to agree well with observed values. The major error was found to be under-forecasting of wind speed (Julian days 215, 222 to 223, and 243 to 245). Wind speed under-forecast periods tend to occur when AMPS over-forecast surface pressure. A scatter plot of observed versus AMPS wind speeds (Figure 27), showed relatively good grouping of data points around the one-to-one correlation line. Differential distribution density is shown in Figure 28. Basic statistics and correlation are presented in Tables 13 and 14.

AMPS forecast wind speed was found to correlate relatively well (correlation coefficient of 0.551 shown in Table 14) with observed wind speed. This reinforced the idea that AMPS was handling the synoptic situation well, but slightly under-forecasting storm intensity.

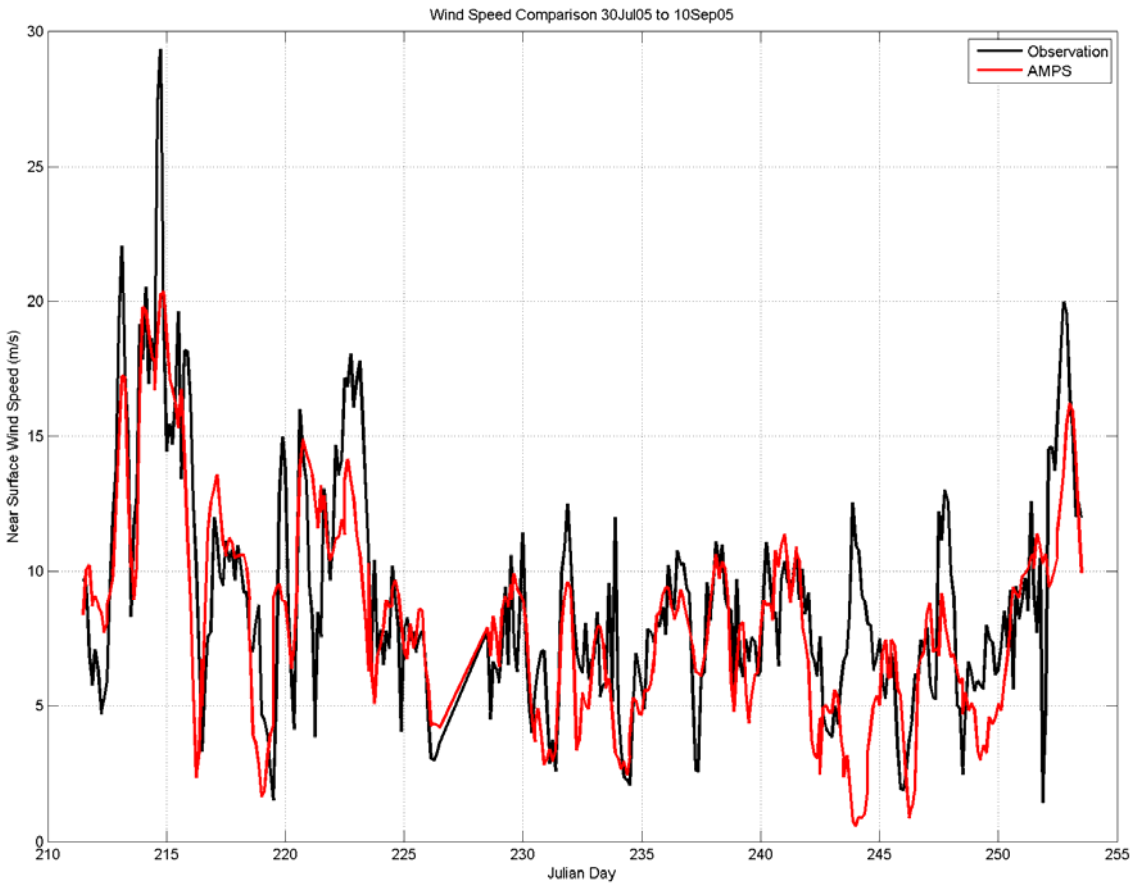

Figure 25. Near surface wind speed time series 30 July 2005 to 10 September 2005. Black line is observational data and red line is AMPS data.

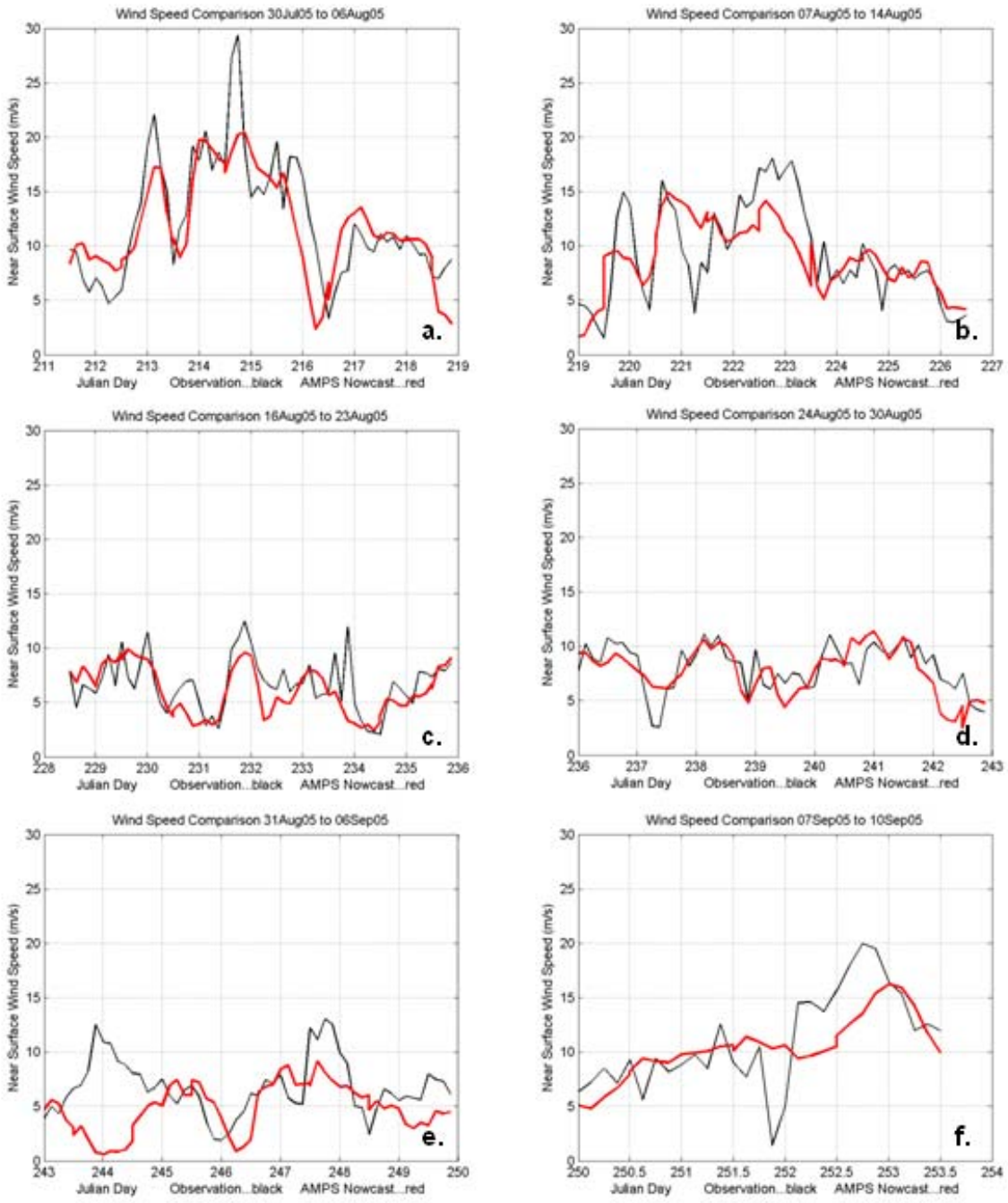

Figure 26. Near surface wind speed weekly time series. Black line is observational data and red line is AMPS data. a.) 30Jul05 to 06Aug05, b.) 07Aug05 to 14Aug05, c.) 16Aug05 to 23Aug05, d.) 24Aug05 to 30Aug05, e.) 31Aug05 to 06Sep05, and f.) 07Sep05 to 10Sep05.

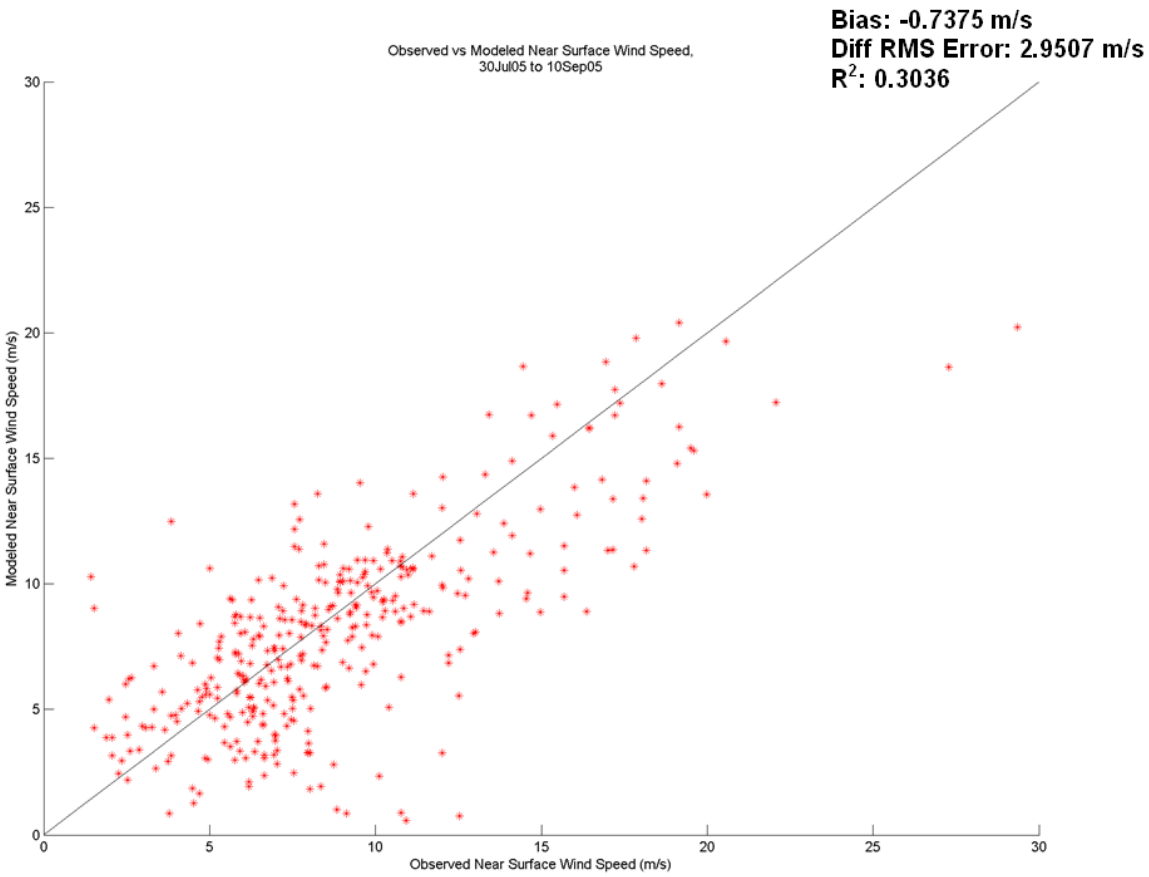

Figure 27. Scatter plot of observed versus modeled near surface wind speed with correlation line equal to one drawn. Values for bias, differential root mean squared error, and correlation coefficient squared (R^2) are shown in the upper right hand corner.

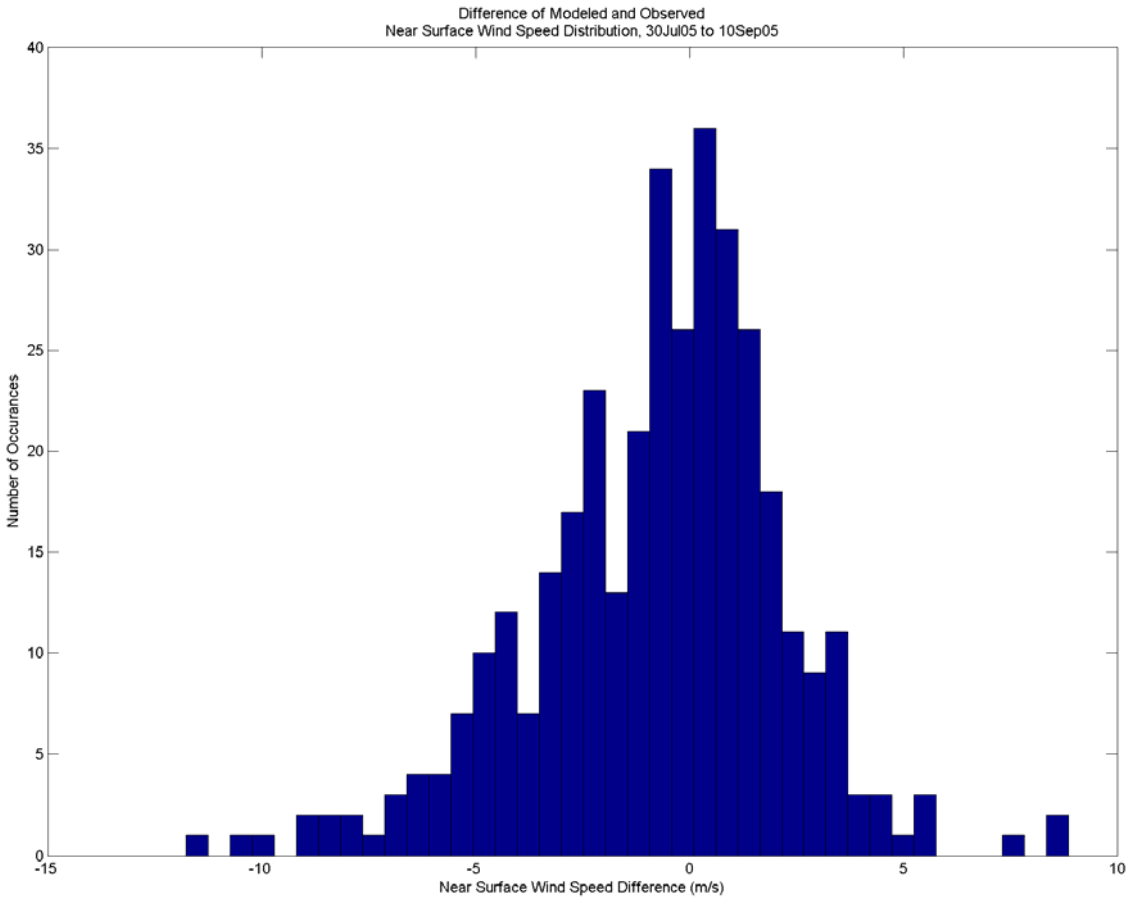

Figure 28. Distribution plot of AMPS near surface wind speed minus observation near surface wind speed.

	Number of data points	Min	Max	Mean	Median	RMS Error
AMPS Wind Speed (m/s)	360	0.5725	20.4145	8.1054	7.9948	3.8589
Observation Wind Speed (m/s)	360	1.42	29.35	8.8429	7.97	4.2857

Table 13. Minimum, maximum, mean, median, and root mean squared values for AMPS derived near surface wind speed (row one) and observation near surface wind speed (row two).

	Number of data points	Min	Max	Bias	MS Diff Error	R	R^2
AMPS Wind Speed minus Ob Wind Speed (m/s)	360	-11.7736	8.8707	-0.7375	2.9507	0.551	0.3036

Table 14. Minimum, maximum, bias, differential mean squared error, correlation coefficient (R), and correlation coefficient squared (R^2) for AMPS minus observation near surface wind speed.

6. Near Surface Wind Direction

Weekly time series plots (Figure 29, presented for better clarity) showed AMPS near surface wind direction compared well with observed wind direction, with notable exceptions on Julian days 216, 219 to 220, 242 to 244, and 252.

Figure 30 presents a scatter plot of observed versus AMPS wind direction, and Figure 31 shows differential distribution density. It should be noted that these plots and basic statistics (Table 15) can be misleading, appearing to have large error when wind directions are northerly. This is due to the wind direction being represented from 0 to 360 degrees clockwise, with north being at the 0 and 360 degree point. With this in mind, and inspection of the time series plots shows that wind direction was indeed forecast well by AMPS.

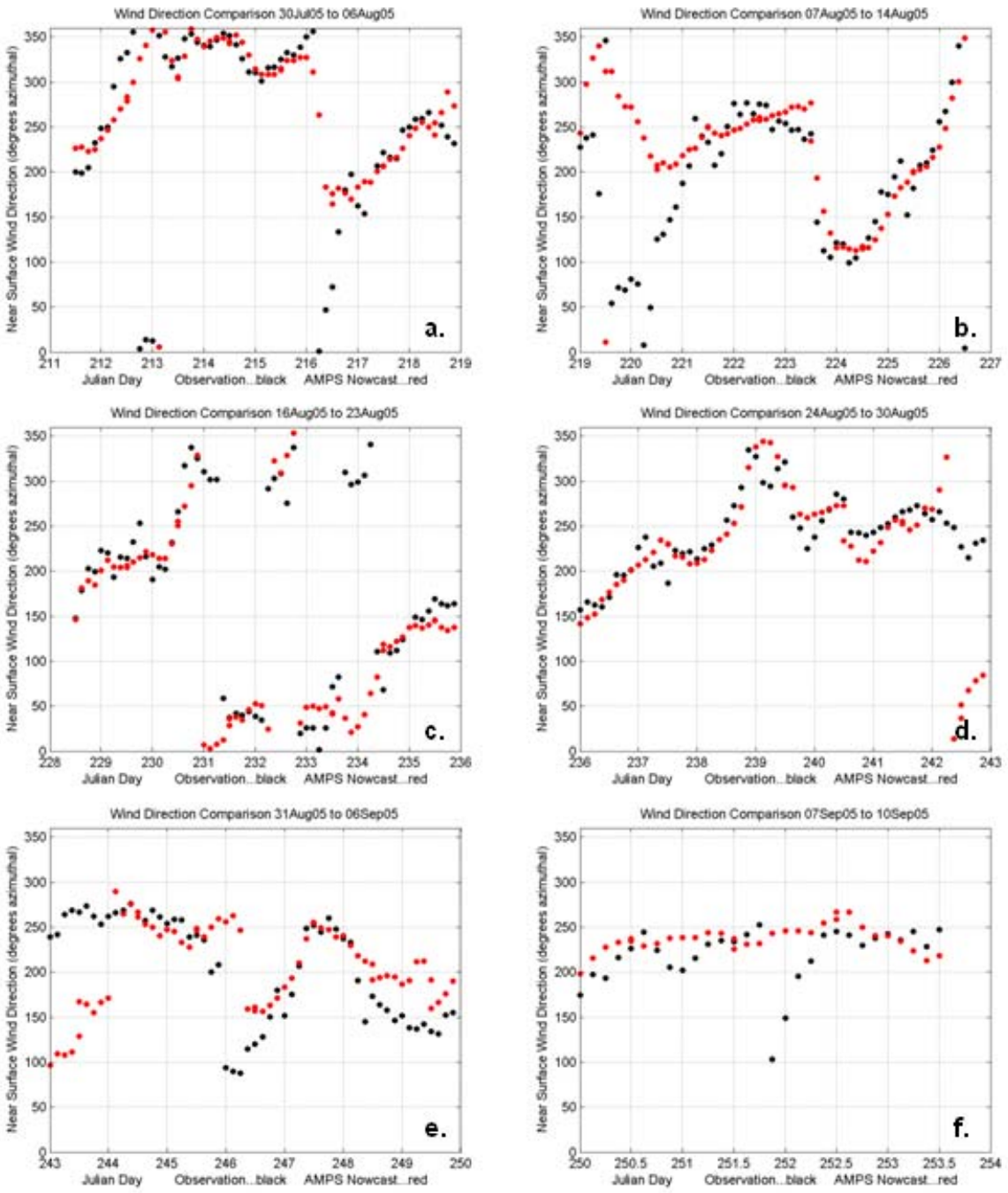

Figure 29. Near surface wind direction weekly time series. Black line is observational data and red line is AMPS data. a.) 30Jul05 to 06Aug05, b.) 07Aug05 to 14Aug05, c.) 16Aug05 to 23Aug05, d.) 24Aug05 to 30Aug05, e.) 31Aug05 to 06Sep05, and f.) 07Sep05 to 10Sep05.

Figure 30. Scatter plot of observed versus modeled near surface wind direction with correlation line equal to one drawn.

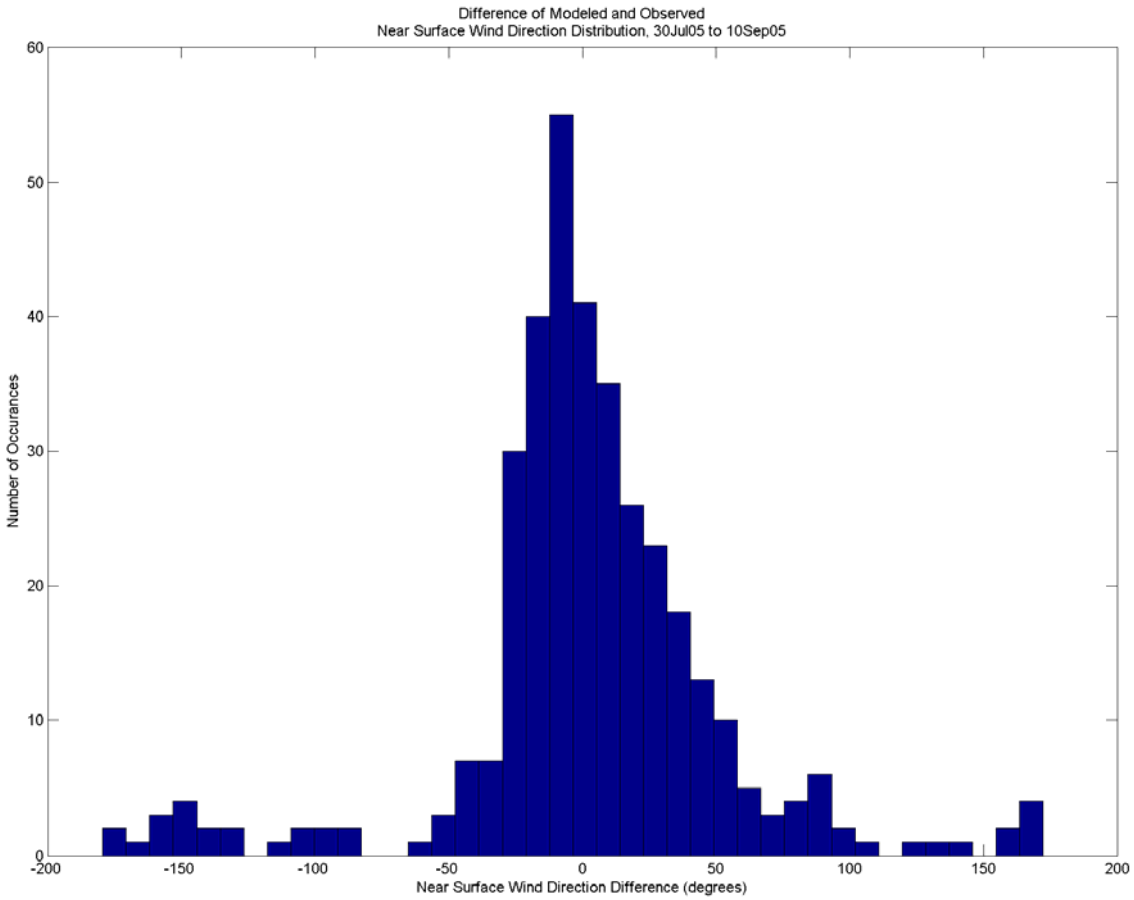

Figure 31. Distribution plot of AMPS near surface wind direction minus observation near surface wind direction.

	Number of data points	Mean	Median	RMS Error
AMPS Wind Direction (degrees)	360	215.1103	229.5342	80.01
Observation Wind Direction (degrees)	360	214.8948	231.92	81.6885

Table 15. Mean, median, and root mean squared values for AMPS derived near surface wind direction (row one) and observation near surface wind direction (row two).

7. Downwelling Long Wave Radiation

AMPS long wave radiation forecasts were found to have no correlation with observed. Time series plots are shown in Figures 32 and 33, scatter plot in Figure 34, and

differential distribution density plot in Figure 35. As can be seen in Figure 34 AMPS had no skill in forecasting long wave radiation. Basic statistics and correlation calculations (Tables 16 and 17) confirm this.

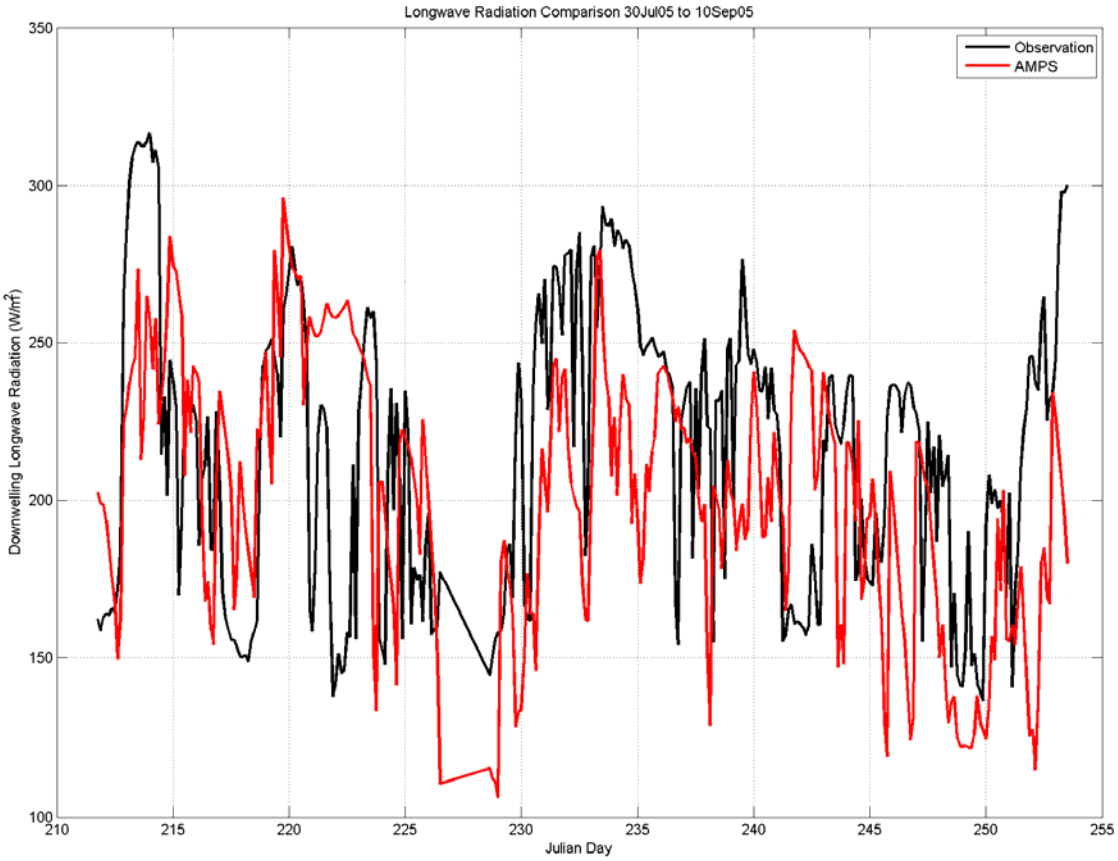

Figure 32. Downwelling long wave radiation time series 30 July 2005 to 10 September 2005. Black line is observational data and red line is AMPS data.

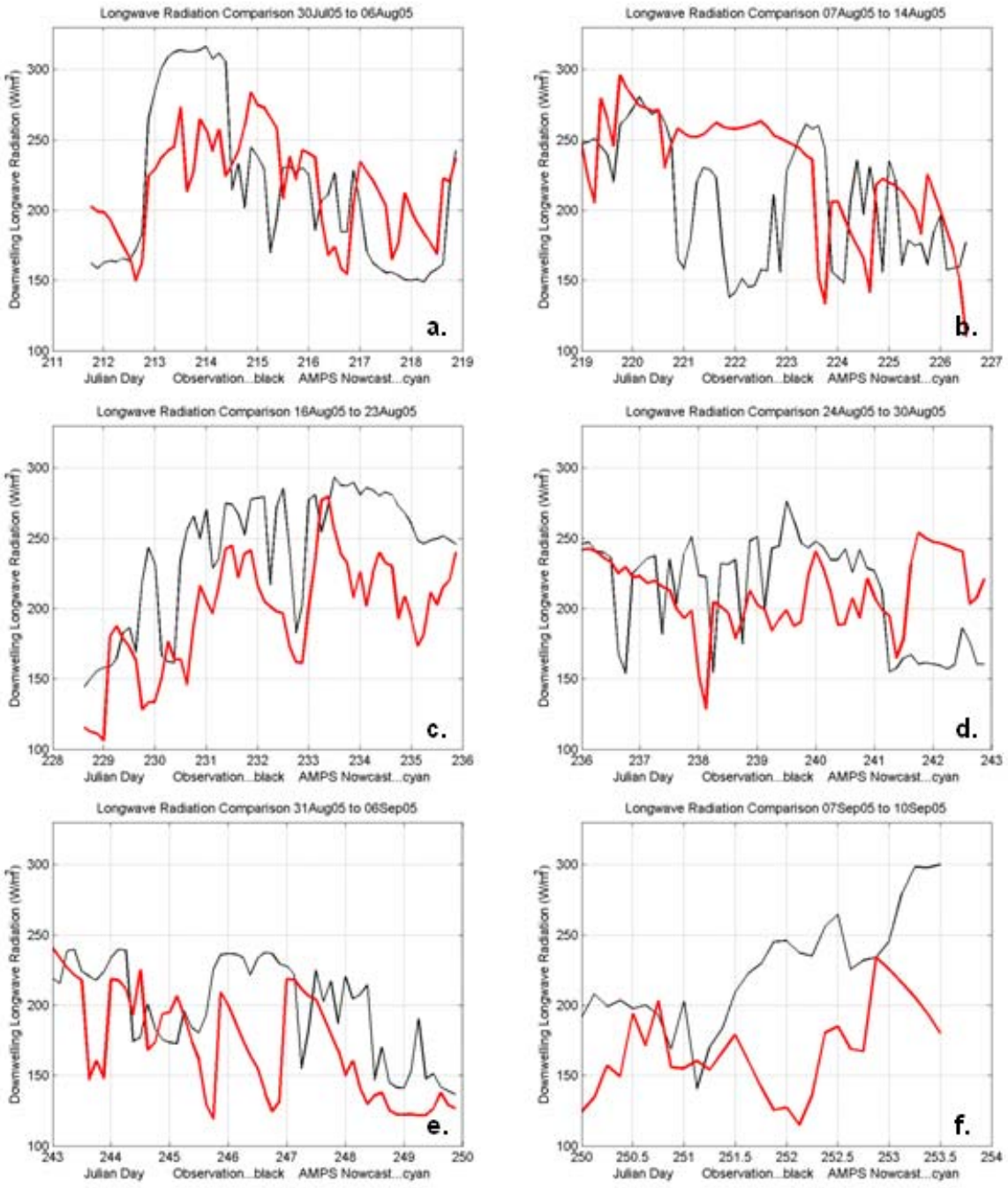

Figure 33. Downwelling long wave radiation weekly time series. Black line is observational data and red line is AMPS data. a.) 30Jul05 to 06Aug05, b.) 07Aug05 to 14Aug05, c.) 16Aug05 to 23Aug05, d.) 24Aug05 to 30Aug05, e.) 31Aug05 to 06Sep05, and f.) 07Sep05 to 10Sep05.

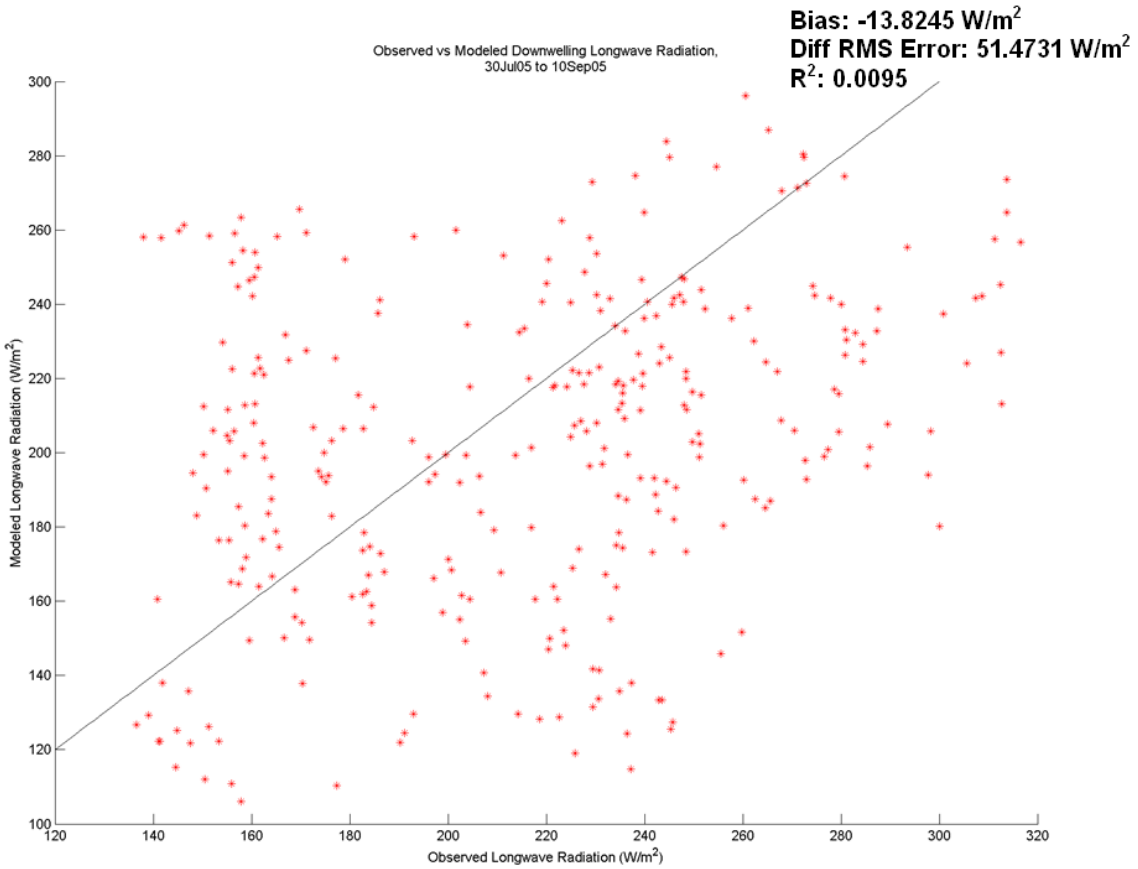

Figure 34. Scatter plot of observed versus modeled downwelling long wave radiation with correlation line equal to one drawn. Values for bias, differential root mean squared error, and correlation coefficient squared (R^2) are shown in the upper right hand corner.

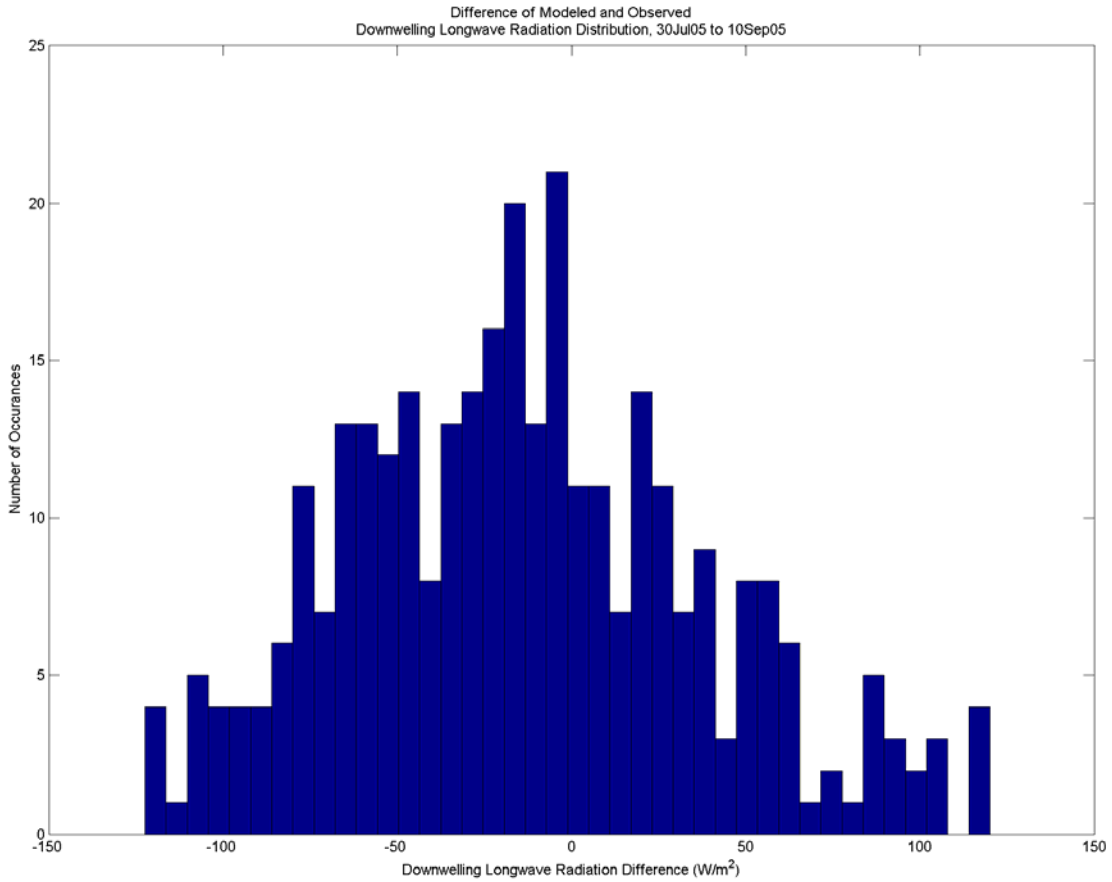

Figure 35. Distribution plot of AMPS downwelling long wave radiation minus observation downwelling long wave radiation.

	Number of data points	Min	Max	Mean	Median	RMS Error
AMPS Downwelling Long Wave Radiation (W/m^2)	319	106.0907	296.1095	201.7034	205.1429	41.9733
Observation Downwelling Long Wave Radiation (W/m^2)	319	136.6	316.6	215.5279	223.5	45.6767

Table 16. Minimum, maximum, mean, median, and root mean squared values for AMPS derived downwelling long wave radiation (row one) and observation downwelling long wave radiation (row two).

	Number of data points	Min	Max	Bias	MS Diff Error	R	R^2
AMPS LW Radn minus Ob LW Radn (W/m^2)	319	-122.389	120.0858	-13.8245	51.4731	0.0977	0.0095

Table 17. Minimum, maximum, bias, differential mean squared error, correlation coefficient (R), and correlation coefficient squared (R^2) for AMPS minus observation downwelling long wave radiation.

8. Downwelling Short Wave Radiation

Figures 36 and 37 show good overlap of AMPS forecast downwelling short wave radiation compared to observed downwelling short wave radiation. One feature to note in these figures are several times where AMPS forecast negative values for short wave radiation (particularly Julian days 258 to 251). It is unknown why this occurred and was not corrected for in statistical calculations (Tables 18 and 19). A scatter plot of observed versus AMPS forecast downwelling radiation is shown in Figure 38. Differential distribution density (Figure 39) shows the majority of differences are slightly positive. These plots, as well as a correlation coefficient of 0.7891 (Table 19), tend to indicate AMPS showed high skill in forecasting downwelling short wave radiation.

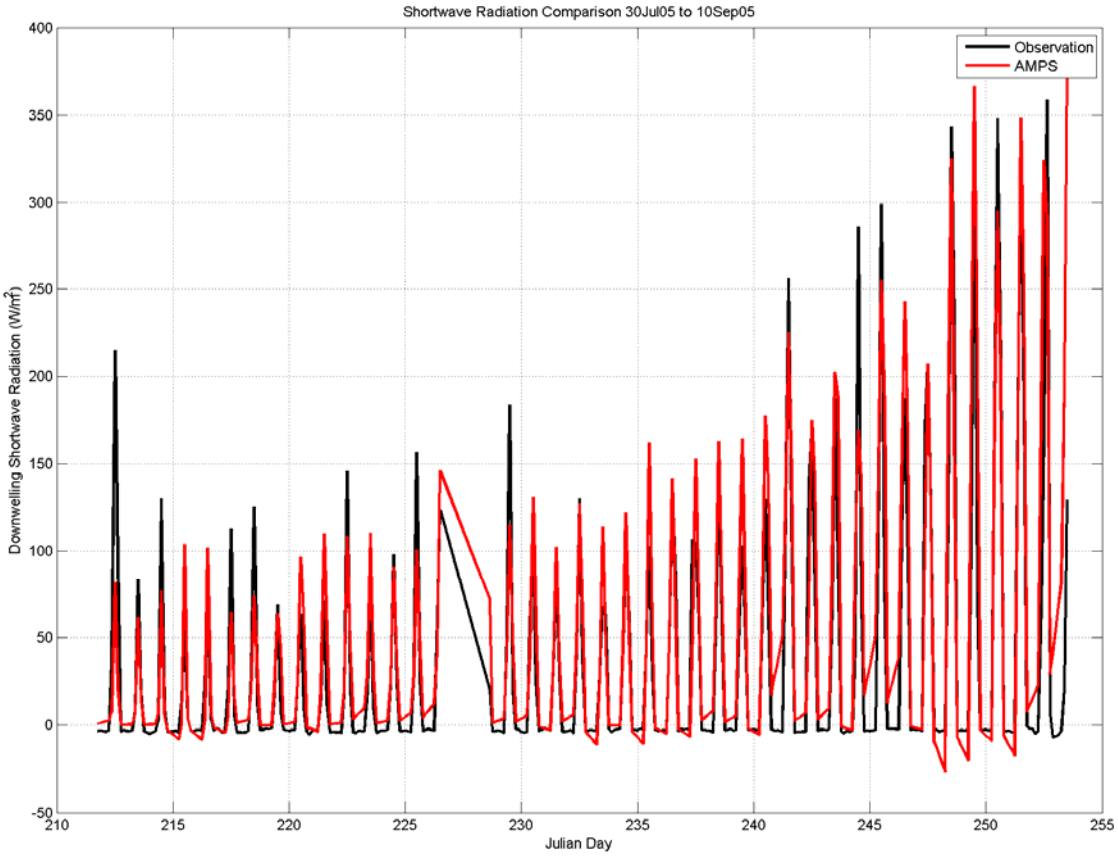

Figure 36. Downwelling short wave radiation time series 30 July 2005 to 10 September 2005. Black line is observational data and red line is AMPS data.

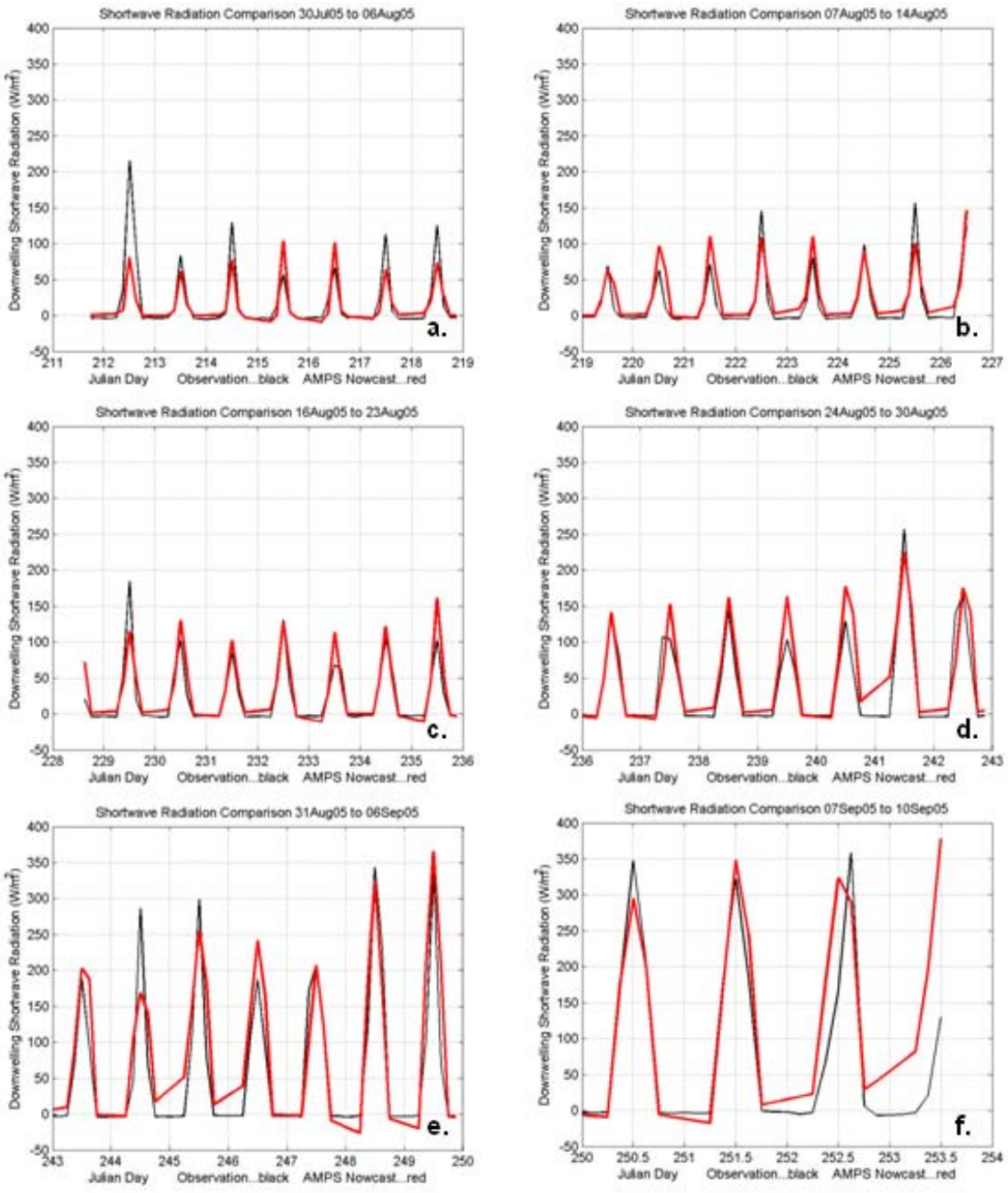

Figure 37. Downwelling short wave radiation weekly time series. Black line is observational data and red line is AMPS data. a.) 30Jul05 to 06Aug05, b.) 07Aug05 to 14Aug05, c.) 16Aug05 to 23Aug05, d.) 24Aug05 to 30Aug05, e.) 31Aug05 to 06Sep05, and f.) 07Sep05 to 10Sep05.

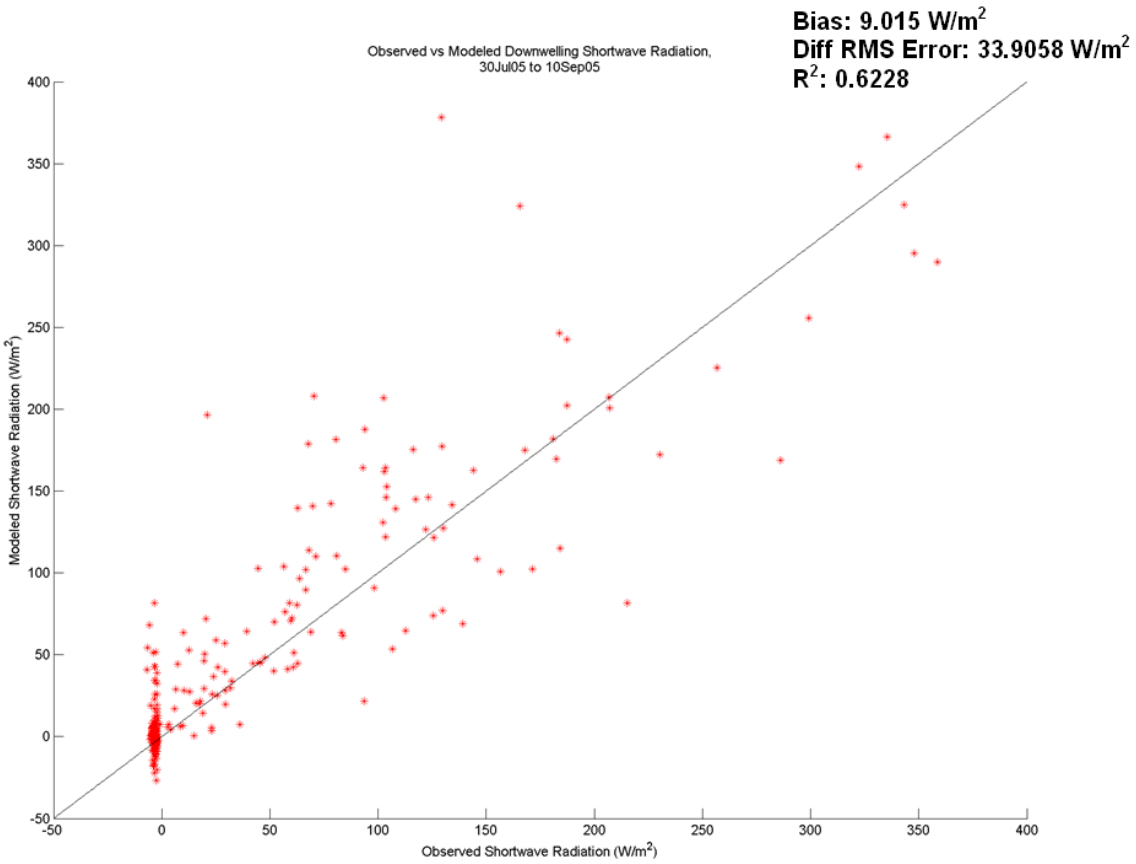

Figure 38. Scatter plot of observed versus modeled downwelling short wave radiation with correlation line equal to one drawn. Values for bias, differential root mean squared error, and correlation coefficient squared (R^2) are shown in the upper right hand corner.

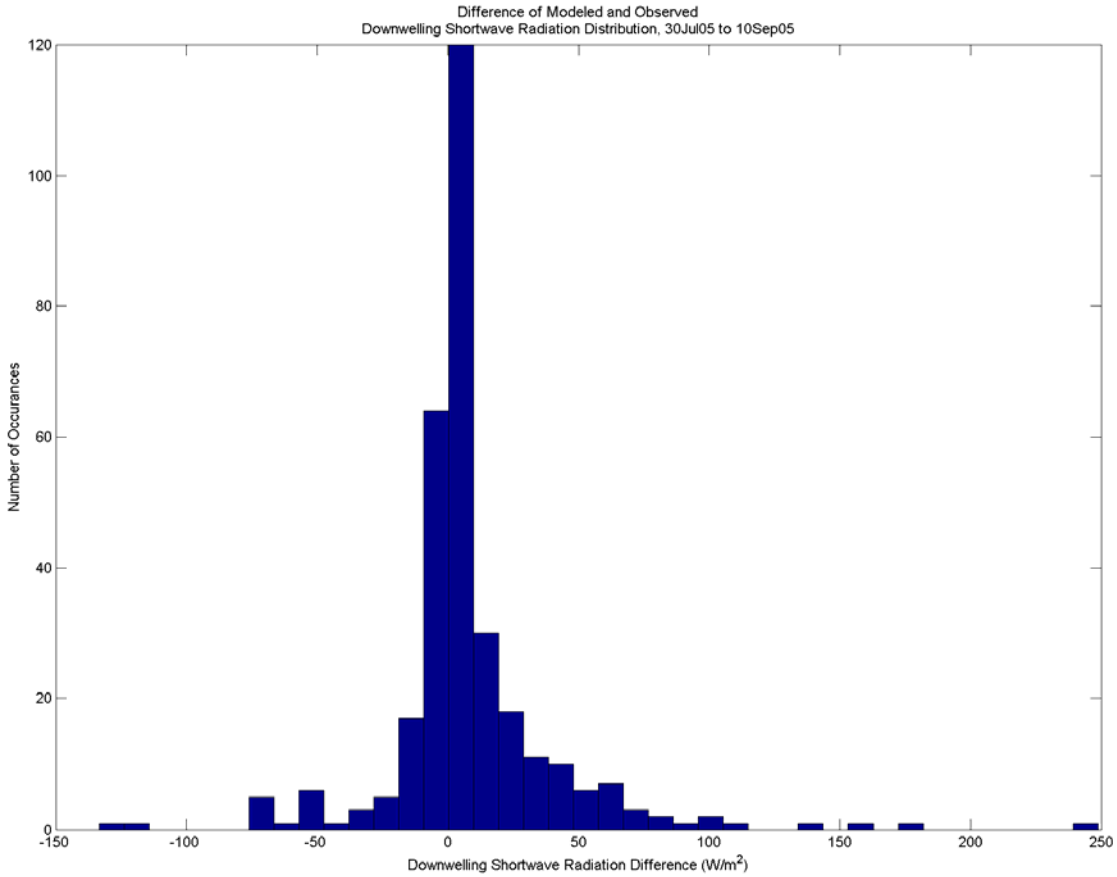

Figure 39. Distribution plot of AMPS downwelling short wave radiation minus observation downwelling short wave radiation.

	Number of data points	Min	Max	Mean	Median	RMS Error
AMPS Downwelling Short Wave Radiation (W/m^2)	319	-26.5966	378.1499	42.1284	5.4396	73.4132
Observation Downwelling Short Wave Radiation (W/m^2)	319	-6.963	358.6	33.1134	-2.631	68.8514

Table 18. Minimum, maximum, mean, median, and root mean squared values for AMPS derived downwelling short wave radiation (row one) and observation downwelling short wave radiation (row two).

	Number of data points	Min	Max	Bias	MS Diff Error	R	R^2
AMPS SW Radn minus Ob SW Radn (W/m^2)	319	-133.353	248.7499	9.015	33.9058	0.7891	0.6228

Table 19. Minimum, maximum, bias, differential mean squared error, correlation coefficient (R), and correlation coefficient squared (R^2) for AMPS minus observation downwelling short wave radiation.

9. Latent and Sensible Heat Fluxes

The AMPS forecast model provides direct latent and sensible heat flux outputs. For this research observed heat fluxes were calculated using the bulk method. In addition, AMPS bulk parameters (relative humidity, wind speed, air temperature, and surface pressure) were used to calculate modeled heat fluxes by the bulk method. Time series plots (Figures 40, 41, 46, and 47) display AMPS direct heat flux output (red), observed bulk method (black) and AMPS bulk method (cyan). As can be seen in these plots, bulk method values tend to be similar, while model output appears to have no correlation at all. The problem with this evaluation is that for the bulk methods, surface temperature for ice is assumed to be air temperature (no direct surface temperature measurements were obtained).

Ice and ocean heat fluxes calculated by bulk methods were then combined into a total flux using a weighted average based on percent ice cover and open ocean (85% and 15% respectively). For example, the calculation for sensible heat flux was:

$$shf_{total} = (.85)(shf_{ice}) + (.15)(shf_{ocean}) \qquad (2)$$

where shf_{total}, shf_{ice}, and shf_{ocean} are total, ice, and ocean sensible heat fluxes respectively. When assuming surface temperature is equal to near surface air temperature, all of the sensible heat flux (and most of the latent) are derived from the open ocean. Another issue was the percentages of ice cover and open ocean were kept constant, when in reality they were variable. Direct model output of heat fluxes showed more variability than bulk methods because surface temperature was not fixed to near

surface air temperature. Bulk method calculations were conducted using a program written by Dr. Peter Guest of the Naval Postgraduate School Department of Meteorology.

Scatter plots were created for observed bulk method versus direct model output (Figures 42 and 48) and observed bulk method versus model bulk method (Figures 43 and 49). As expected, observation versus direct AMPS output indicated no skill, while observed versus model bulk methods showed a correlation. Differential distribution density plots (Figures 44, 45, 50, and 51) and basic statistics and correlations (Tables 20, 21, 22 and 23) show the same results.

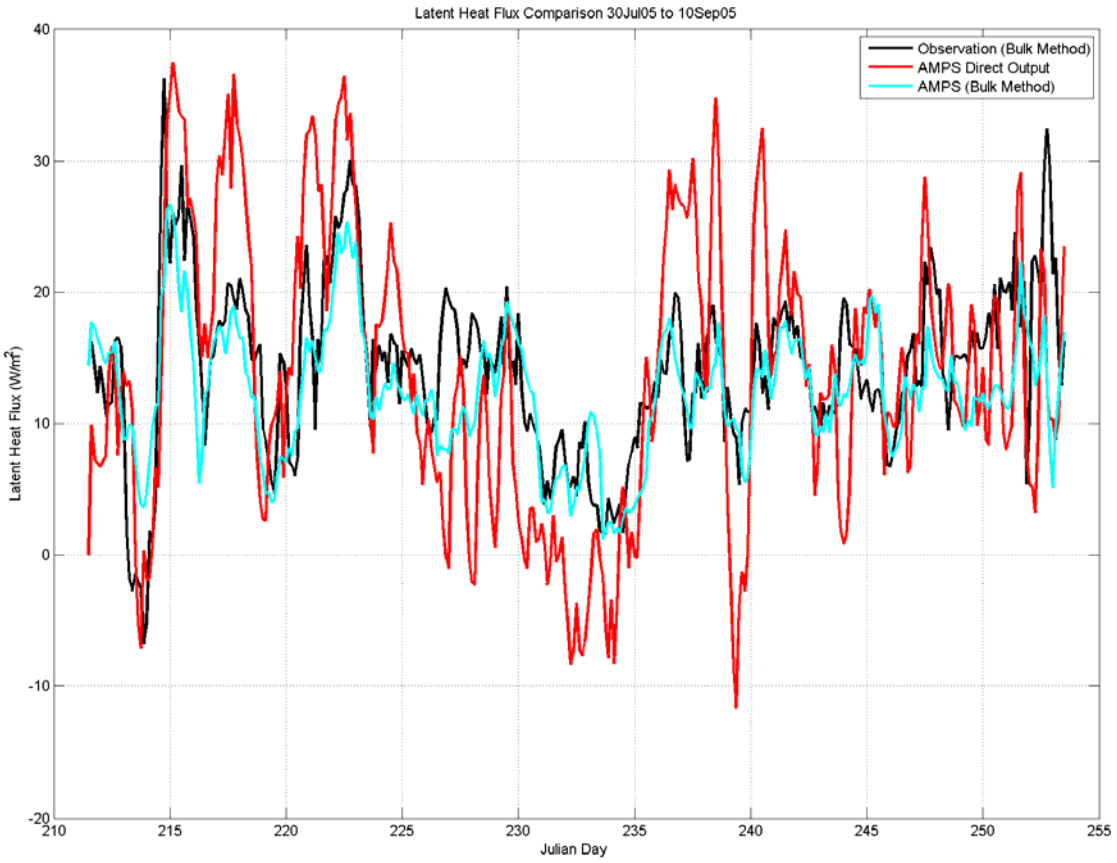

Figure 40. Latent Heat Flux time series 30 July 2005 to 10 September 2005. Black line is observational data, red line is AMPS latent heat flux output, and cyan line is latent heat flux calculated by bulk methods using AMPS model output for bulk parameters.

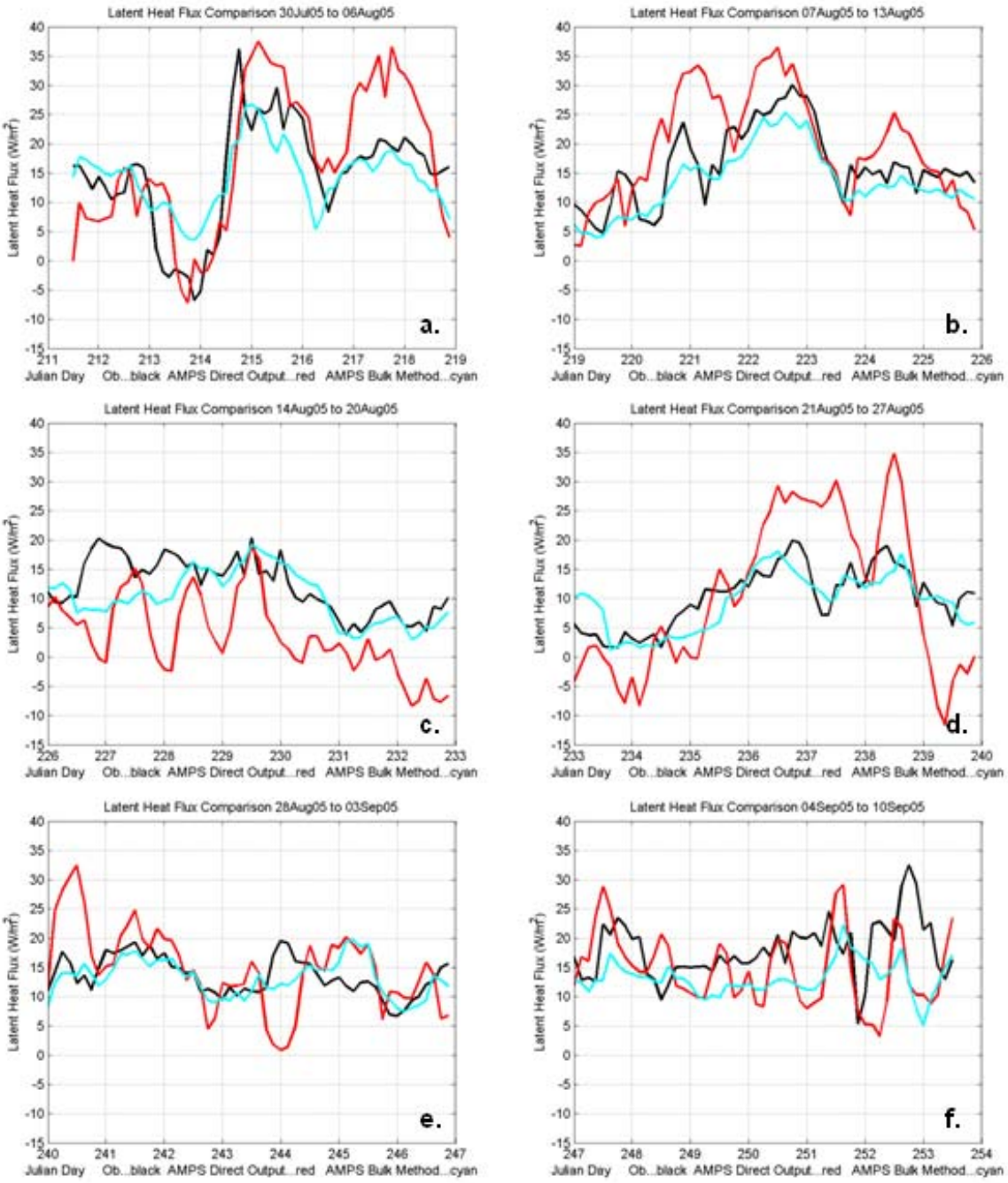

Figure 41. Latent heat flux weekly time series. Black line is observational data, red line is AMPS latent heat flux output, and cyan line is latent heat flux calculated by bulk methods using AMPS model output for bulk parameters. a.) 30Jul05 to 06Aug05, b.) 07Aug05 to 13Aug05, c.) 14Aug05 to 20Aug05, d.) 21Aug05 to 27Aug05, e.) 28Aug05 to 03Sep05, and f.) 04Sep05 to 10Sep05.

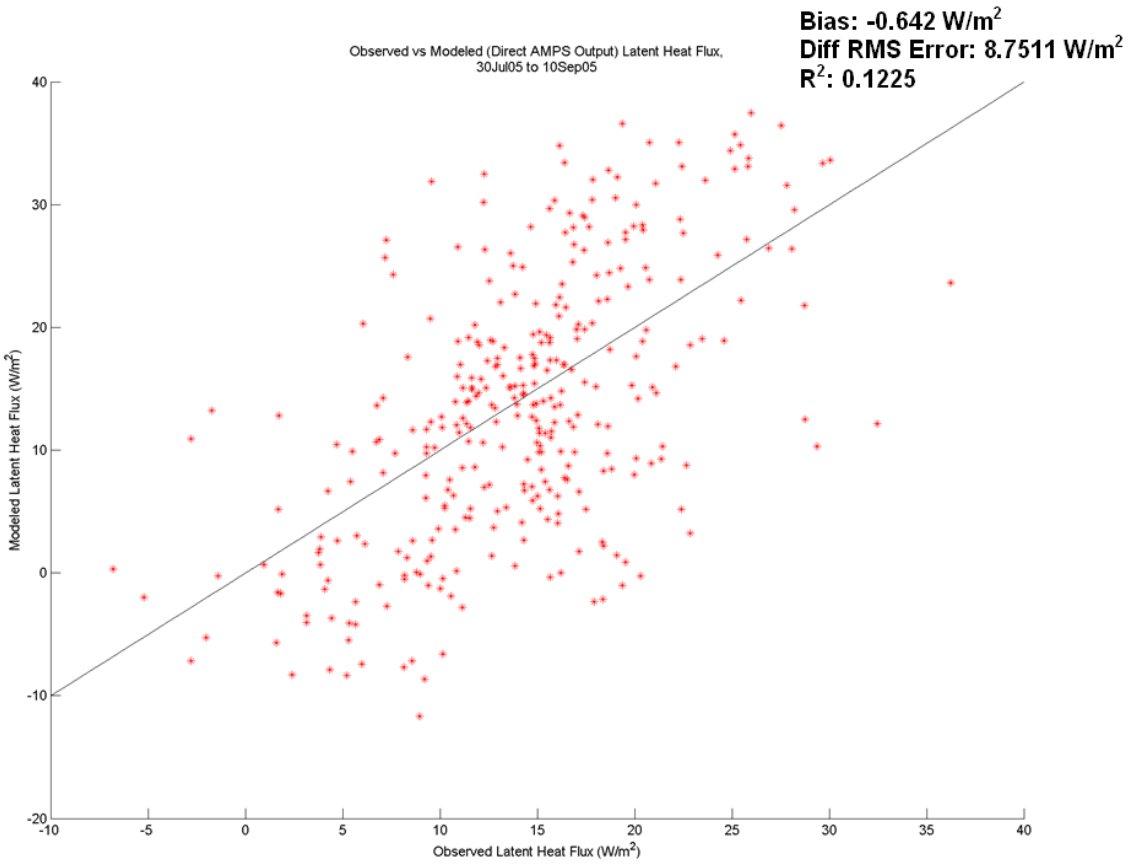

Figure 42. Scatter plot of observed versus modeled latent heat flux (direct AMPS output) with correlation line equal to one drawn. Values for bias, differential root mean squared error, and correlation coefficient squared (R^2) are shown in the upper right hand corner.

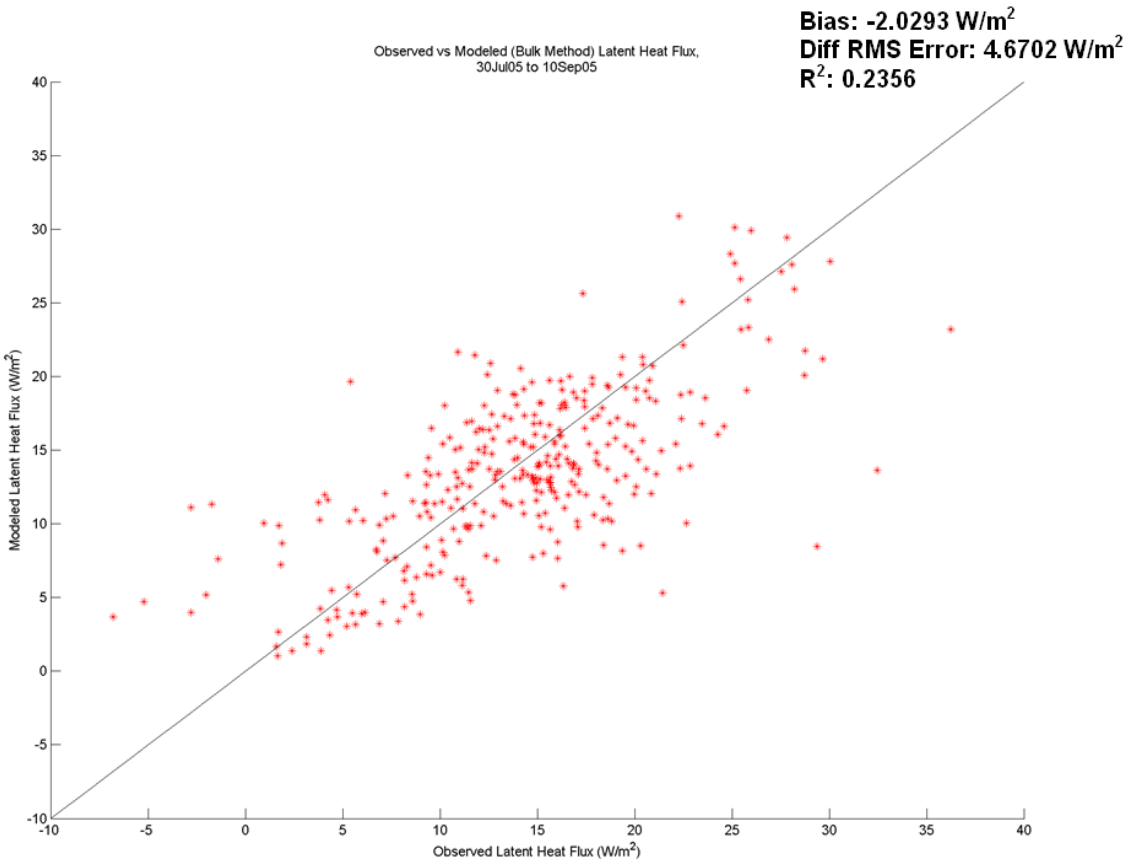

Figure 43. Scatter plot of observed versus modeled latent heat flux (calculated by bulk method using AMPS model output for bulk parameters) with correlation line equal to one drawn. Values for bias, differential root mean squared error, and correlation coefficient squared (R^2) are shown in the upper right hand corner.

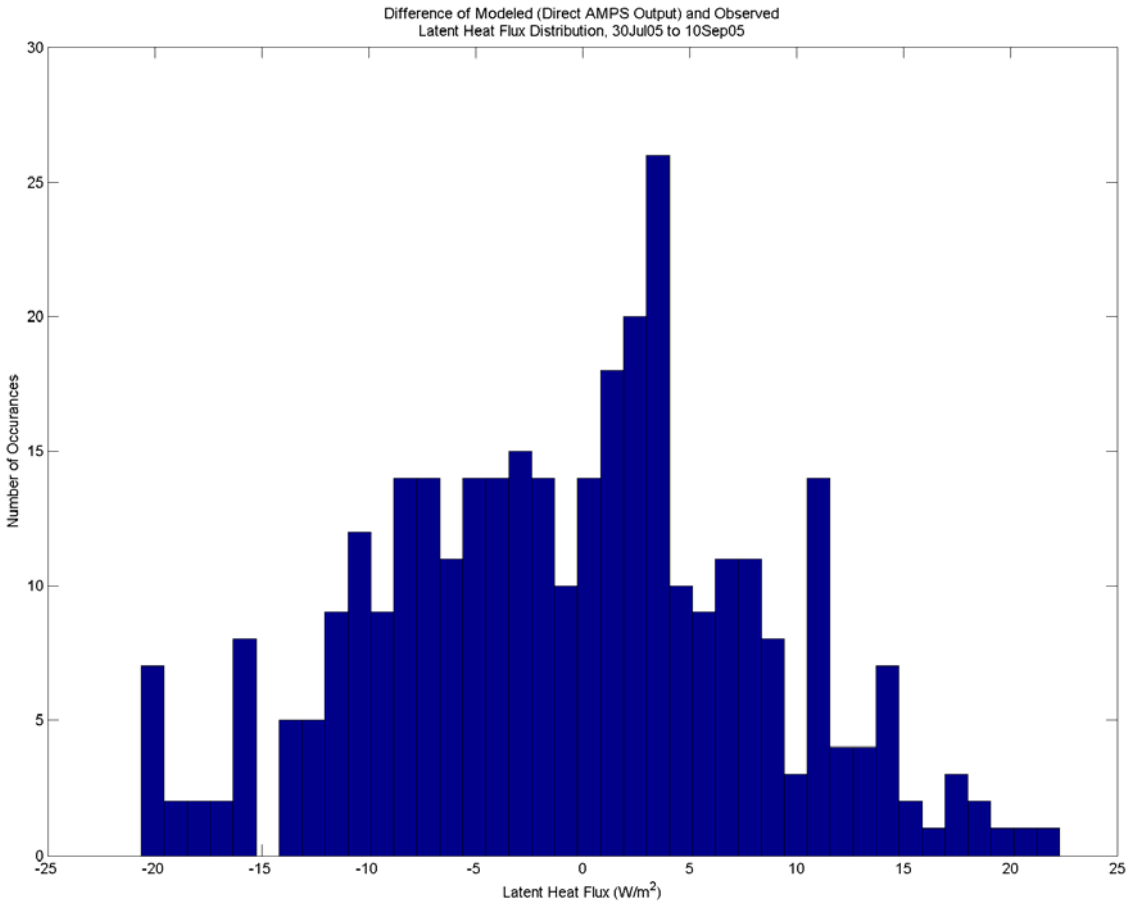

Figure 44. Distribution plot of AMPS latent heat flux (direct model output) minus observation latent heat flux.

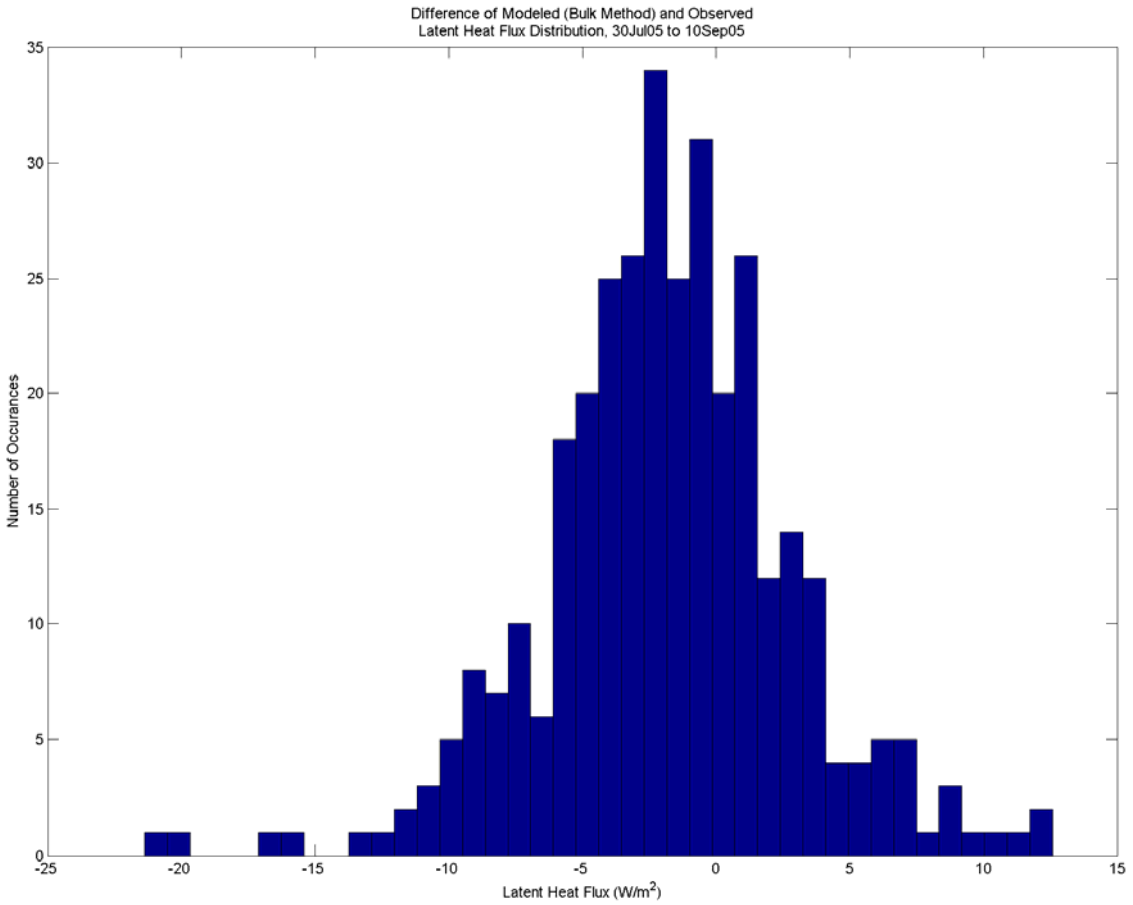

Figure 45. Distribution plot of AMPS latent heat flux (calculated by bulk method using AMPS model output for bulk parameters) minus observation latent heat flux.

	Number of data points	Min	Max	Mean	Median	RMS Error
AMPS Latent Heat Flux, Model Output (W/m^2)	337	-11.6854	37.4711	13.5072	13.2429	10.8533
AMPS Latent Heat Flux, Bulk Method (W/m2)	337	1.2293	26.6983	12.3249	12.4332	4.841
Observation Latent Heat Flux (W/m^2)	337	-6.7852	36.2324	14.1492	14.7403	6.5025

Table 20. Minimum, maximum, mean, median, and root mean squared values for AMPS derived (direct model output) latent heat flux (row one), AMPS derived (calculated by bulk method using AMPS model output for bulk parameters) latent heat flux (row two) and observation latent heat flux (row three).

	Number of data points	Min	Max	Bias	MS Diff Error	R	R^2
AMPS LHF minus Ob LHF (W/m^2)	337	-20.6235	22.3135	-0.642	8.7511	0.3499	0.1225
AMPS Bulk Method LHF minus Ob LHF (W/m2)	337	-21.3666	12.5859	-1.8243	4.6866	0.483	0.2333

Table 21. Minimum, maximum, bias, differential mean squared error, correlation coefficient (R), and correlation coefficient squared (R^2) for AMPS (direct model output) minus observation latent heat flux (row one), and AMPS (bulk method) minus observation latent heat flux (row two).

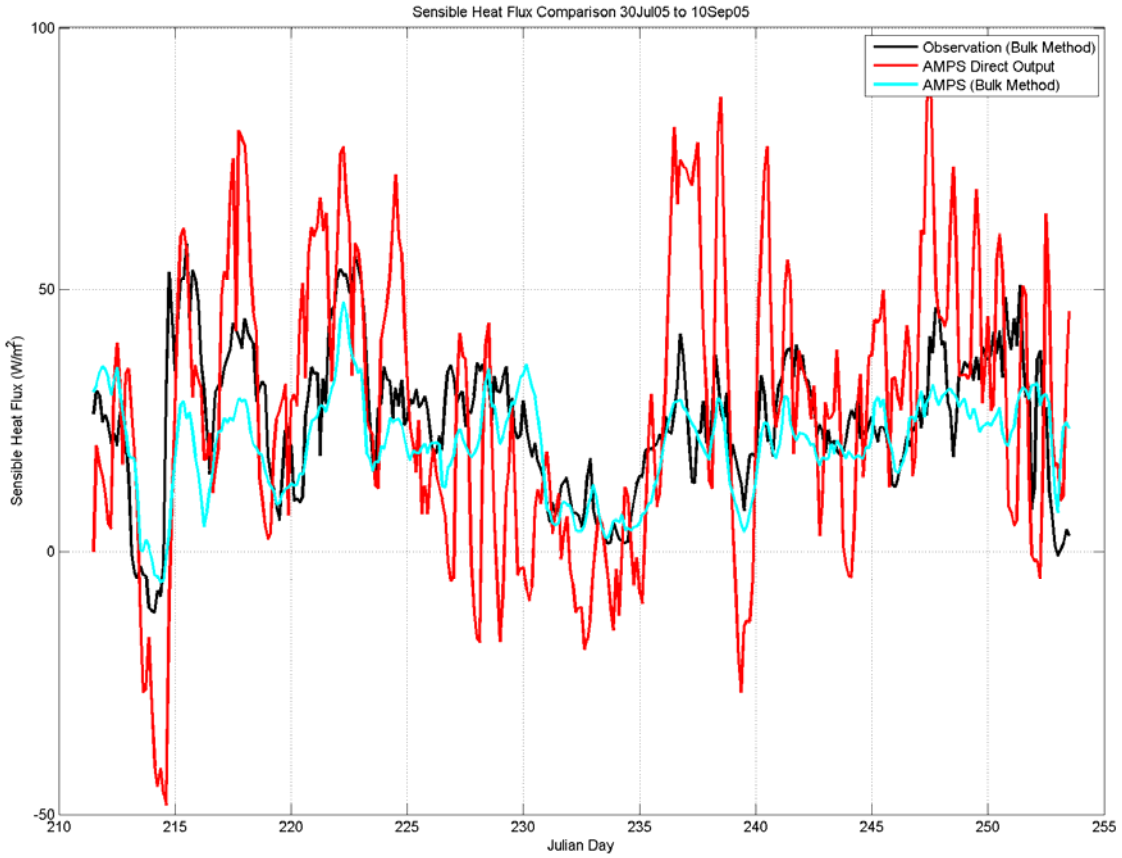

Figure 46. Sensible heat flux time series 30 July 2005 to 10 September 2005. Black line is observational data, red line is AMPS sensible heat flux output, and cyan line is sensible heat flux calculated by bulk methods using AMPS model output for bulk parameters.

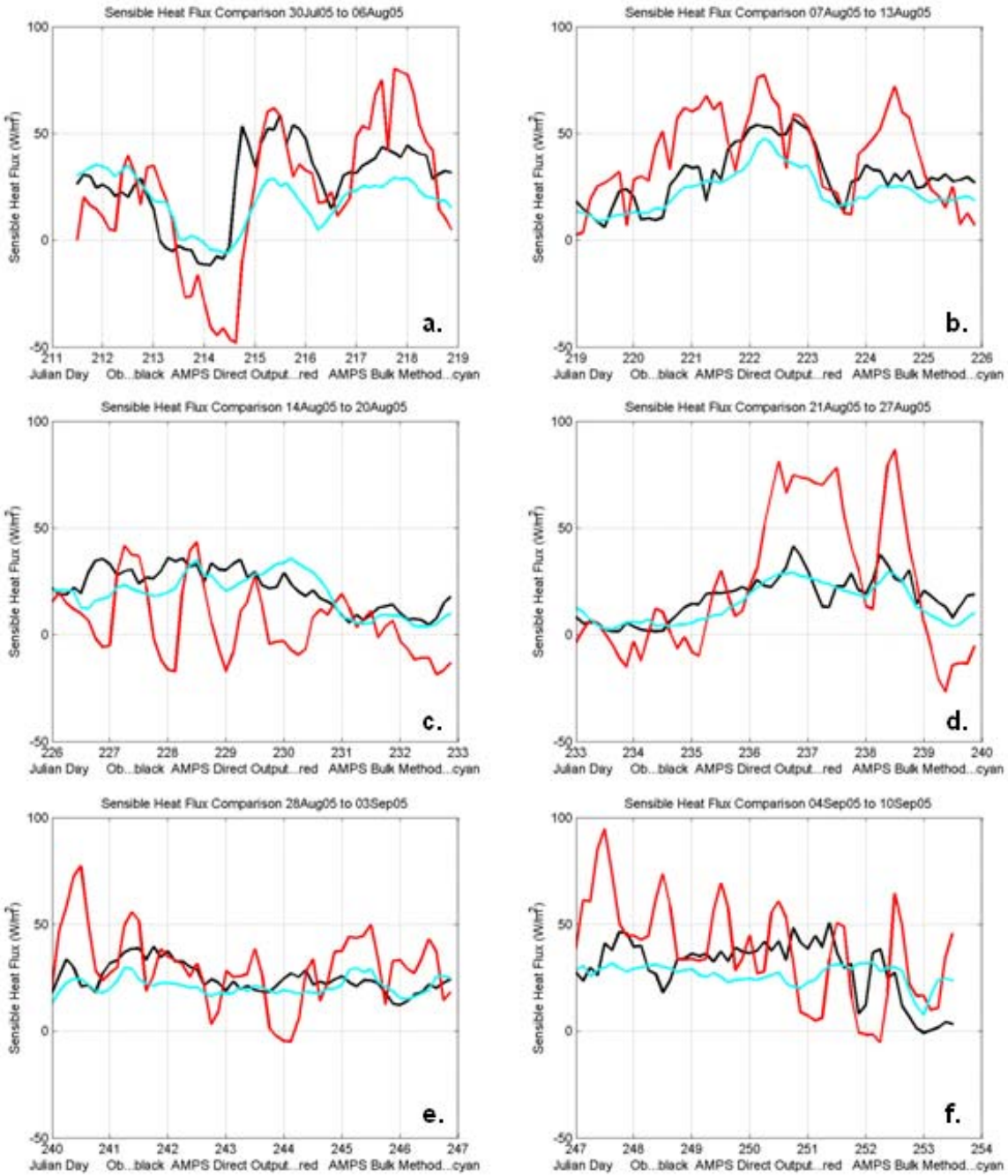

Figure 47. Sensible heat flux weekly time series. Black line is observational data, red line is AMPS sensible heat flux output, and cyan line is sensible heat flux calculated by bulk methods using AMPS model output for bulk parameters. a.) 30Jul05 to 06Aug05, b.) 07Aug05 to 13Aug05, c.) 14Aug05 to 20Aug05, d.) 21Aug05 to 27Aug05, e.) 28Aug05 to 03Sep05, and f.) 04Sep05 to 10Sep05.

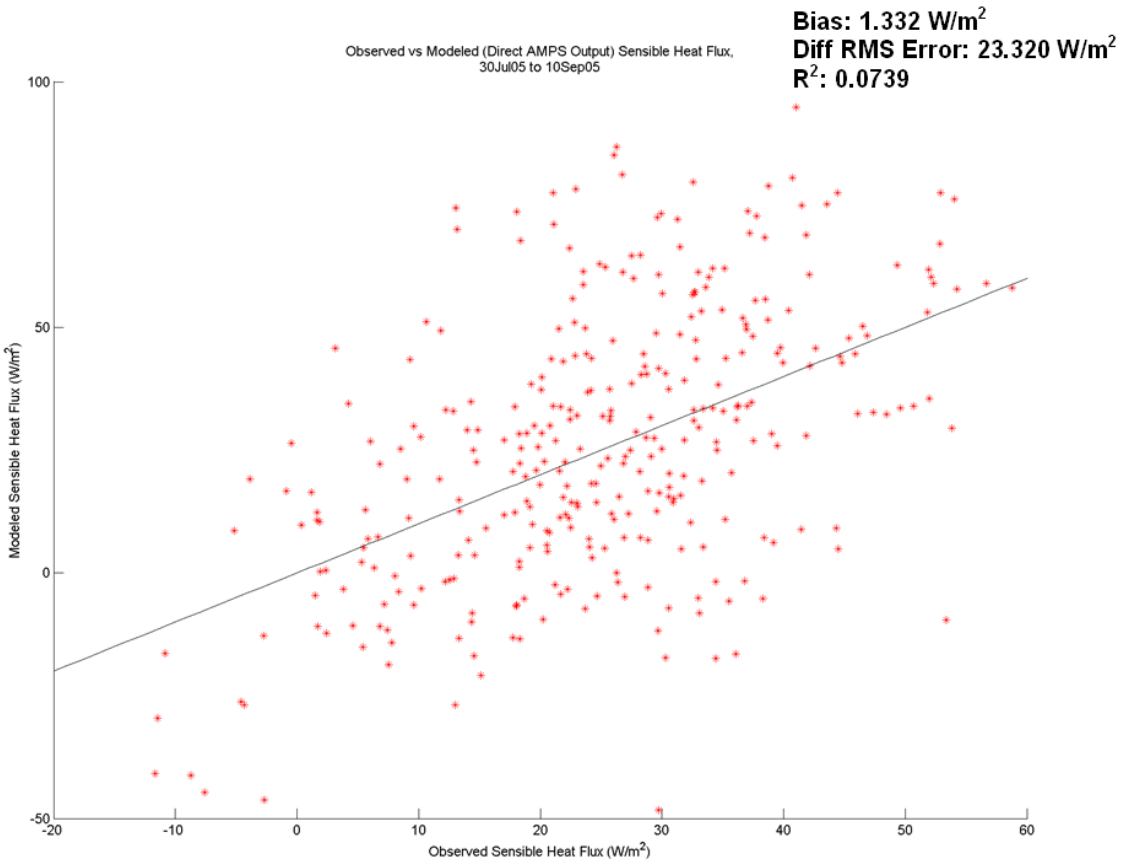

Figure 48. Scatter plot of observed versus modeled sensible heat flux (direct AMPS output) with correlation line equal to one drawn. Values for bias, differential root mean squared error, and correlation coefficient squared (R^2) are shown in the upper right hand corner.

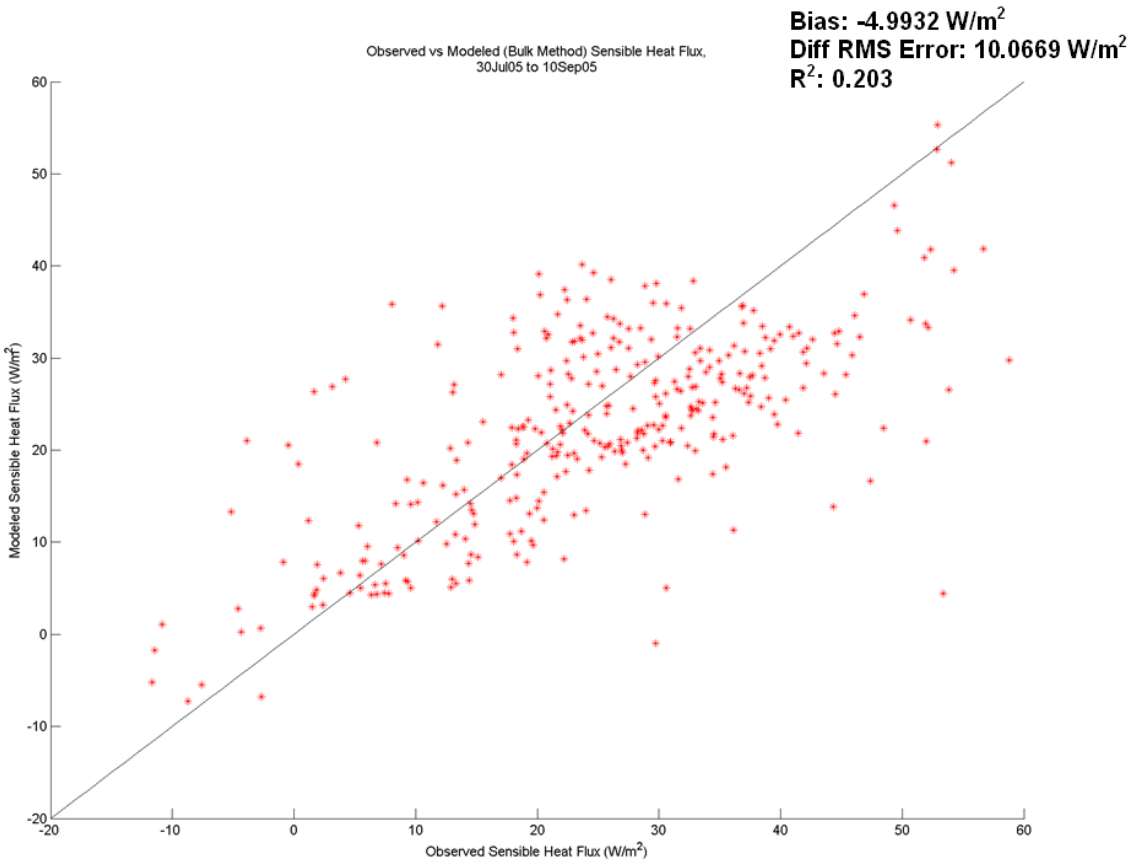

Figure 49. Scatter plot of observed versus modeled sensible heat flux (calculated by bulk method using AMPS model output for bulk parameters) with correlation line equal to one drawn. Values for bias, differential root mean squared error, and correlation coefficient squared (R^2) are shown in the upper right hand corner.

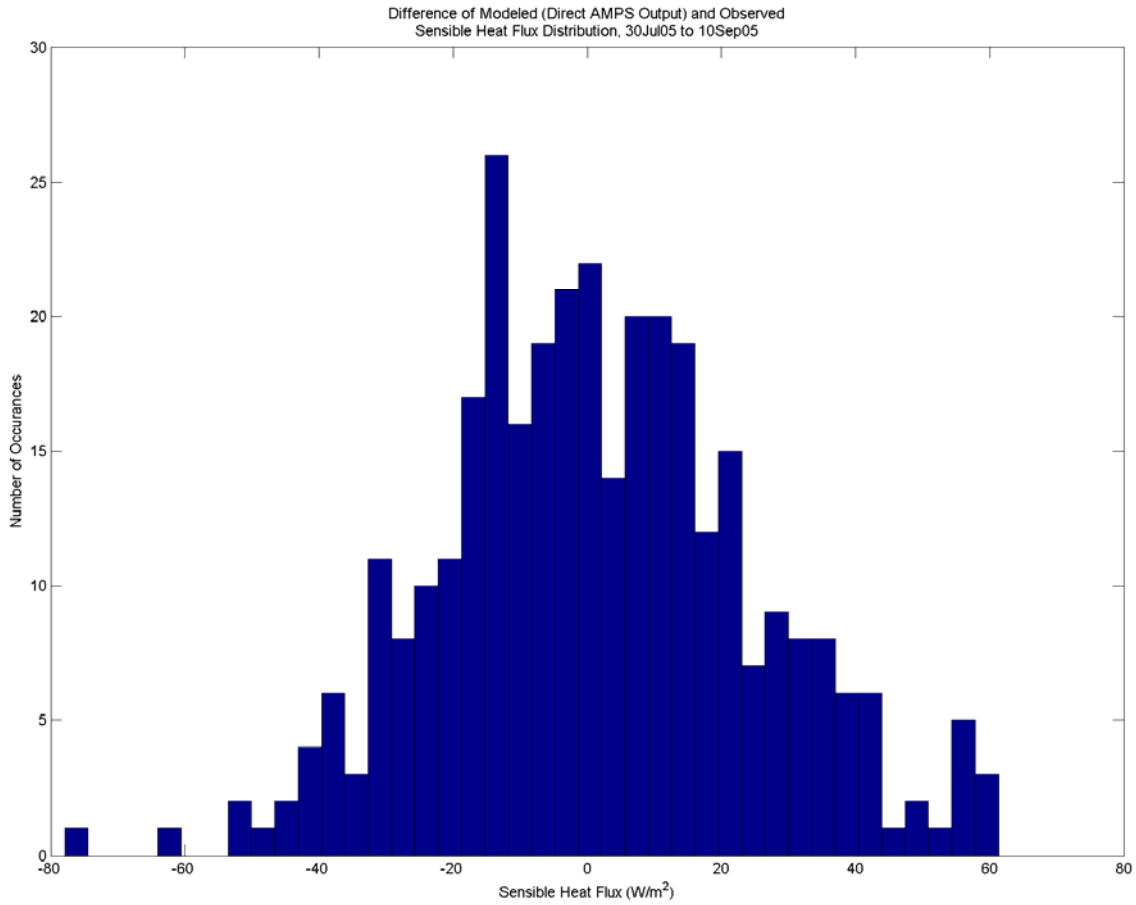

Figure 50. Distribution plot of AMPS sensible heat flux (direct model output) minus observation sensible heat flux.

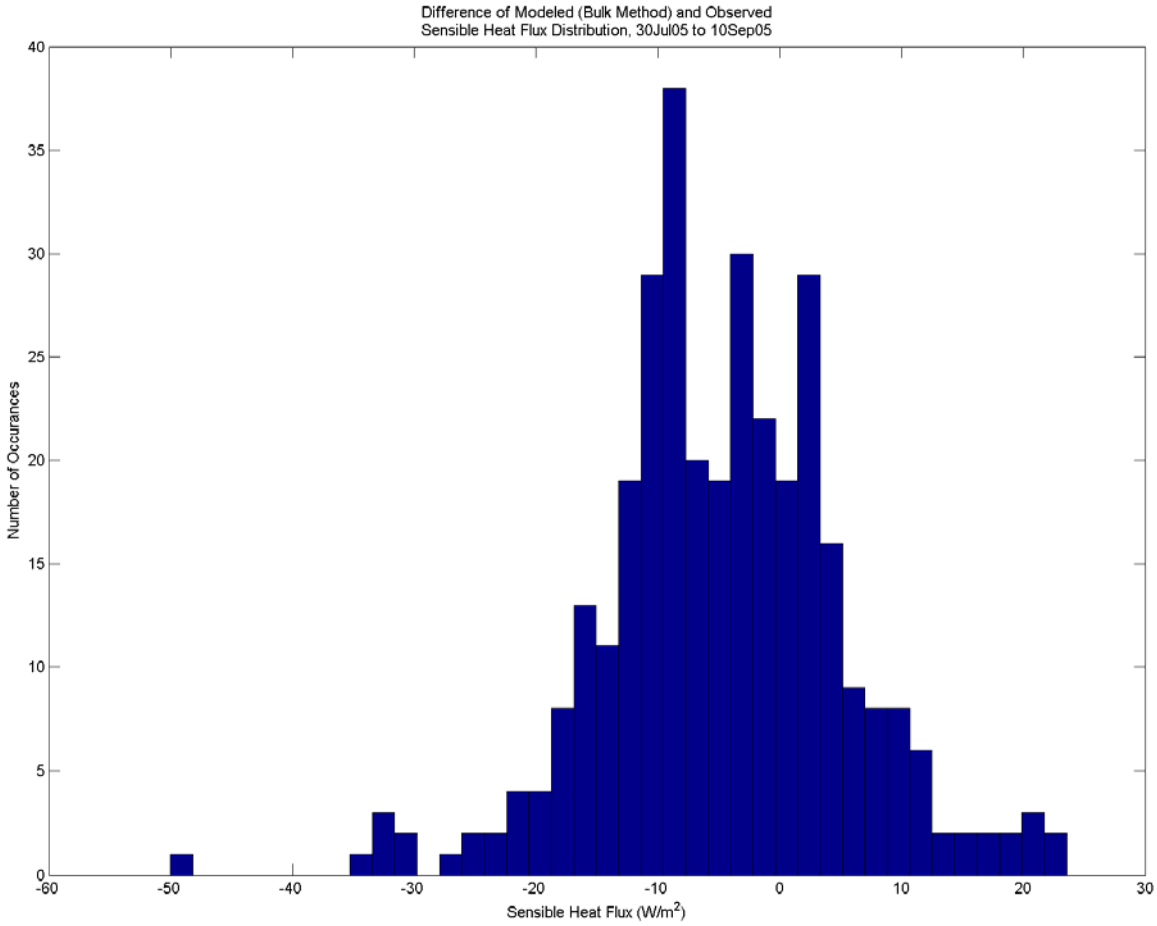

Figure 51. Distribution plot of AMPS sensible heat flux (calculated by bulk method using AMPS model output for bulk parameters) minus observation sensible heat flux.

	Number of data points	Min	Max	Mean	Median	RMS Error
AMPS Sensible Heat Flux, Model Output (W/m^2)	337	-48.2254	94.7855	26.3397	26.402	27.3168
AMPS Sensible Heat Flux, Bulk Method (W/m2)	337	-6.0896	47.6757	20.2441	21.1381	9.3373
Observation Sensible Heat Flux (W/m^2)	337	-11.6588	58.8124	25.0077	25.5618	13.5801

Table 22. Minimum, maximum, mean, median, and root mean squared values for AMPS derived (direct model output) sensible heat flux (row one), AMPS derived (calculated by bulk method using AMPS model output for bulk parameters) sensible heat flux (row two) and observation sensible heat flux (row three).

	Number of data points	Min	Max	Bias	MS Diff Error	R	R^2
AMPS SHF minus Ob SHF (W/m^2)	337	-77.929	61.3296	1.332	23.32	0.2718	0.0739
AMPS Bulk Method SHF minus Ob SHF (W/m2)	337	-50.0183	23.5586	-4.7636	10.0576	0.4517	0.2041

Table 23. Minimum, maximum, bias, differential mean squared error, correlation coefficient (R), and correlation coefficient squared (R^2) for AMPS (direct model output) minus observation sensible heat flux (row one), and AMPS (bulk method) minus observation senisble heat flux (row two).

D. COMPARISON CONCLUSIONS

AMPS surface pressure and relative humidity forecasts were found to have no skill when compared to observed values. It is believed this was due to AMPS handling of cloud and moisture parameters. It was also found that a slightly better relative humidity forecast could be obtained by simply setting relative humidity with respect to ice to saturation.

The skill of AMPS in predicting latent and sensible heat fluxes is unknown due to the broad assumptions made in calculating observed values with the bulk method. When AMPS bulk parameter inputs were used to calculate fluxes with the bulk method, the results were found to be similar with observed values (even with AMPS' lack of skill in forecasting relative humidity) because of the dependence of latent heat flux on specific humidity difference and wind speed.

AMPS near surface air temperature, and therefore specific humidity, were found to be over-forecast part of the time. The remaining parameters (surface pressure, wind speed and direction, and short wave radiation) performed well when compared to observed values. Surface pressure, wind speed and direction show that AMPS had a good performance in representing the synoptic situation.

When time series plots for near surface wind speed were compared with time series for surface pressure, it was noted that times when AMPS under-forecast wind speed tended to correspond to times when it over-forecast surface pressure. This led to the belief that AMPS also tended to slightly under-forecast the intensity of storms.

Residual scatter plot analysis was also performed for all parameters. This was accomplished by taking the difference of the value of a modeled parameter minus the observed value and comparing this difference to all other meteorological parameters (AMPS and observed) on a scatter plot. No significant correlations were found during this process.

THIS PAGE INTENTIONALLY LEFT BLANK

III. OCEAN MODEL

A. 1-D OCEAN MODEL

The ocean model used for this research is a simple one dimensional, ocean model developed by Dr. Miles McPhee. McPhee (2000) gives a detailed description of the model, which will not be restated here. Basically, the model ocean structure is initialized by a temperature-salinity profile (conductivity-temperature-depth (CTD) profiler cast data used for this research). Time series were created for surface friction velocity, ice heat conduction, and downwelling short wave radiation. These fields were then used to force the initialized conditions over a selected period of time.

It is important to note that only one CTD profile could be used to initialize the model for the entire run, regardless of the length of the model run. The actual ocean structure would not remain exactly the same over time, and, the research vessel did not remain in the location of the CTD profile cast. Other limitations of this model presented in McPhee (2000) are divergence of ice cover and Ekman transport in the mixed layer are neglected, and any assumption of horizontal homogeneity implicit in one dimension modeling, particularly in the Maud Rise region, are suspect.

These limitations would severely degrade ocean modeling requiring a high degree of accuracy. For the purposes of this research, modeling the ocean structure over the Maud Rise was not the goal. Sensitivity to changes in atmospheric forcing was desired, and the one-dimensional ocean model proved sufficient in that task.

B. COMPILATION OF DATA FOR USE IN MODEL

1. Model Constants

The following is a list of constants and their values used in the ocean model runs:

a. Model Depth

A model depth of 250 meters was chosen (pycnocline depth observed in CTD data was between 50 to 150 meters).

b. Undersurface Roughness Length (z_o)

Undersurface roughness length of 1.0 mm was used (McPhee 2007, personal communication).

c. Initial Ice Thickness

Initial average ice thickness over the Maud Rise area was set to 40 cm.

d. Heat transfer coefficient

Based on McPhee et al. (1999), a dimensionless heat transfer coefficient (Stanton number based on friction speed instead of mean speed) of 5.6×10^{-3} was used.

e. Latitude

Latitudes for model runes were the latitude of the CTD profile used to initialize the run.

f. Buoyancy Frequency Squared (N^2) Limit

Based on Mcphee (2000), a buoyancy frequency squared (N^2) limit of 1.5×10^{-5} s^{-2} was used. The pycnocline depth is defined as the depth in the water column where this value is first exceeded.

2. Model Variables

The following is a list that describes the variables used in the ocean model and how they were compiled.

a. Temperature/Salinity Profiles

Temperature and salinity profiles were obtained from three separate CTD downcast profiles at stations 1, 65, and 92 (reason for these cast selections is given below). Depth, primary temperature, and primary salinity data were taken from the casts and compiled into text files for input into the ocean model.

b. Downwelling Solar Radiation

Two downwelling solar radiation time series files were created from AMPS model output and observation data (AMPS downwelling short wave radiation and observed downwelling short wave radiation).

c. Friction Speed (u_*)

McPhee et al. (1999) characterize friction speed as the square root of kinematic stress at the interface. Using this definition, friction speed was calculated using the following equation:

$$u_* = \sqrt{\frac{\tau_{total}}{\rho_{sw}}} \tag{3}$$

where u_* is friction speed in meters/second, τ_{total} is wind stress in Newton/meters^2 (note that the wind stess is total wind stress over ice and seawater, taking into account the percent of ice cover), and ρ_{sw} is the density of seawater (1025 kilograms/meter^3 (kg/m^3) used).

Four separate wind stress time series were created using bulk methods for the following conditions:

-AMPS forecast wind speed

-Observational wind speed

-AMPS wind speed increased by a factor of two, and

-Observational wind speed increased by a factor of two.

(Weather conditions during MaudNESS were found to be unusually mild for a winter season in the Weddell Sea. For this reason, AMPS and observed wind speeds were increased by a factor of two in order to simulate more typical winter forcing conditions).

d. Ice Conductive Heat Flux ($\dot{q}$)

Ice conductive heat flux is defined by McPhee (1992) as heat conduction in ice divided by the product of density and specific heat of seawater. Using this definition, ice conductive heat flux was calculated using the following equation:

$$\dot{q} = \frac{q_{ice}}{\left((\rho_{sw})(c_{p_{sw}})\right)} \tag{4}$$

where $\dot{q}$ is ice conductive heat flux (meters-Celsius/second), q_{ice} is heat conduction in ice (with respect to ice temperature) in Watts/meter^2, ρ_{sw} is the density of seawater (1025 kg/m^3 used), and $c_{p_{sw}}$ is the specific heat capacity of seawater (Joules/kilogram-Celsius) at the seawater-ice interface.

Bulk methods were used to create heat conduction in ice time series for the same four scenarios described above. Specific heat capacity of seawater at the seawater-ice interface was calculated using interface values from the appropriate CTD profiles.

C. CTD STATIONS CHOSEN FOR MODEL RUNS

Figure 52 shows the bathymetry of the Maud Rise area and all the locations of the MaudNESS deployment Phase I CTD stations. The three highlighted CTD stations were the locations chosen for this study.

The temperature-salinity profiles were used to initialize the ocean model at the latitude and Julian day of the CTD cast (summarized in Table 24). The model was then run for seven days from the date of initialization, for each of the scenarios listed in the previous section.

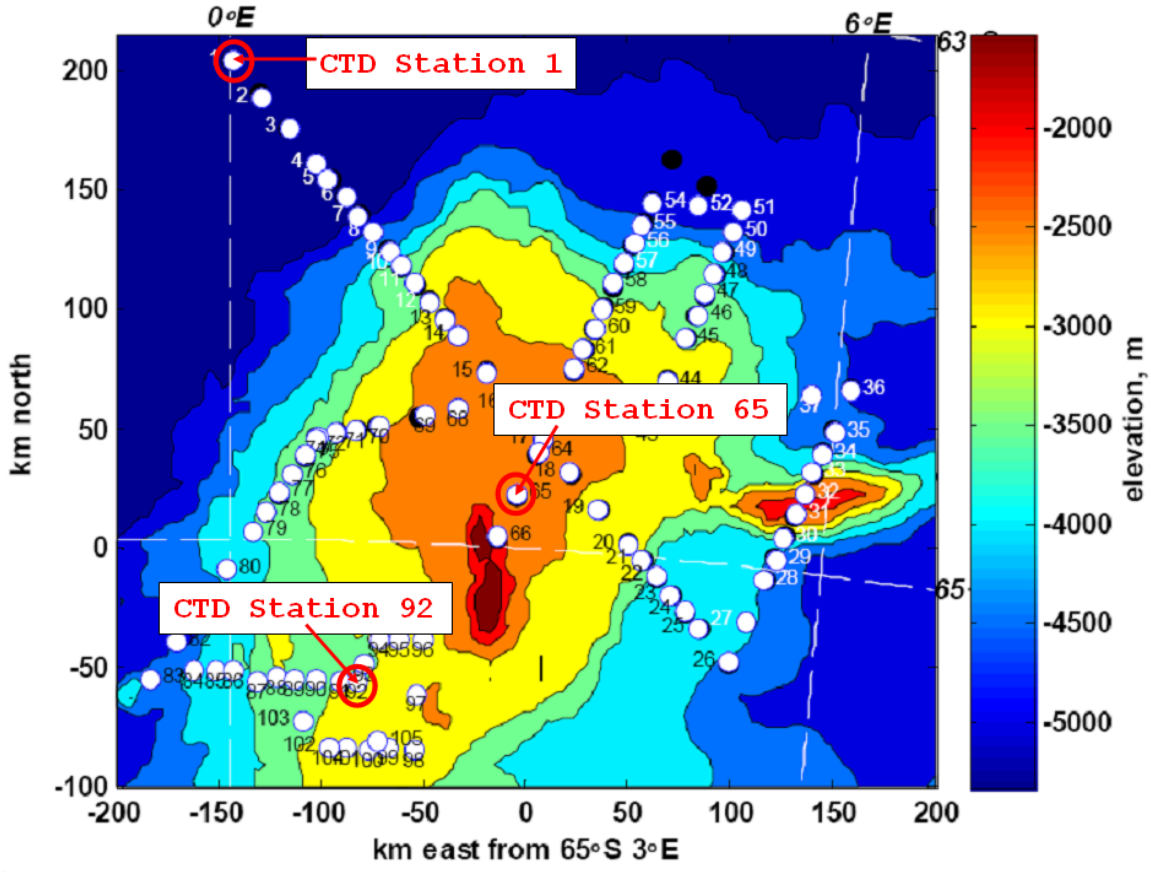

Figure 52. Maud Rise bathymetry and MaudNESS CTD stations. Location of CTD's used for ocean model initialization annotated. (After: Figure 8, MaudNESS Cruise Report)

CTD Station Number	Date	Time (Z)	Lat (dec)	Long (dec)
1	2-Aug-05	12:43:14	-63.236	0.01
65	9-Aug-05	5:09:28	-64.8	2.88
92	21-Aug-05	16:07:37	-65.515	1.312

Table 24. Date, time, latitude, and longitude data for CTD stations used in this study.

1. CTD Station 1

CTD station 1 was selected as the station farthest away from the Maud Rise. The water column at this location was relatively stable when compared to the other two locations. The potential density difference across the pycnocline was approximately 0.175 kg/m^3, as can be seen in Figure 53. There were also relatively large differences in potential temperature and salinity across the pycnocline (approximately 2.8 degrees Celsius (^{o}C) and 0.375 practical salinity units (psu) respectively).

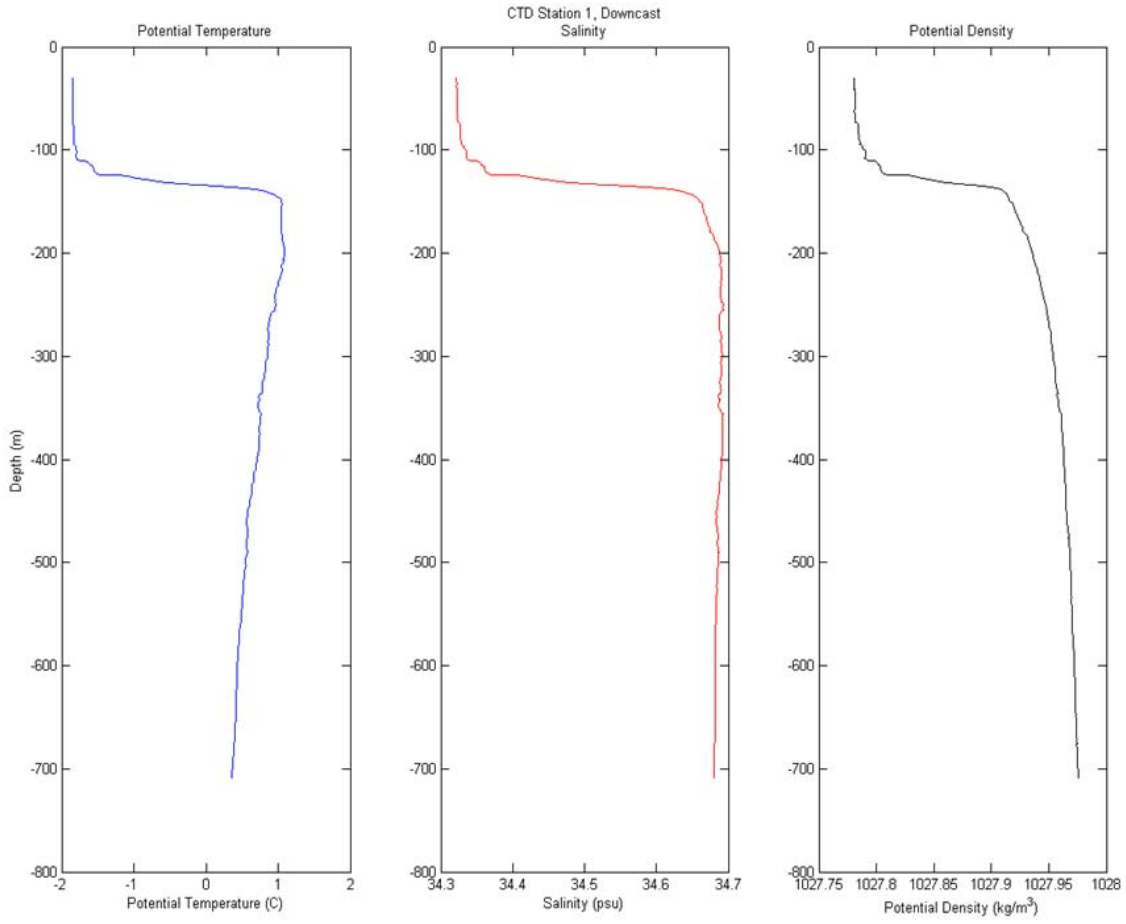

Figure 53. Initial potential temperature, salinity, and potential density profiles for CTD station 1 downcast.

2. CTD Station 65

CTD station 65 was chosen due to the location over the Maud Rise in the Taylor column. This water column exhibited marginal stability with a potential density jump of

0.08 kg/m^3 (illustrated in Figure 54). The potential temperature and salinity differences are also smaller than at station 1 (approximately 2 ^{o}C and 0.2 psu respectively).

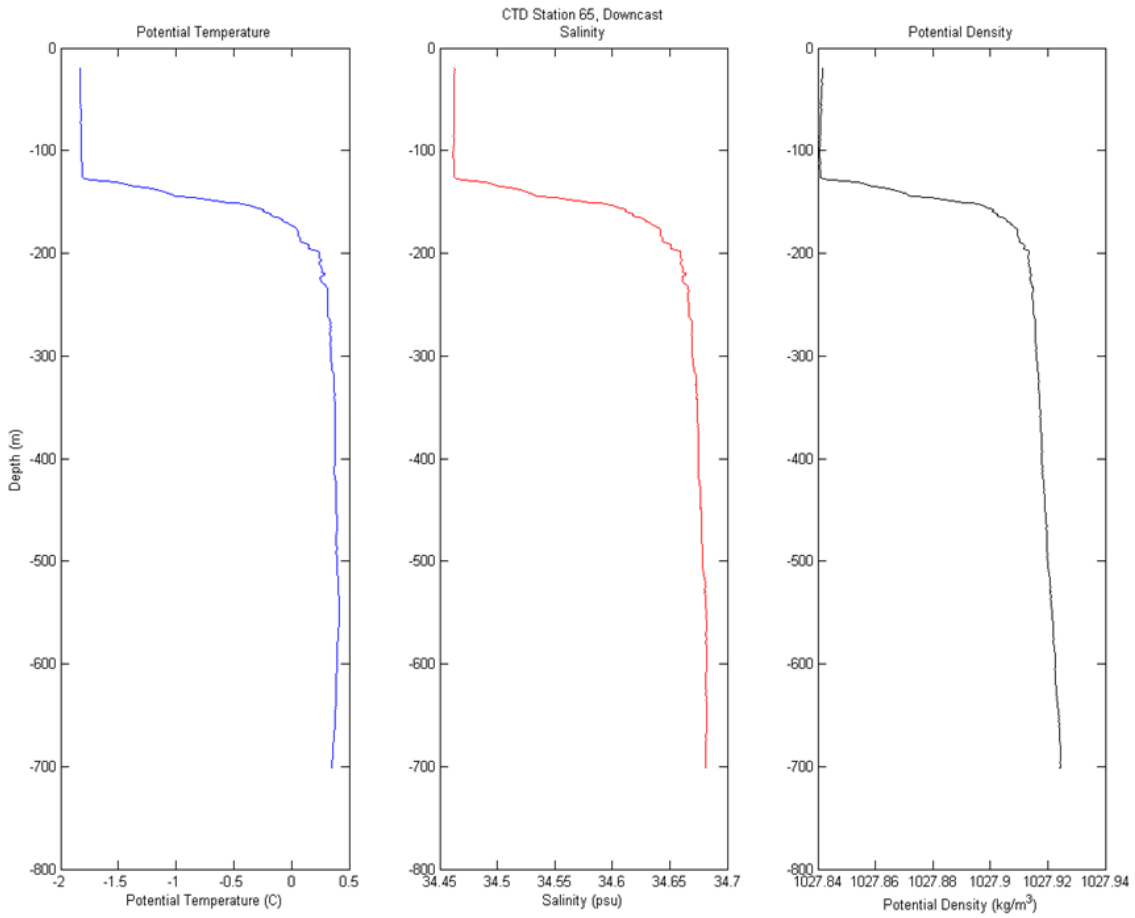

Figure 54. Initial potential temperature, salinity, and potential density profiles for CTD station 65 downcast.

3. CTD Station 92

CTD station 92 was located to the southwest of the Maud Rise in an area that Muench et al. (2001) called the warm pool. They further define this area as a "dynamically necessary region of positive (cyclonic) vorticity that is associated with a Taylor column over the rise". It was the least stable of the three locations chosen for this study. The potential density difference (Figure 55) at this location was approximately 0.05 kg/m^3. The potential temperature difference was approximately 2.3 ^{o}C (slightly higher than at station 65 but expected in the warm pool), and the salinity difference was approximately 0.18 psu.

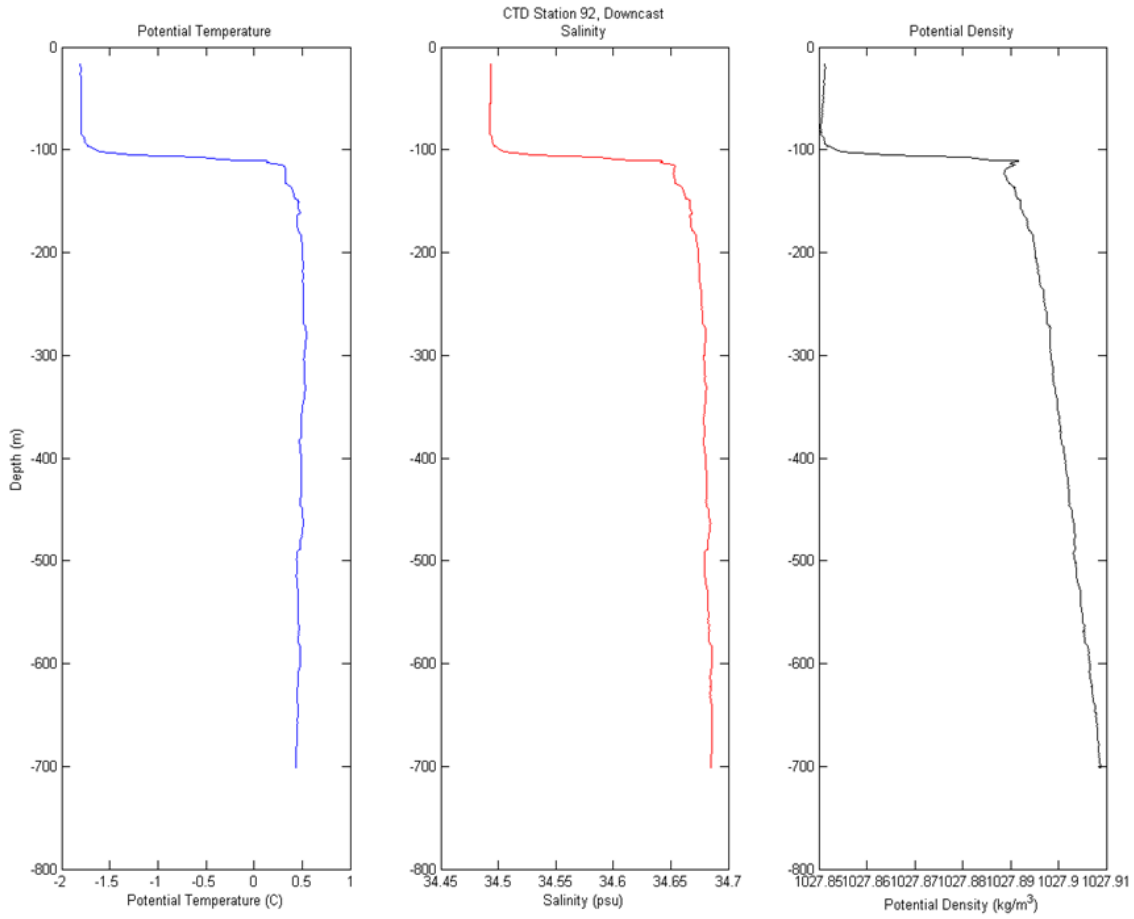

Figure 55. Initial potential temperature, salinity, and potential density profiles for CTD station 92 downcast.

D. COMPARISON OF OCEAN MODEL RESULTS FORCED BY AMPS AND OBSERVATIONAL DATA

1. CTD Station 1

Figure 56 shows friction speed for the four different scenarios run. With the exception of day four, observed forcing was shown to result in a slightly higher friction speed than AMPS forcing. This result carried over to the friction speeds when both AMPS and observed wind speeds were increased.

Figure 57 shows temperature fluxes for all four scenarios. Both cases of increased wind speed (Figure 57 c. and d.) indicate relatively strong and deep positive temperature flux when compared to AMPS forecast and observed values (Figure 57 a.

and b.). For AMPS forecast and observation inputs, a relatively large negative salinity flux persisted over the entire period (Figure 58 a. and b.). For increased wind speed scenarios, a large positive salinity flux was initially present with small intrusions of negative salinity flux later in the period (Figure 58 c. and d.). Buoyancy flux (Figure 59) was found to closely follow salinity flux.

For the AMPS forecast and observation input, the weaker temperature flux allowed the sea ice to grow, which in turn caused negative salinity flux (increased salinity in the upper layer due to brine rejection of the freezing seawater). Figure 60 shows ocean model predicted ice thickness (initially 40 cm) increasing almost linearly after day one.

When forcing was increased, the ocean model predicted an ice thickness decrease (Figure 61), with small increases in thickness around day three and days six and seven (corresponding to negative buoyancy and salinity fluxes at that time). The increased temperature flux for these runs immediately caused the sea ice to melt, thereby mixing fresh water with the upper layer water and creating positive salinity and buoyancy fluxes in the upper layer.

Potential temperature, salinity, and potential density profiles are shown in Figures 62, 63, and 64 respectively. Shown are initial CTD profiles (blue), and ocean model prediction at the conclusion of the run (with AMPS input (black), observed input (red), AMPS wind speed increased by factor of two (green), and observed wind speed increased by factor of two (cyan)). These profiles agree with results obtained from contour and ice thickness plots discussed above.

For CTD station 1, the ocean model forced by observed conditions led to the least stable profile after seven days. Under this scenario, potential density difference across the pycnocline decreased to approximately 0.10 kg/m^3, compared to an initial value of 0.175kg/m^3.

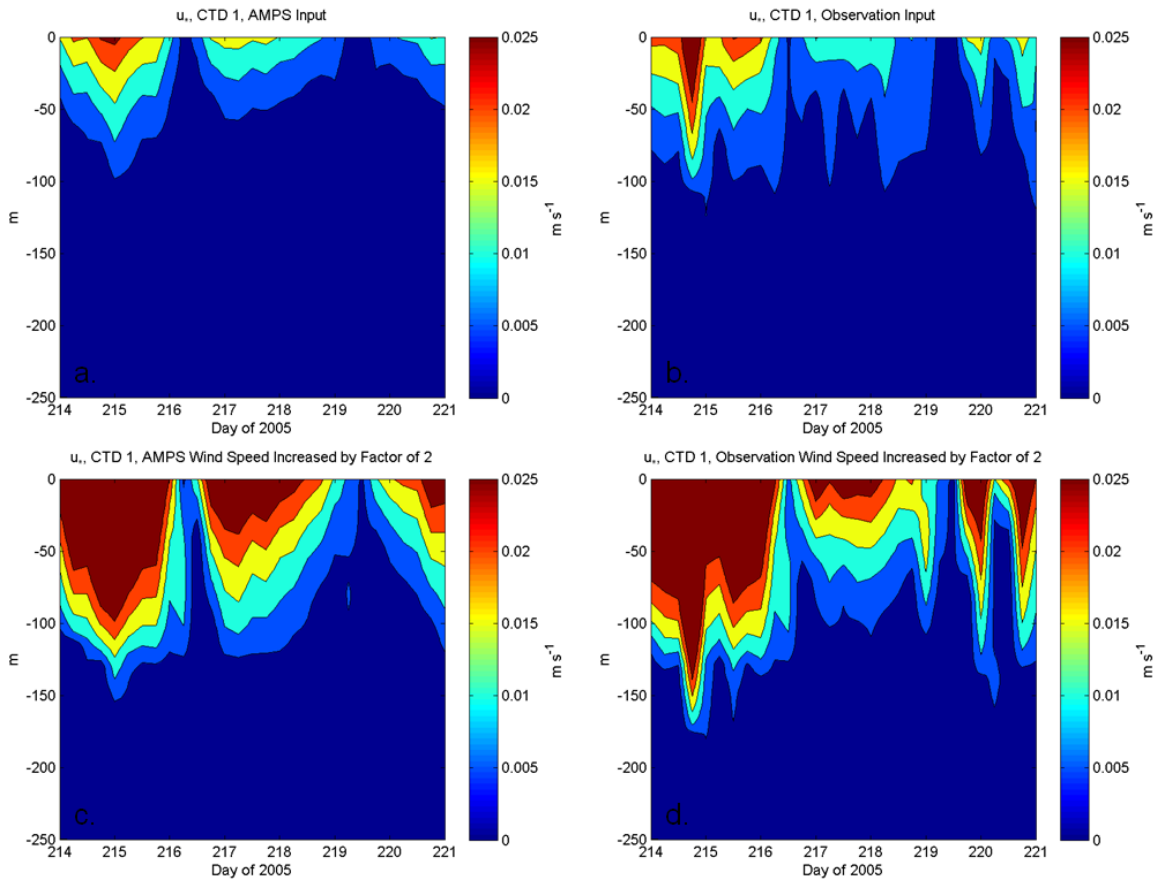

Figure 56. Friction speed (u_*) contour plots from surface to 250 meters at CTD station 1 for Julian days 214 to 221: a.) AMPS forecast, b.) Observed conditions, c.) AMPS forecast wind speed increased by factor of two, and d.) Observed wind speed increased by factor of two.

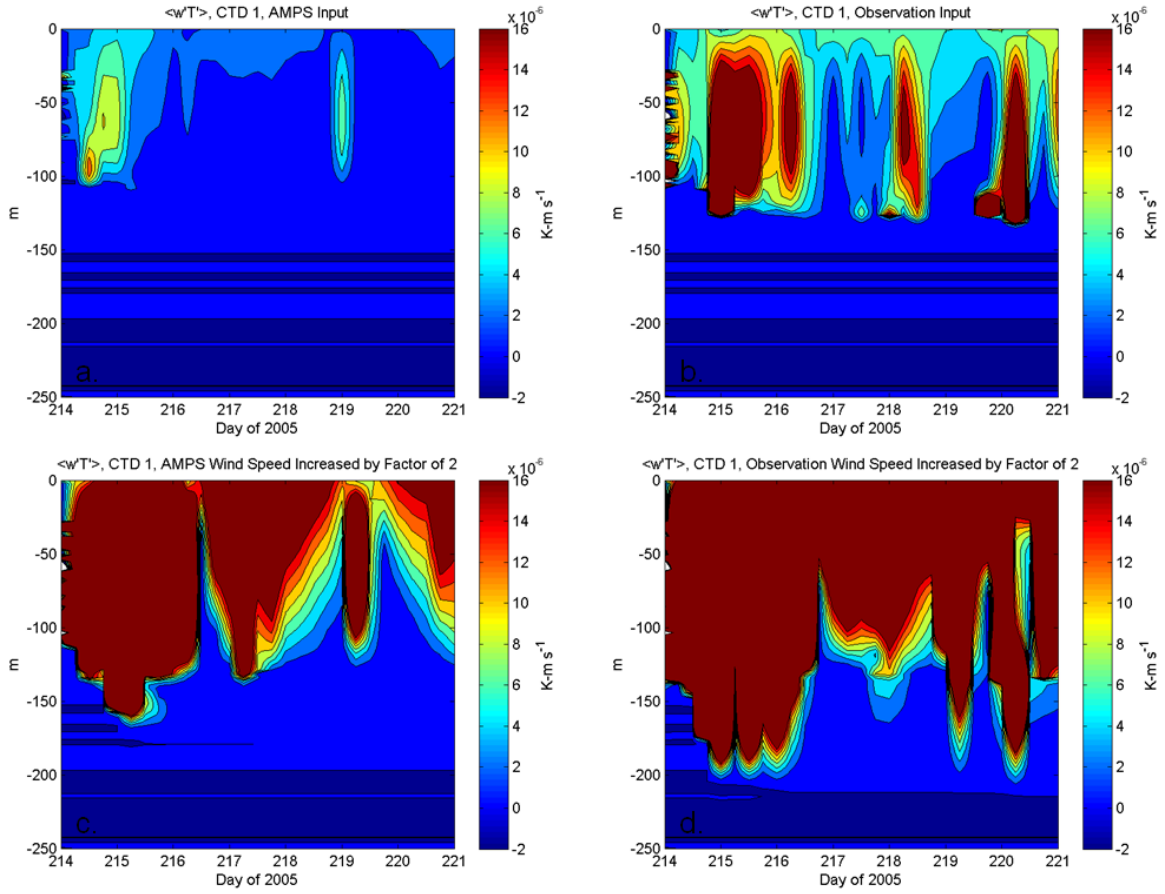

Figure 57. Temperature flux (<w'T'>) contour plots from surface to 250 meters at CTD station 1 for Julian days 214 to 221: a.) AMPS forecast, b.) Observed conditions, c.) AMPS forecast wind speed increased by factor of two, and d.) Observed wind speed increased by factor of two.

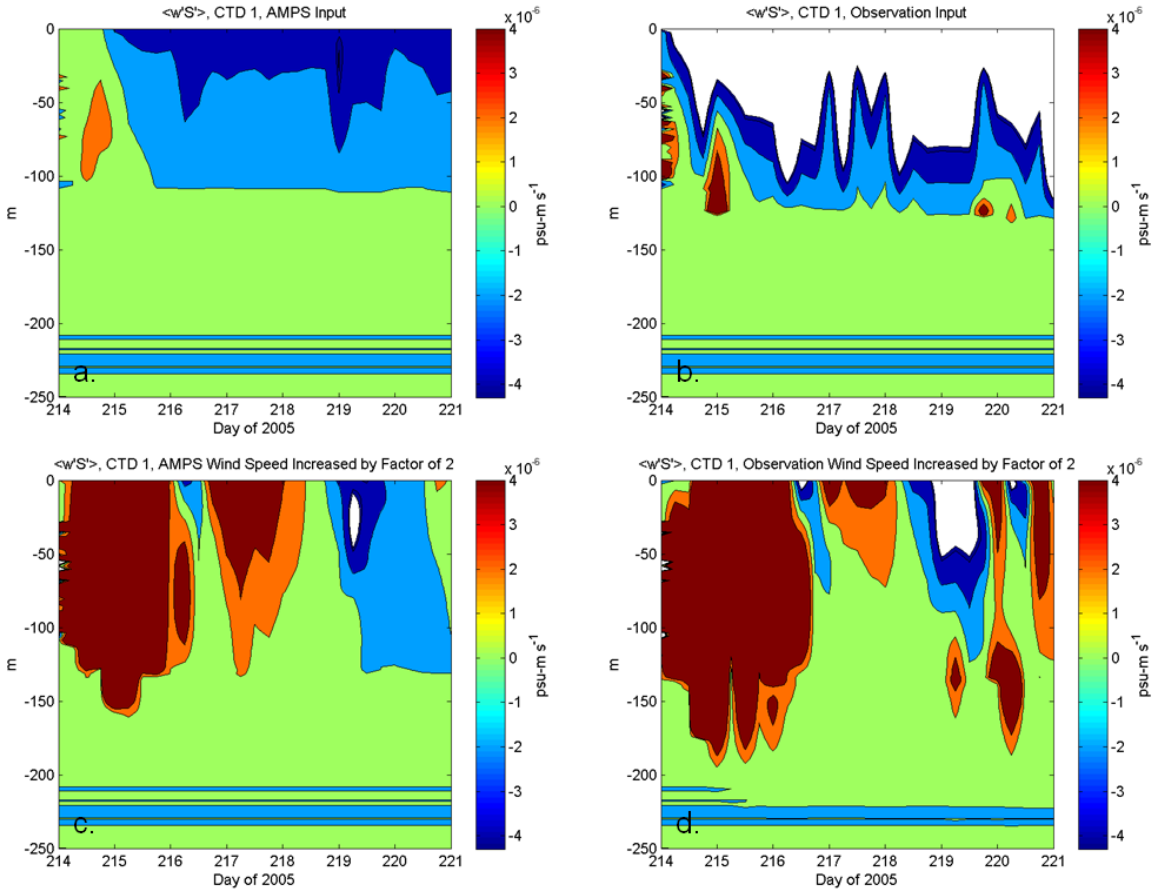

Figure 58. Salinity flux (<w'S'>) contour plots from surface to 250 meters at CTD station 1 for Julian days 214 to 221: a.) AMPS forecast, b.) Observed conditions, c.) AMPS forecast wind speed increased by factor of two, and d.) Observed wind speed increased by factor of two (Note white shaded contours are areas of relatively large negative values).

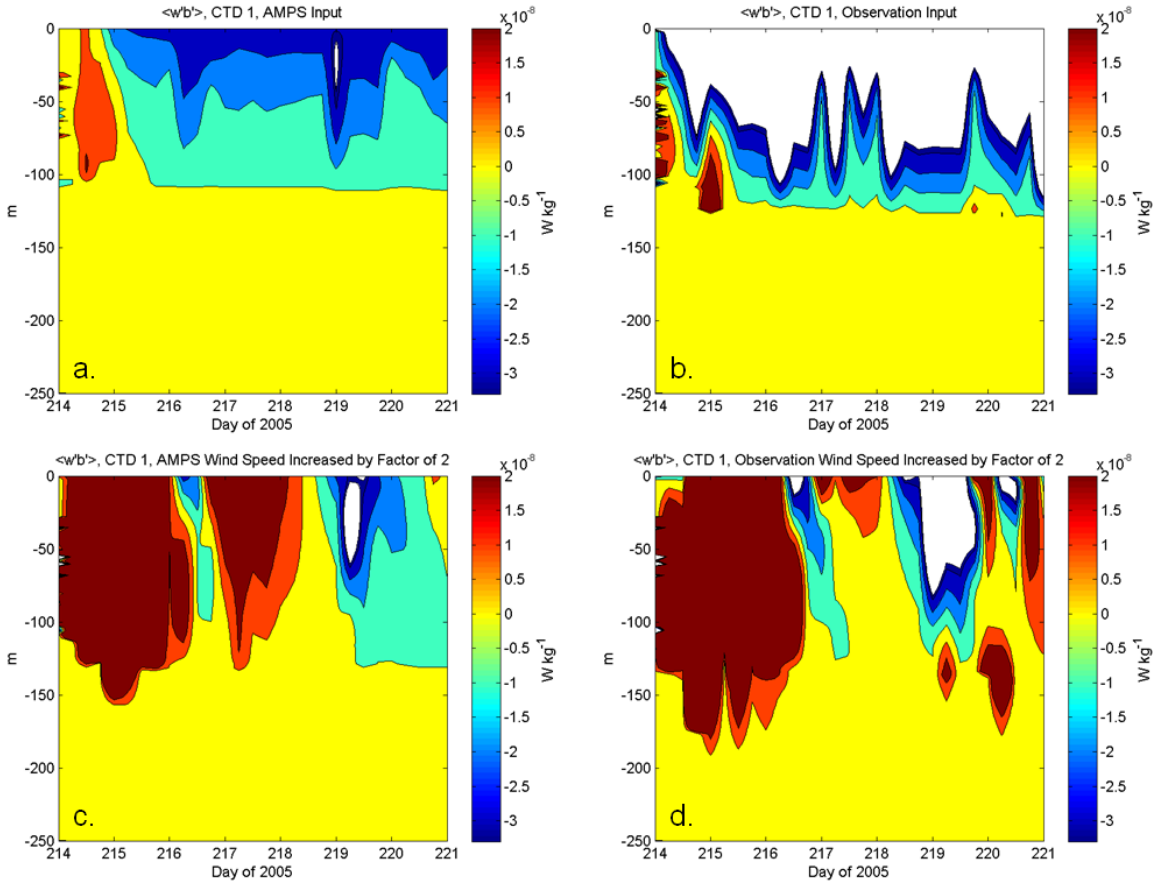

Figure 59. Buoyancy flux (<w'b'>) contour plots from surface to 250 meters at CTD station 1 for Julian days 214 to 221: a.) AMPS forecast, b.) Observed conditions, c.) AMPS forecast wind speed increased by factor of two, and d.) Observed wind speed increased by factor of two (Note white shaded contours are areas of relatively large negative values).

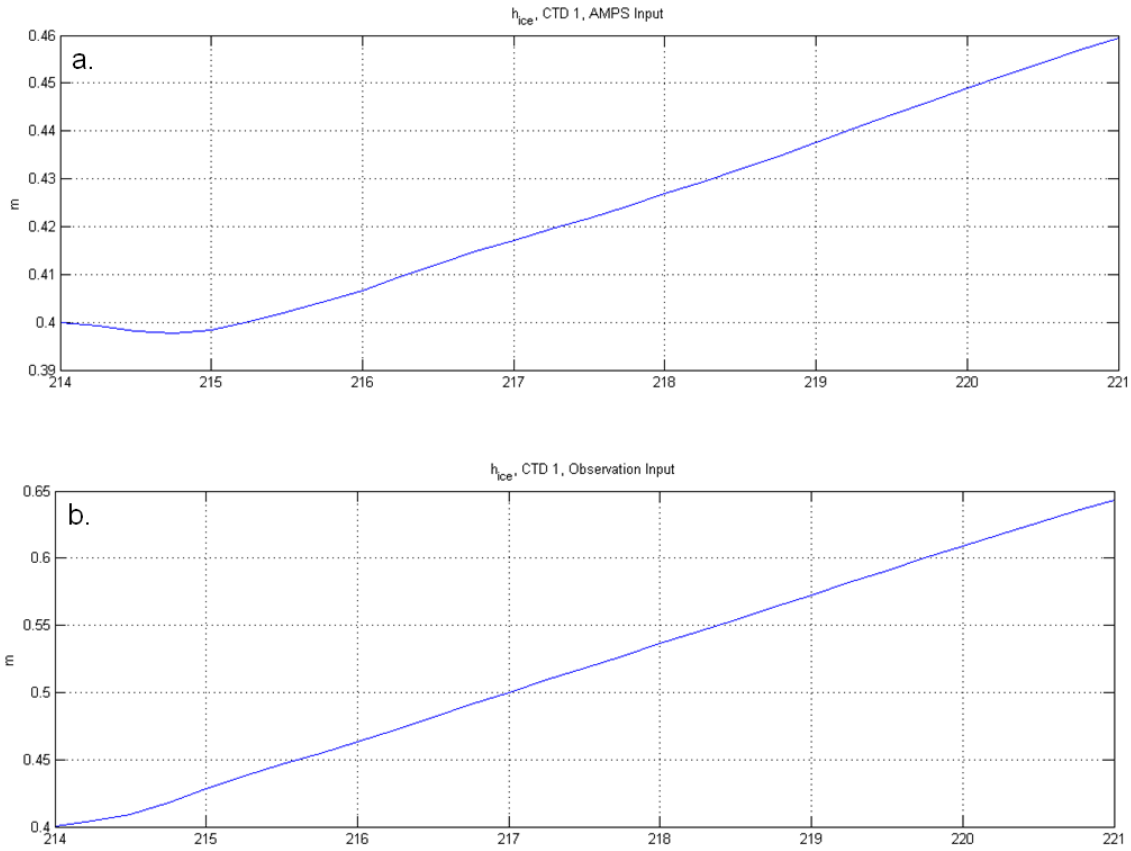

Figure 60. Ocean model predicted ice thickness at CTD station 1, Julian days 214 to 221, for a.) AMPS forecast, and b.) Observed wind forcing conditions.

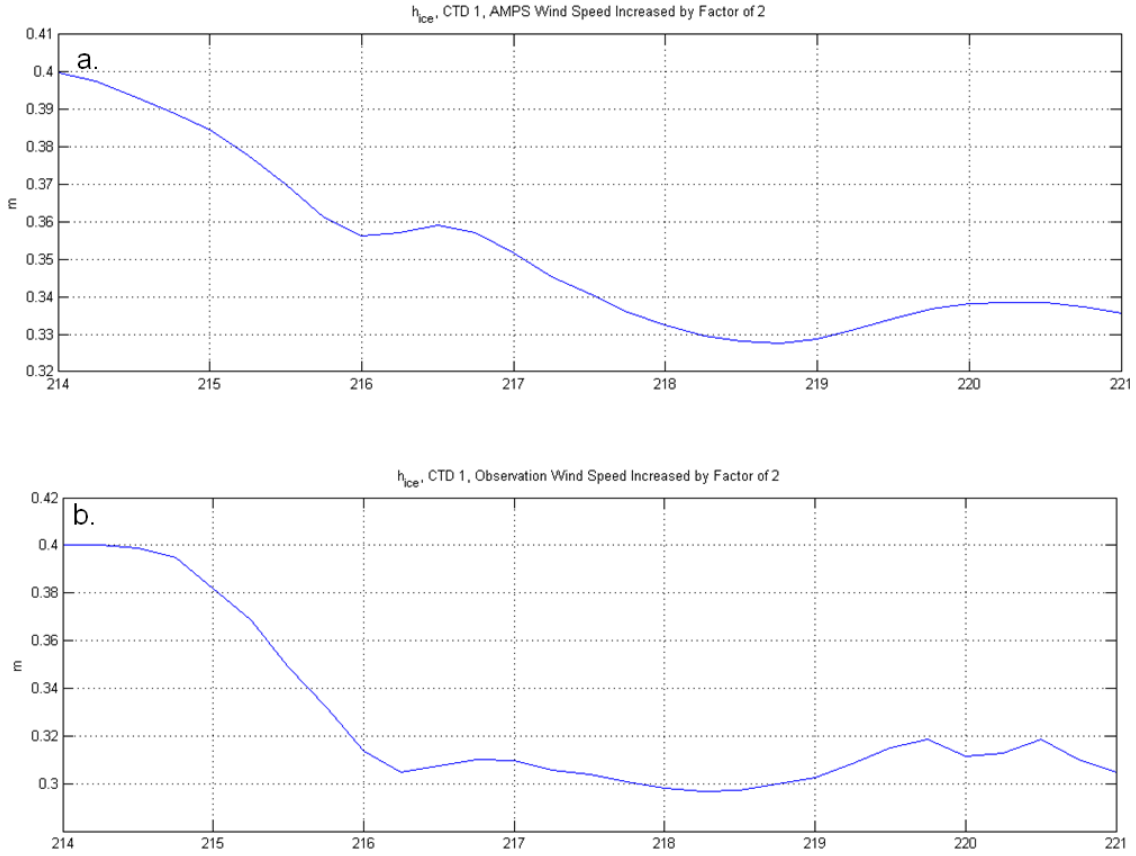

Figure 61. Ocean model predicted ice thickness at CTD station 1, Julian days 214 to 221, for a.) AMPS forecast wind speed increased by factor of two, and b.) Observed wind speed increased by factor of two.

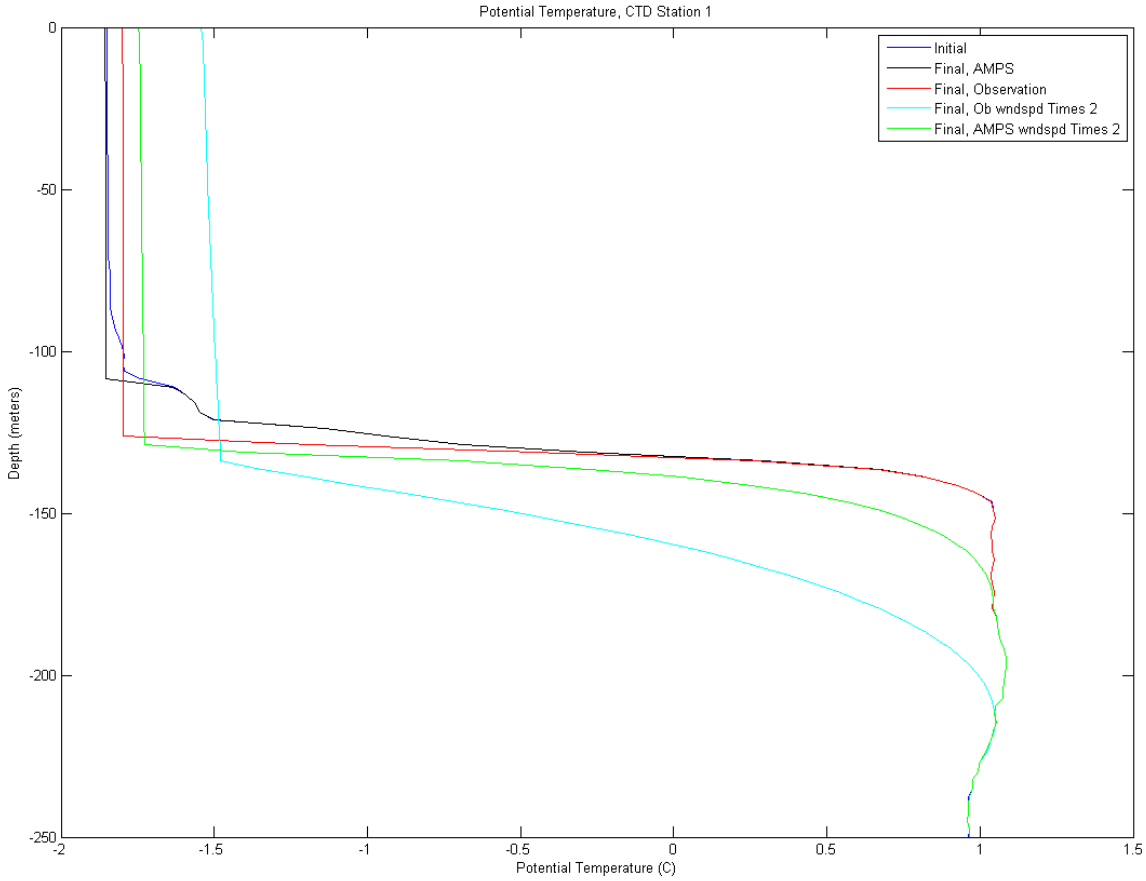

Figure 62. Potential temperature profiles for CTD station 1. Profiles shown are CTD initial (blue), and ocean model prediction seven days later (with AMPS forcing (black), observed forcing (red), AMPS wind speed increased by factor of two (green), and observed wind speed increased by factor of two (cyan)).

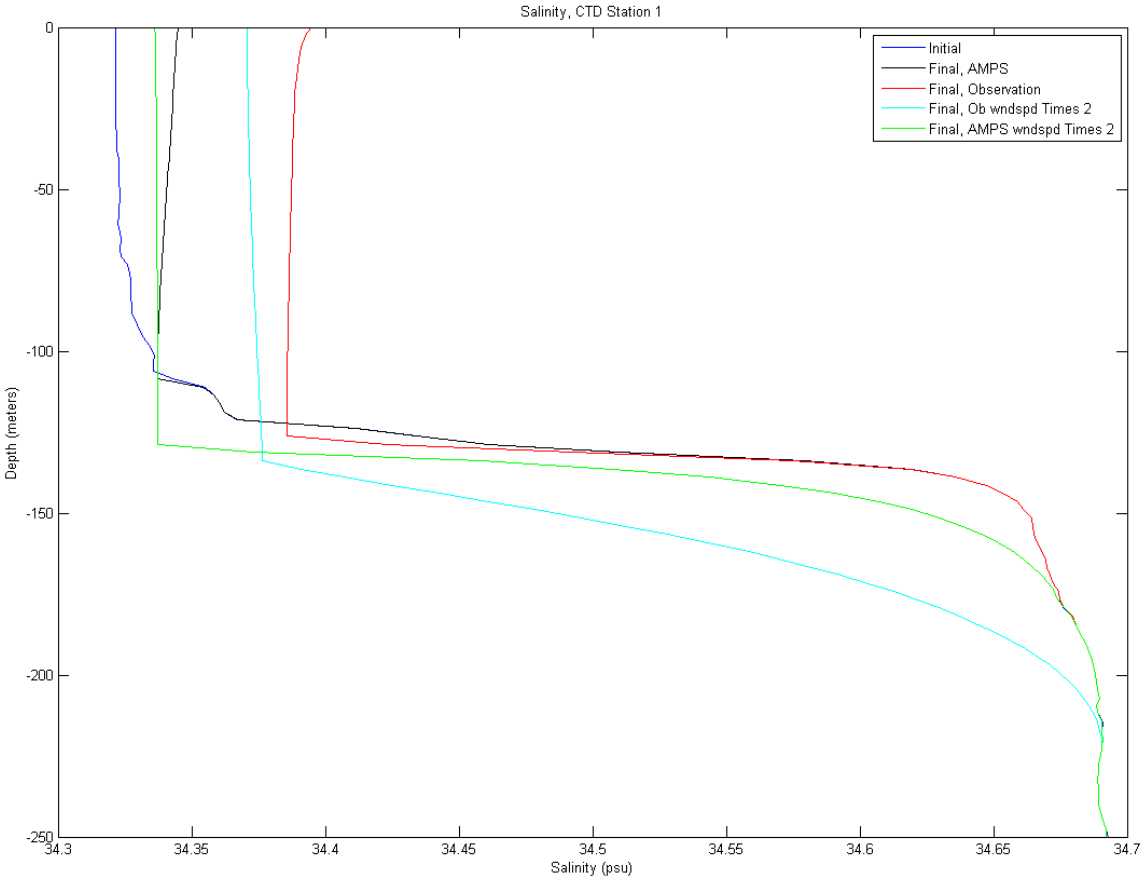

Figure 63. Salinity profiles for CTD station 1. Profiles shown are CTD initial (blue), and ocean model prediction seven days later (with AMPS forcing (black), observed forcing (red), AMPS wind speed increased by factor of two (green), and observed wind speed increased by factor of two (cyan)).

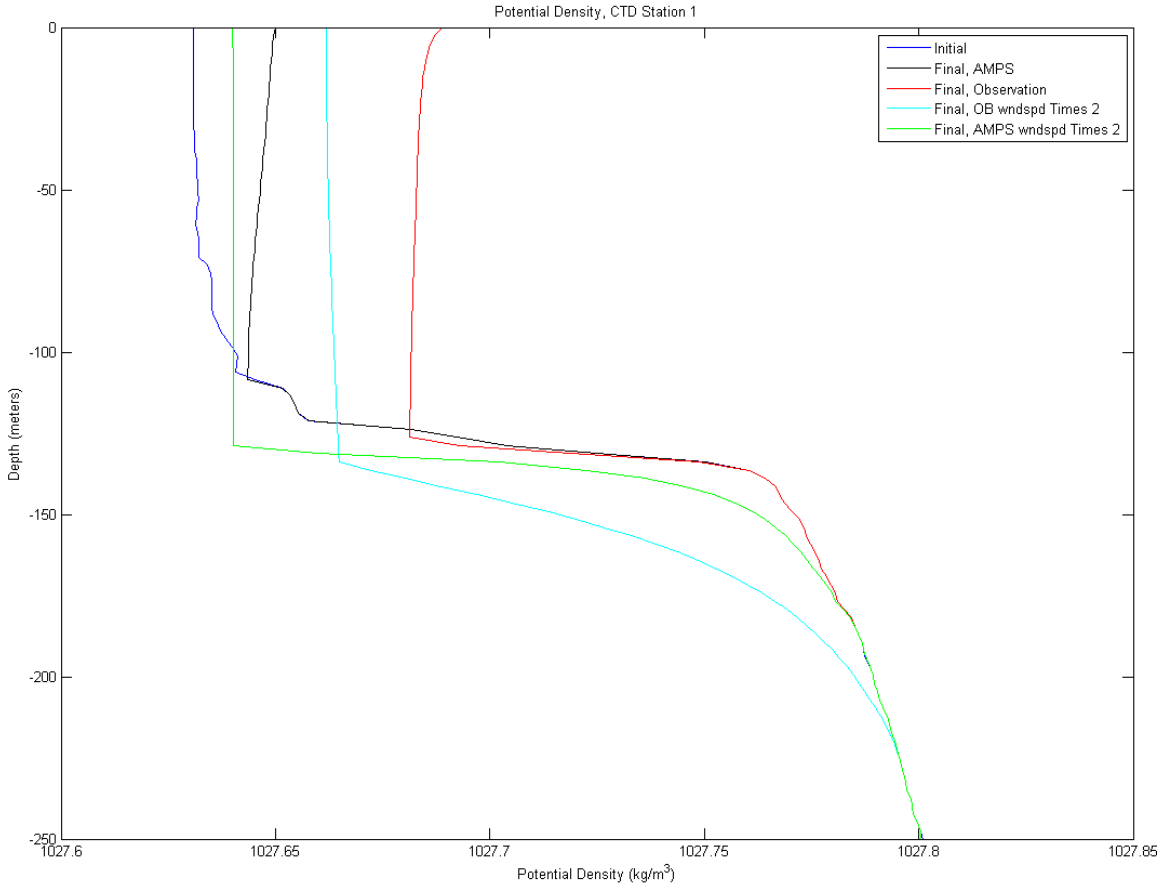

Figure 64. Potential density profiles for CTD station 1. Profiles shown are CTD initial (blue), and ocean model prediction seven days later (with AMPS forcing (black), observed forcing (red), AMPS wind speed increased by factor of two (green), and observed wind speed increased by factor of two (cyan)).

2. CTD Station 65

Figure 65 shows friction speed for the four different scenarios run at CTD station 65 (Taylor column over the Maud Rise). Friction speed values between AMPS forecast and observed conditions (Figure 65 a. and b.) were very similar (observed conditions slightly larger). Again, when AMPS and observed forcing were increased (Figure 65 c. and d.), friction speed increased and high values extended deeper into the water column.

Relatively large positive temperature flux (note the temperature flux contour values are close to two orders of magnitude larger than CTD station 1) for the AMPS forecast scenario (Figure 66 a.) occurred late in the model run (end of days five and seven). For observed conditions (Figure 66 b.), positive temperature fluxes occur

between days two and three, three and four, five and six, and six and seven. For each of the increased forcing scenarios (Figure 66 c. and d.), a large positive temperature flux area appeared between days two and three.

Salinity and buoyancy fluxes (Figures 67 and 68 respectively) tended to be negative the entire period for all scenarios. A notable exception to this is the large area of positive salinity and buoyancy fluxes (Figures 67 c. and d. and 68 c. and d.) from approximately 75 to 150 meters between days two and three for the increased forcing scenarios (this area of positive salinity and buoyancy fluxes corresponds to the large positive temperature flux discussed in the previous paragraph).

Figures 69 and 70 show an almost linear increase in ocean model predicted ice thickness for all four scenarios (note in Figure 70 a. and b., the rate of ice growth decreases around day three in agreement with temperature, salinity, and buoyancy flux).

Potential temperature, salinity, and potential density profiles are shown in Figures 71, 72 and 73, respectively. Initial CTD profiles and ocean model prediction at the conclusion of the run are as described for CTD station 1. As with CTD station 1, profiles agree well with contour and ocean model predicted ice thickness plots.

At CTD station 65, the increased observed forcing scenario resulted in the least stable water column at the end of the seven day model run. Potential density difference across the pycnocline (Figure 73) decreased from an initial value of 0.08 kg/m^3 to approximately 0.02 kg/m^3.

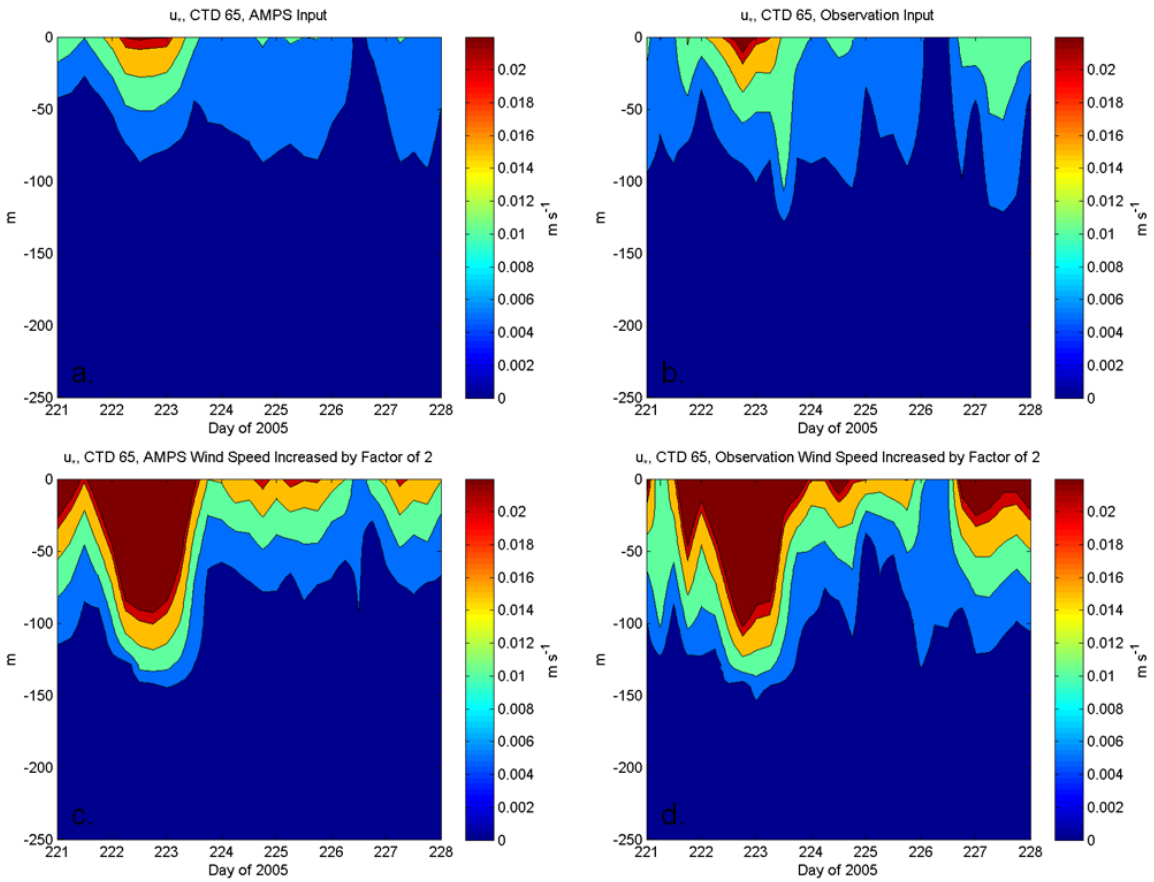

Figure 65. Friction speed (u_*) contour plots from surface to 250 meters at CTD station 65 for Julian days 221 to 228: a.) AMPS forecast, b.) Observed conditions, c.) AMPS forecast wind speed increased by factor of two, and d.) Observed wind speed increased by factor of two.

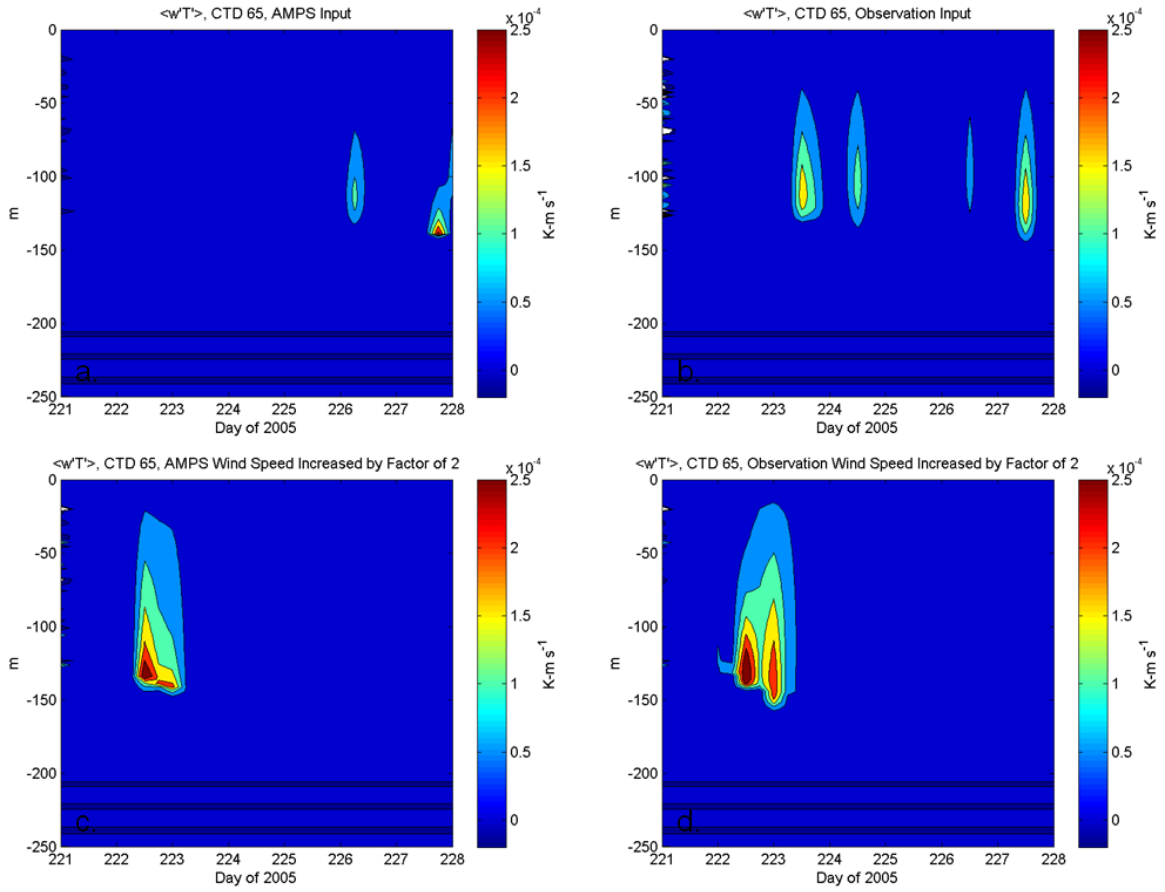

Figure 66. Temperature flux (<w'T'>) contour plots from surface to 250 meters at CTD station 65 for Julian days 221 to 228: a.) AMPS forecast, b.) Observed conditions, c.) AMPS forecast wind speed increased by factor of two, and d.) Observed wind speed increased by factor of two.

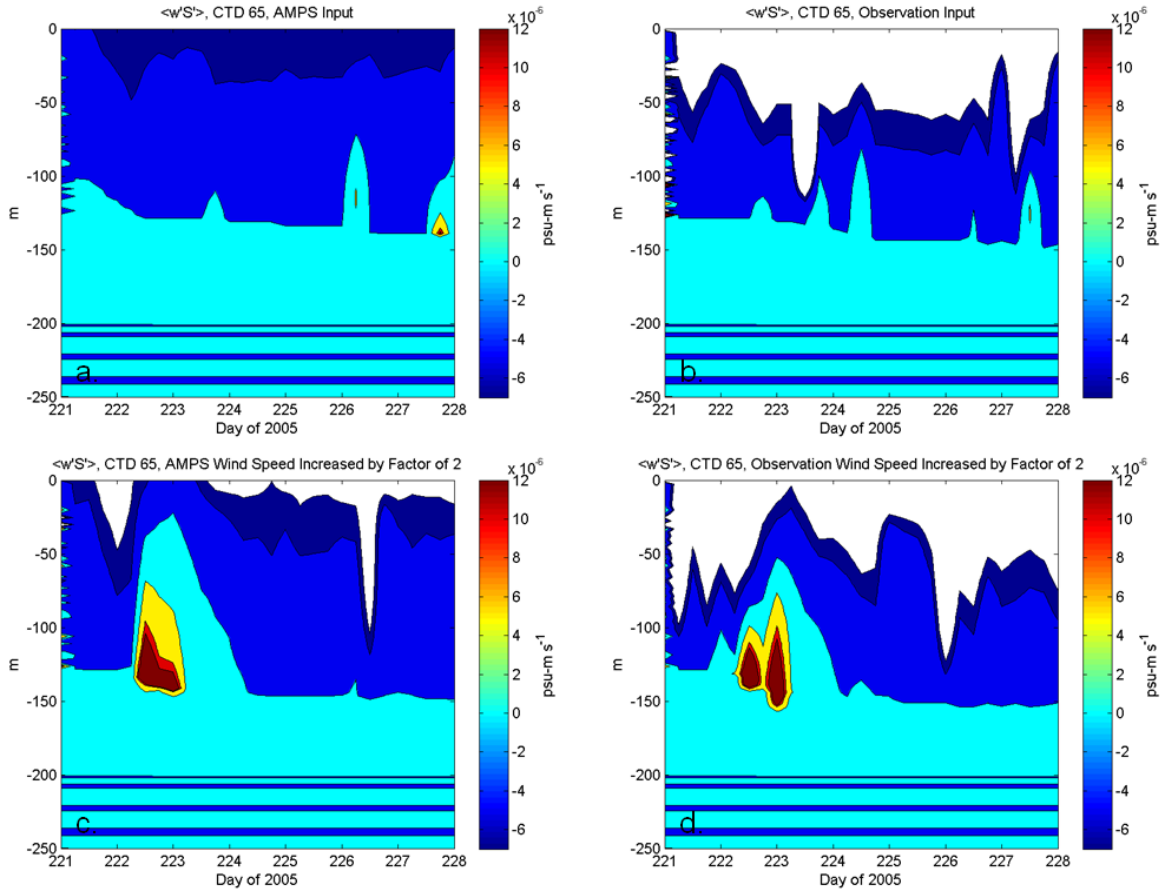

Figure 67. Salinity flux (<w'S'>) contour plots from surface to 250 meters at CTD station 65 for Julian days 221 to 228: a.) AMPS forecast, b.) Observed conditions, c.) AMPS forecast wind speed increased by factor of two, and d.) Observed wind speed increased by factor of two (Note white shaded contours are areas of relatively large negative values).

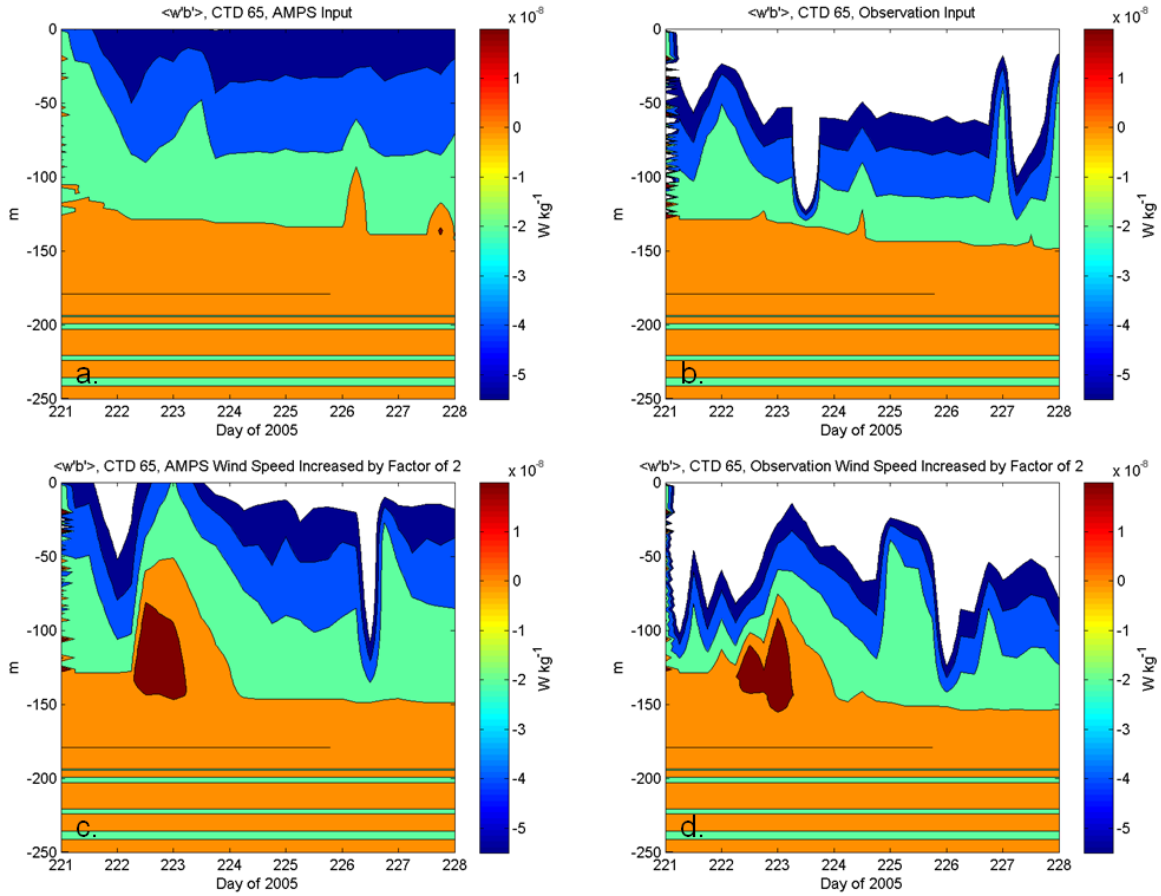

Figure 68. Buoyancy flux (<w'b'>) contour plots from surface to 250 meters at CTD station 65 for Julian days 221 to 228: a.) AMPS forecast, b.) Observed conditions, c.) AMPS forecast wind speed increased by factor of two, and d.) Observed wind speed increased by factor of two (Note white shaded contours are areas of relatively large negative values).

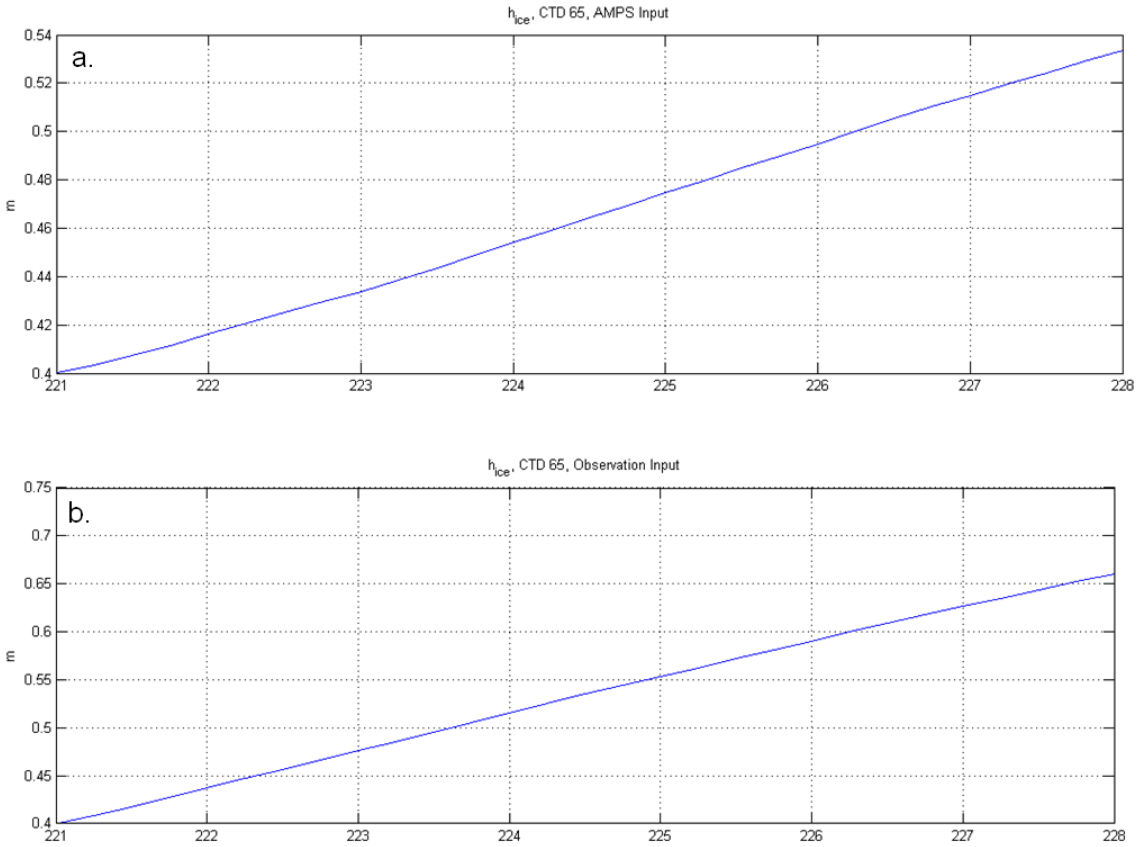

Figure 69. Ocean model predicted ice thickness at CTD station 65, Julian days 221 to 228, for a.) AMPS forecast, and b.) Observed wind forcing conditions.

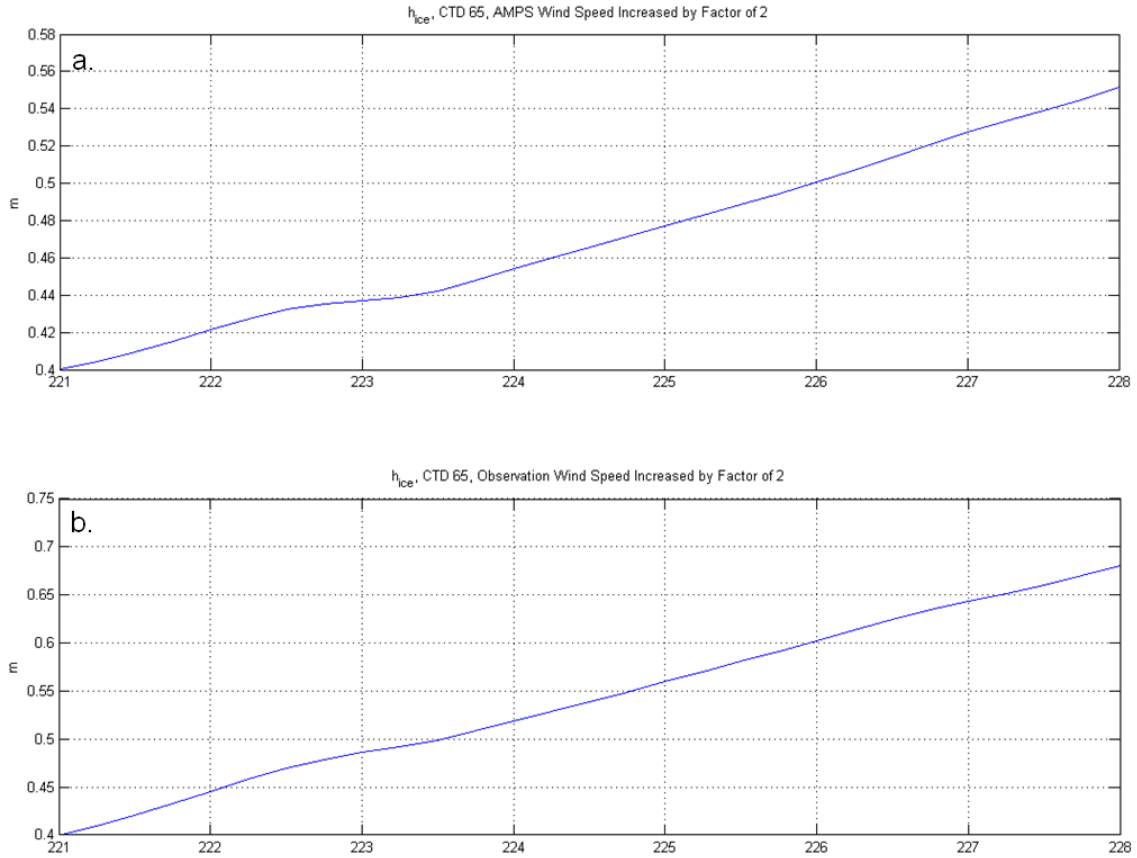

Figure 70. Ocean model predicted ice thickness at CTD station 65, Julian days 221 to 228, for a.) AMPS forecast wind speed increased by factor of two, and b.) Observed wind speed increased by factor of two.

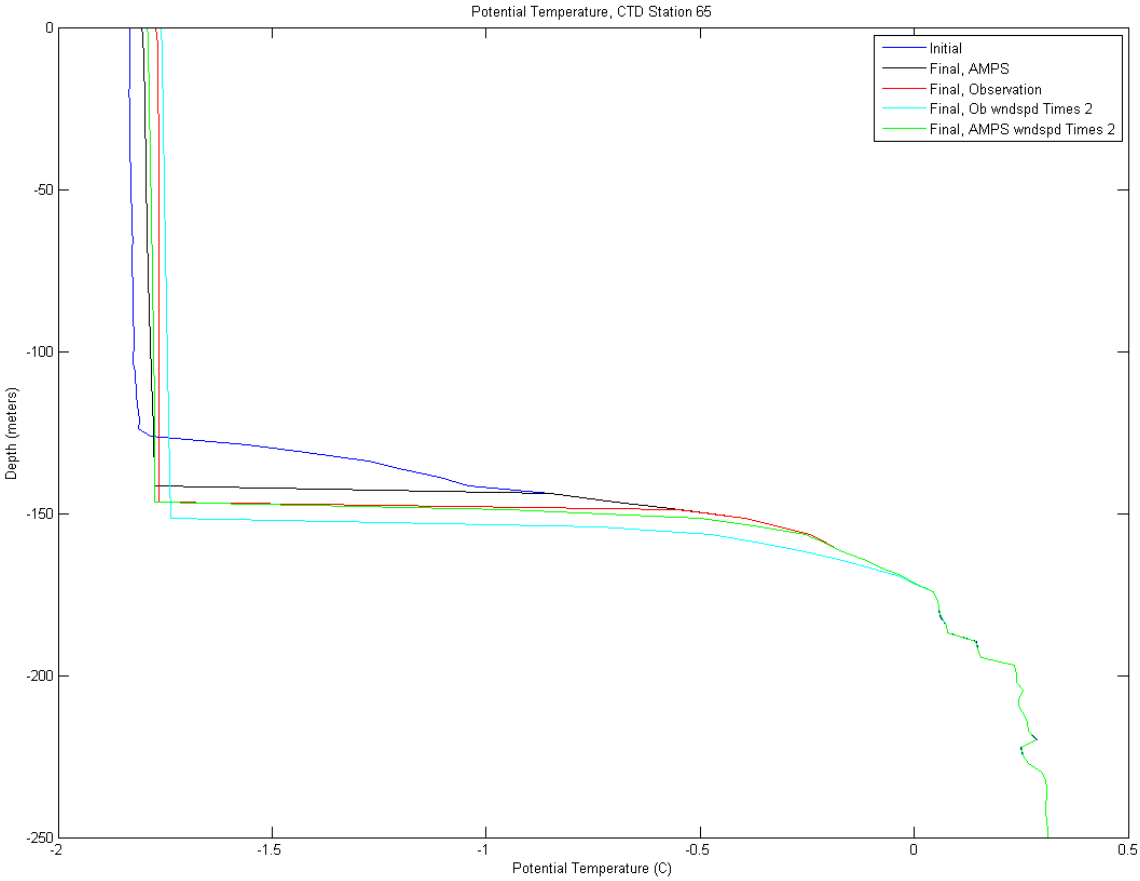

Figure 71. Potential temperature profiles for CTD station 65. Profiles shown are CTD initial (blue), and ocean model prediction seven days later (with AMPS forcing (black), observed forcing (red), AMPS wind speed increased by factor of two (green), and observed wind speed increased by factor of two (cyan)).

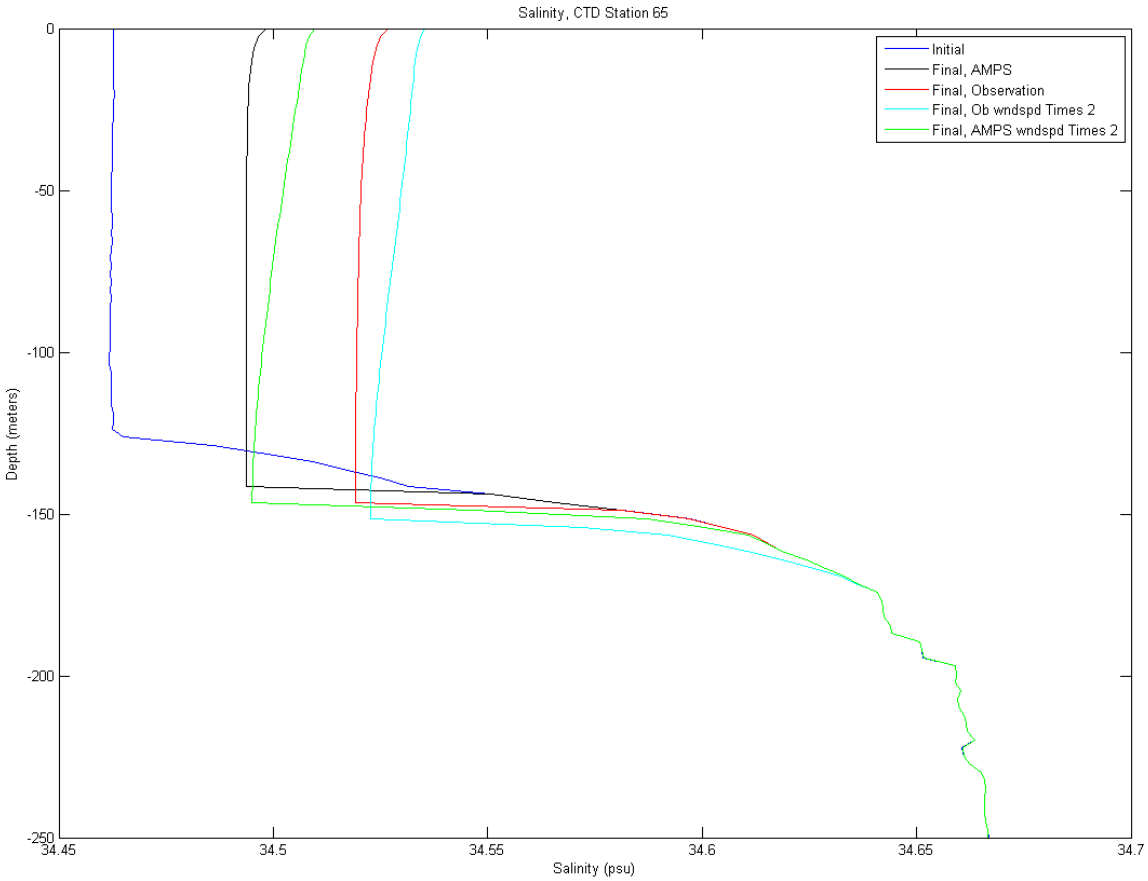

Figure 72. Salinity profiles for CTD station 65. Profiles shown are CTD initial (blue), and ocean model prediction seven days later (with AMPS forcing (black), observed forcing (red), AMPS wind speed increased by factor of two (green), and observed wind speed increased by factor of two (cyan)).

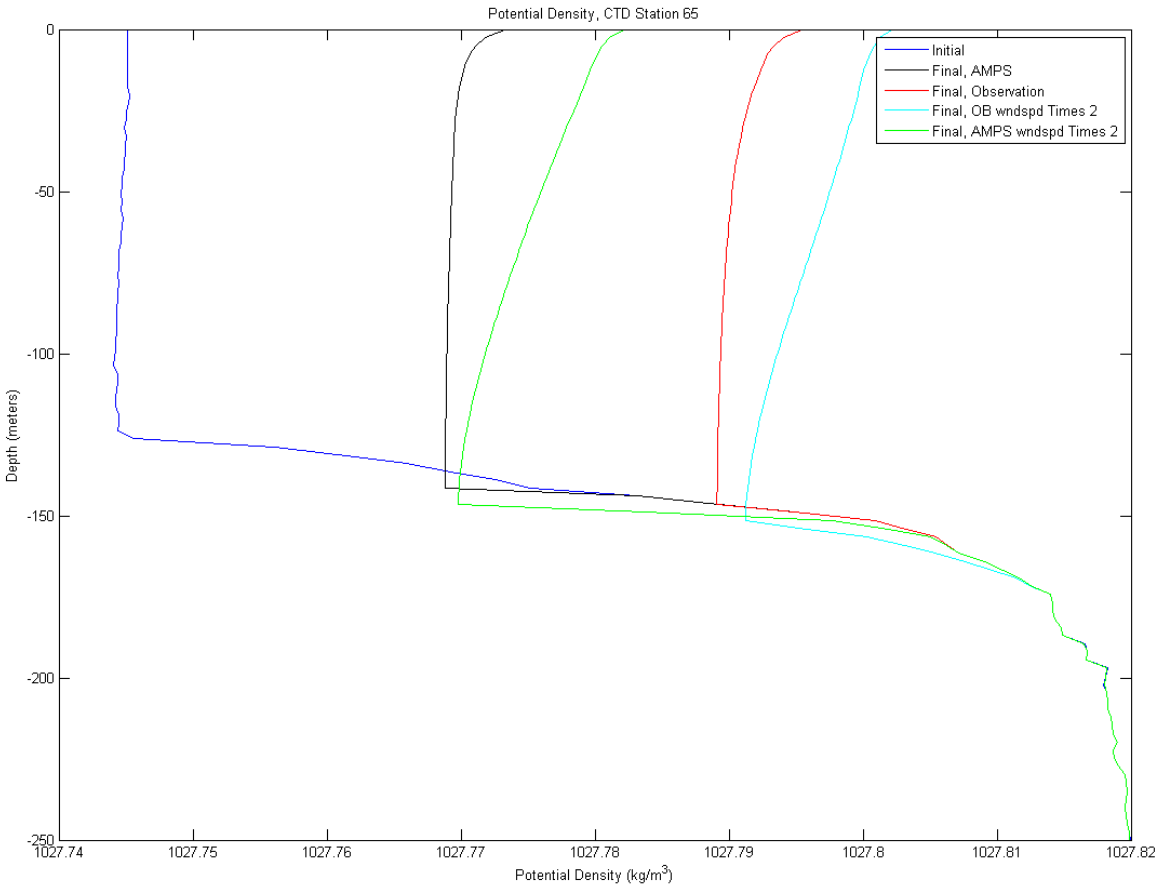

Figure 73. Potential density profiles for CTD station 65. Profiles shown are CTD initial (blue), and ocean model prediction seven days later (with AMPS forcing (black), observed forcing (red), AMPS wind speed increased by factor of two (green), and observed wind speed increased by factor of two (cyan)).

3. CTD Station 92

Figure 74 shows friction speed for the four different scenarios run at CTD station 92. Observed forcing resulted in a higher friction speed than AMPS forcing. This trend is also shown when both AMPS and observed wind speeds were increased.

A relatively large positive temperature flux area for the AMPS forecast scenario (Figure 75 a.) occurred at the end of day one into day two. For observed conditions (Figure 75 b.), large positive temperature flux areas occurred immediately on day one, between days three and four, and six and seven. For each of the increased forcing scenarios (Figure 75 c. and d.), the larger positive temperature flux areas occurred deeper in the water column, with very weak positive temperature flux near the surface.

For both AMPS scenarios (forecast and increased wind speed) the weaker forcing appeared to be unable to overcome the temperature flux. Figure 76 a. and c. show varying salinity flux (between positive and negative) throughout the water column. As before, buoyancy flux (Figure 77 a. and c.) followed salinity flux. The ocean model predicted ice thickness (Figures 78 a. and 79 a.) showed very little change for both of these scenarios.

Stronger forcing associated with both observed scenarios led to negative salinity and buoyancy fluxes (Figures 76 b. and d., and 77 b. and d.) in the upper water column over the entire period. The ocean model predicted ice thickness for both of these cases (Figures 78 b. and 79 b.) show an almost linear increase in ice thickness.

Potential temperature, salinity, and potential density profiles for are shown in Figures 80, 81, and 82 respectively. Initial CTD profiles and ocean model prediction at the conclusion of the run are as described for CTD station 1. As with CTD station 1, profiles agree well with contour and ice thickness plots.

At CTD station 92, the observed forcing scenario resulted in the least stable water column at the end of the seven day model run. Potential density difference across the pycnocline (Figure 82) decreased from an initial value of 0.05 kg/m^3 to approximately 0.01 kg/m^3. Note that AMPS scenarios at this station caused very little change.

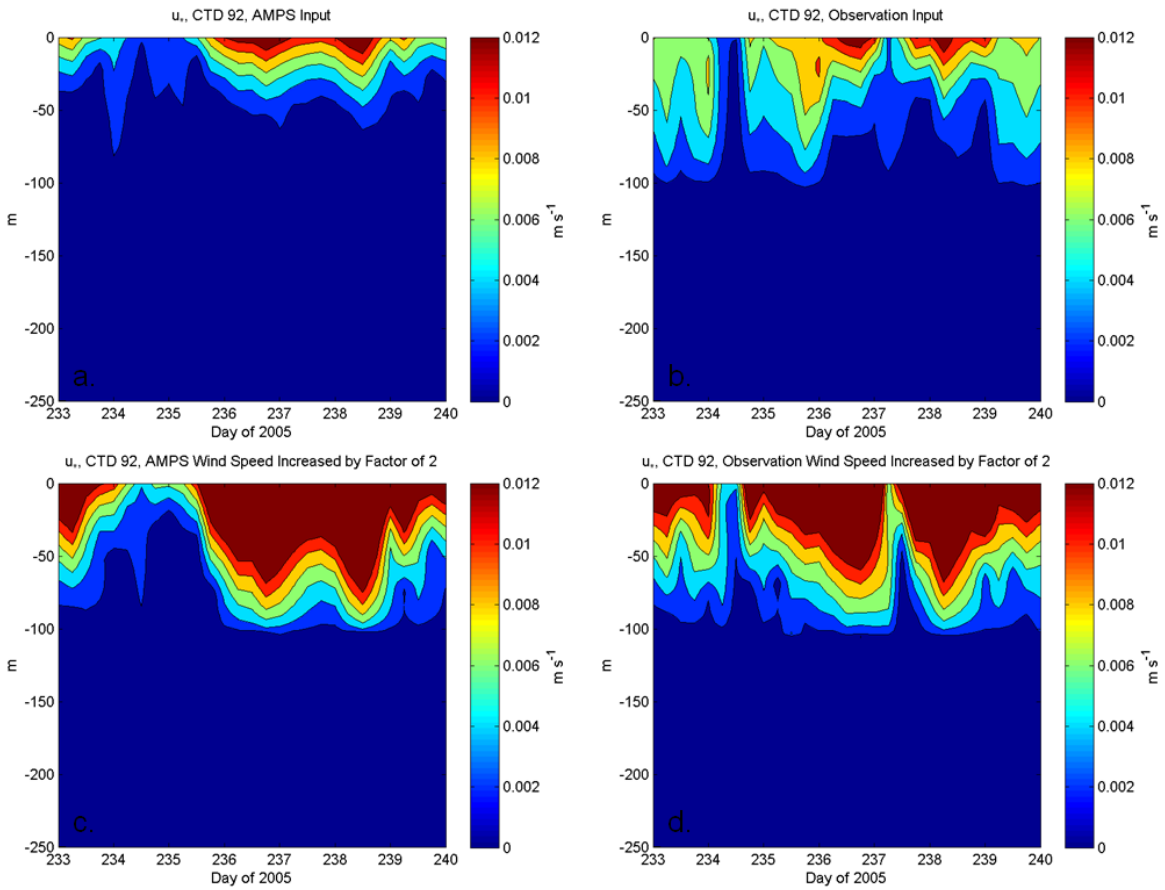

Figure 74. Friction speed (u_*) contour plots from surface to 250 meters at CTD station 92 for Julian days 233 to 240 a.) AMPS forecast, b.) Observed conditions, c.) AMPS forecast wind speed increased by factor of two, and d.) Observed wind speed increased by factor of two.

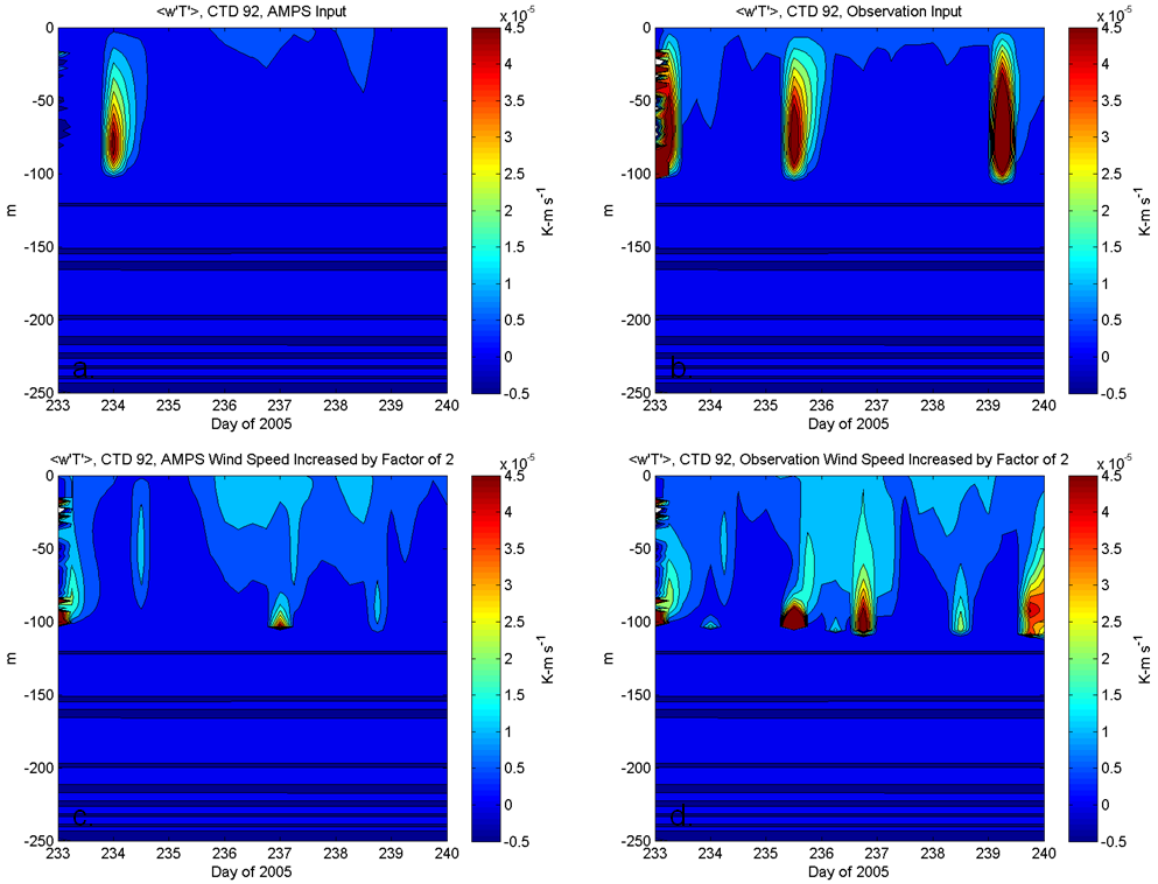

Figure 75. Temperature flux (<w'T'>) contour plots from surface to 250 meters at CTD station 92 for Julian days 233 to 240: a.) AMPS forecast, b.) Observed conditions, c.) AMPS forecast wind speed increased by factor of two, and d.) Observed wind speed increased by factor of two.

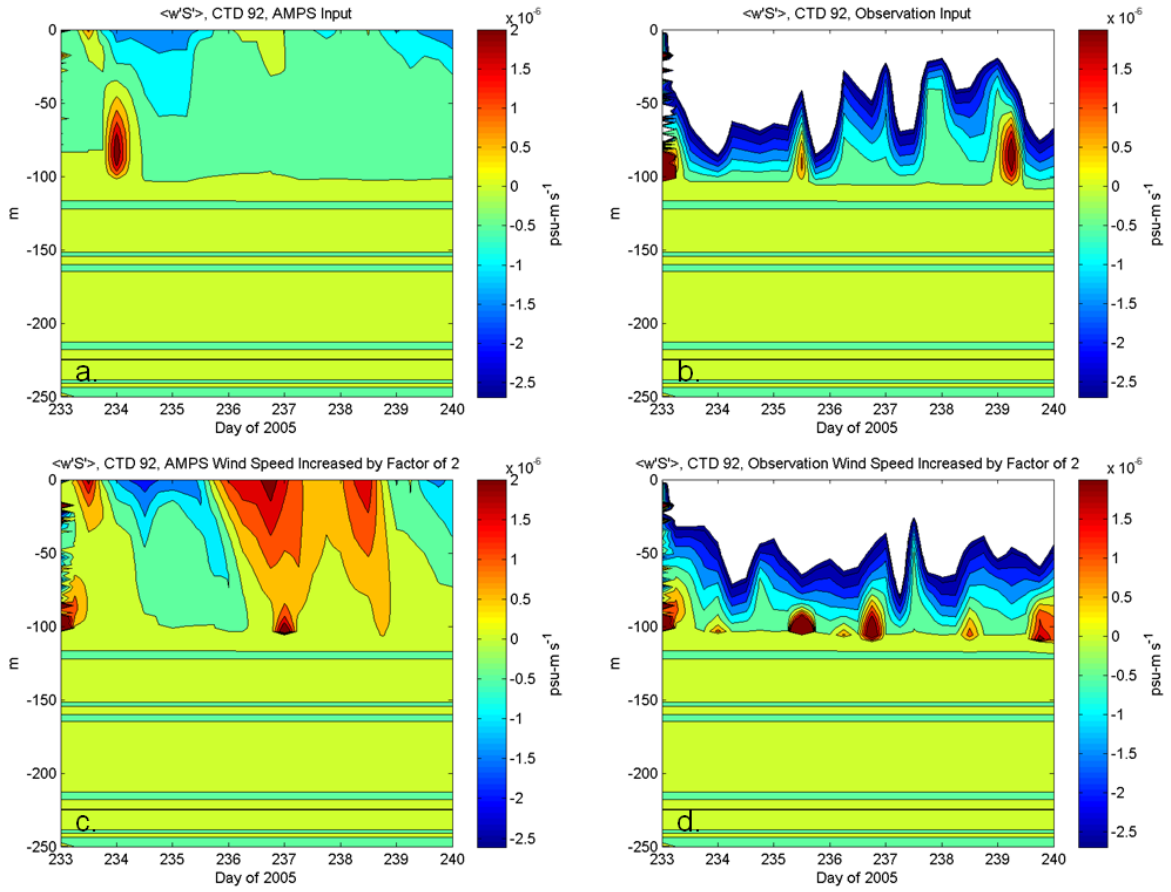

Figure 76. Salinity flux (<w'S'>) contour plots from surface to 250 meters at CTD station 92 for Julian days 233 to 240: a.) AMPS forecast, b.) Observed conditions, c.) AMPS forecast wind speed increased by factor of two, and d.) Observed wind speed increased by factor of two (Note white shaded contours are areas of relatively large negative values).

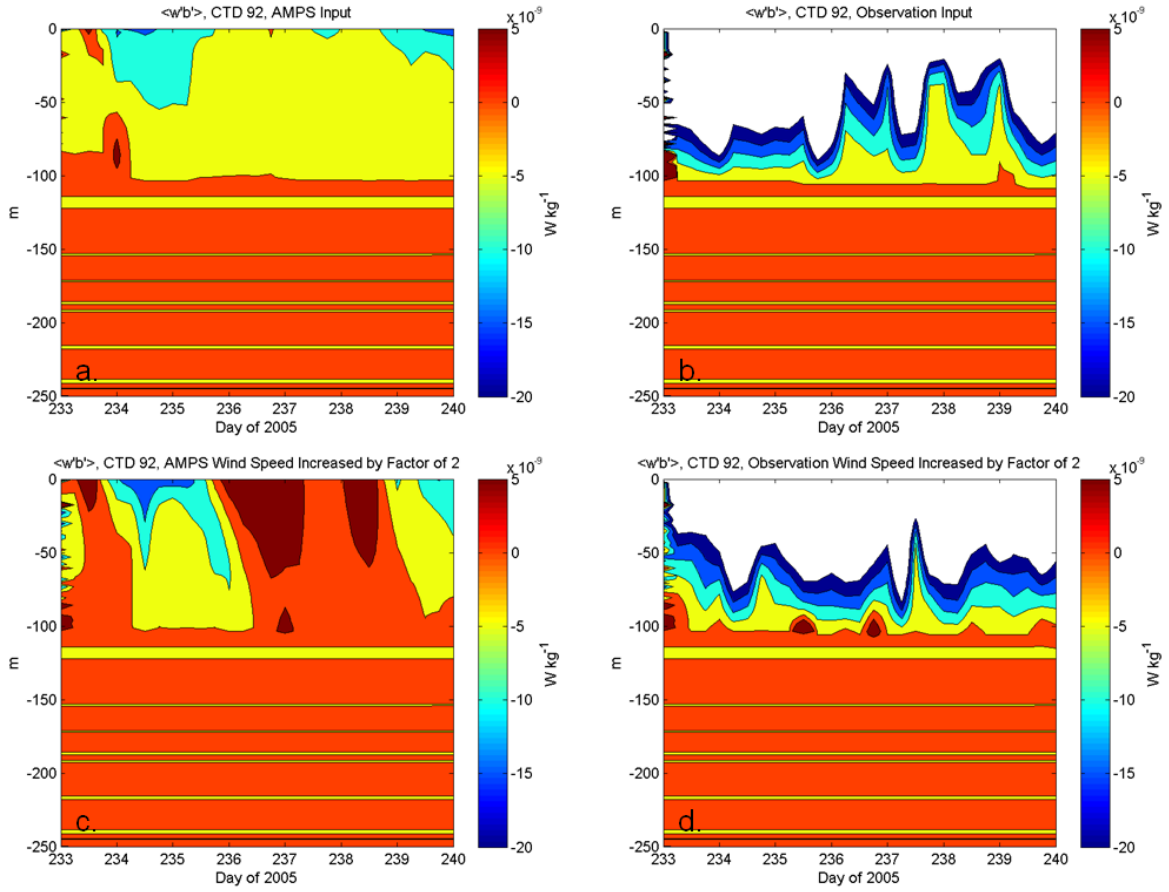

Figure 77. Buoyancy flux (<w'b'>) contour plots from surface to 250 meters at CTD station 92 for Julian days 233 to 240: a.) AMPS forecast, b.) Observed conditions, c.) AMPS forecast wind speed increased by factor of two, and d.) Observed wind speed increased by factor of two (Note white shaded contours are areas of relatively large negative values).

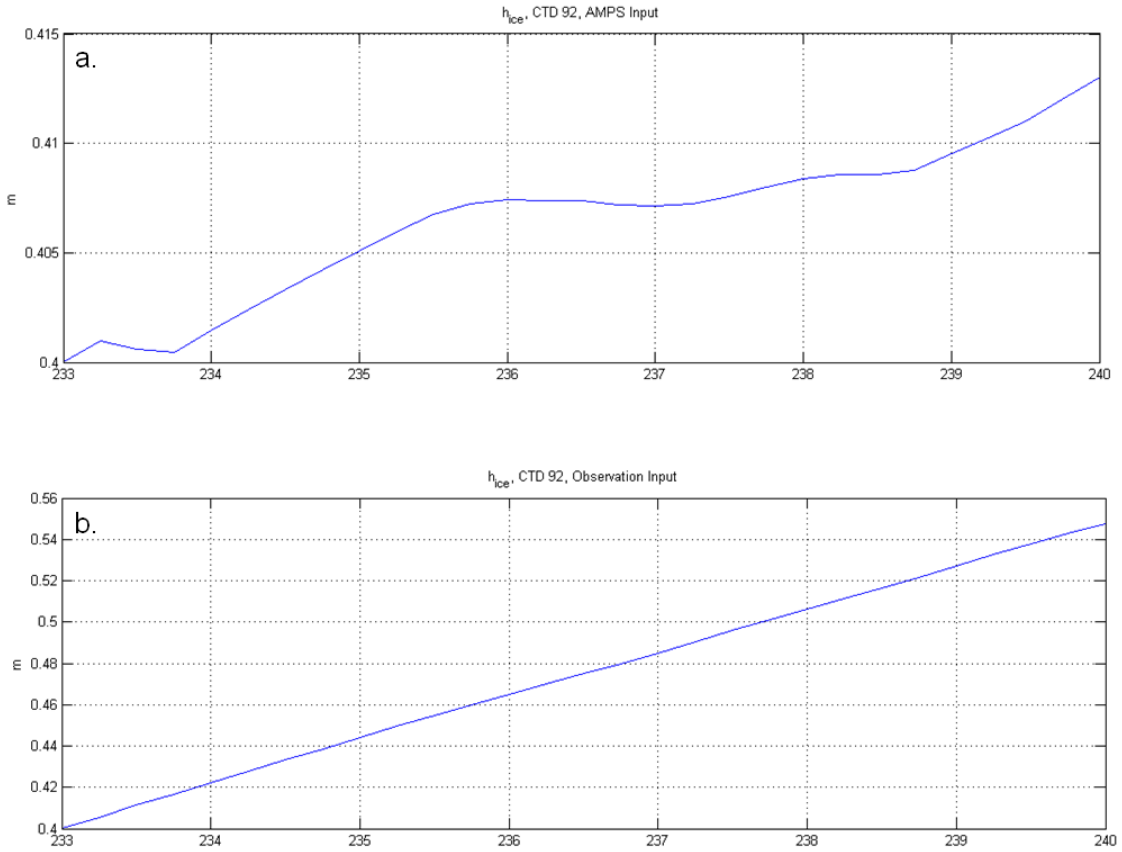

Figure 78. Ocean model predicted ice thickness at CTD station 92, Julian days 233 to 240, for a.) AMPS forecast, and b.) Observed wind forcing conditions.

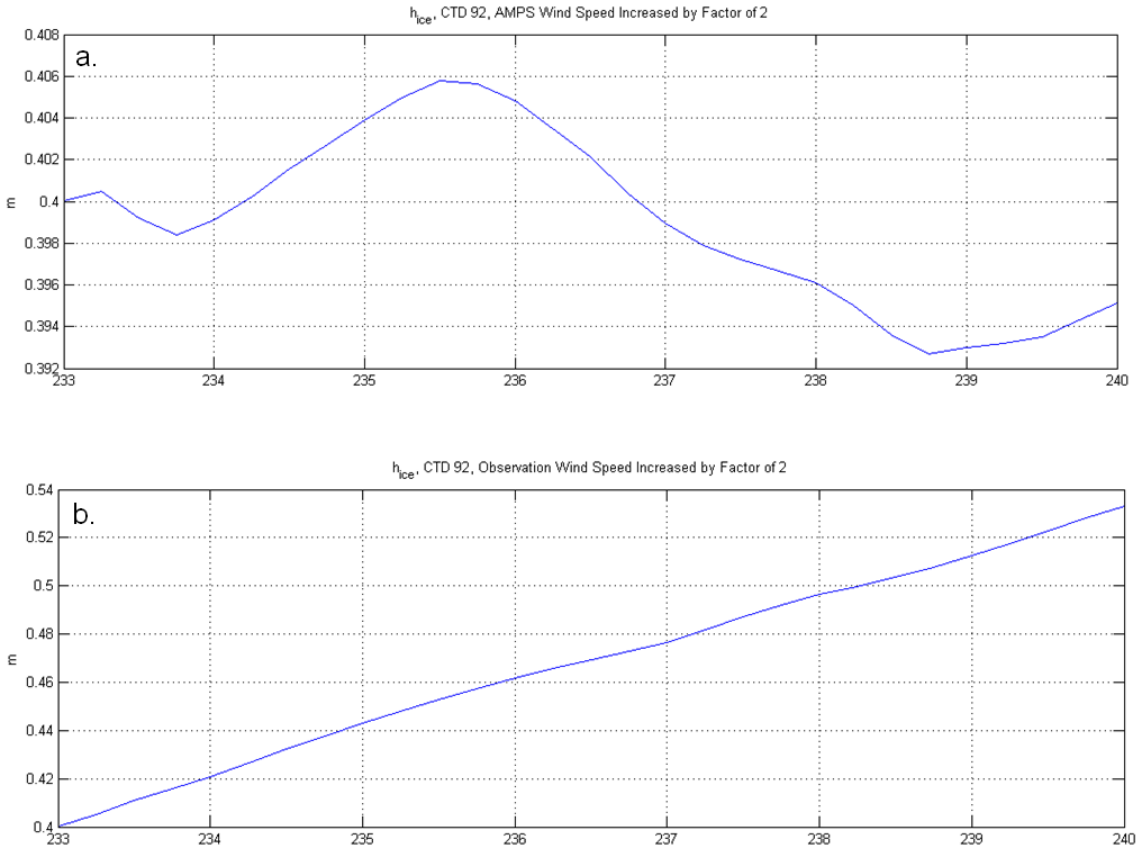

Figure 79. Ocean model predicted ice thickness at CTD station 92, Julian days 233 to 240, for a.) AMPS forecast wind speed increased by factor of two, and b.) Observed wind speed increased by factor of two.

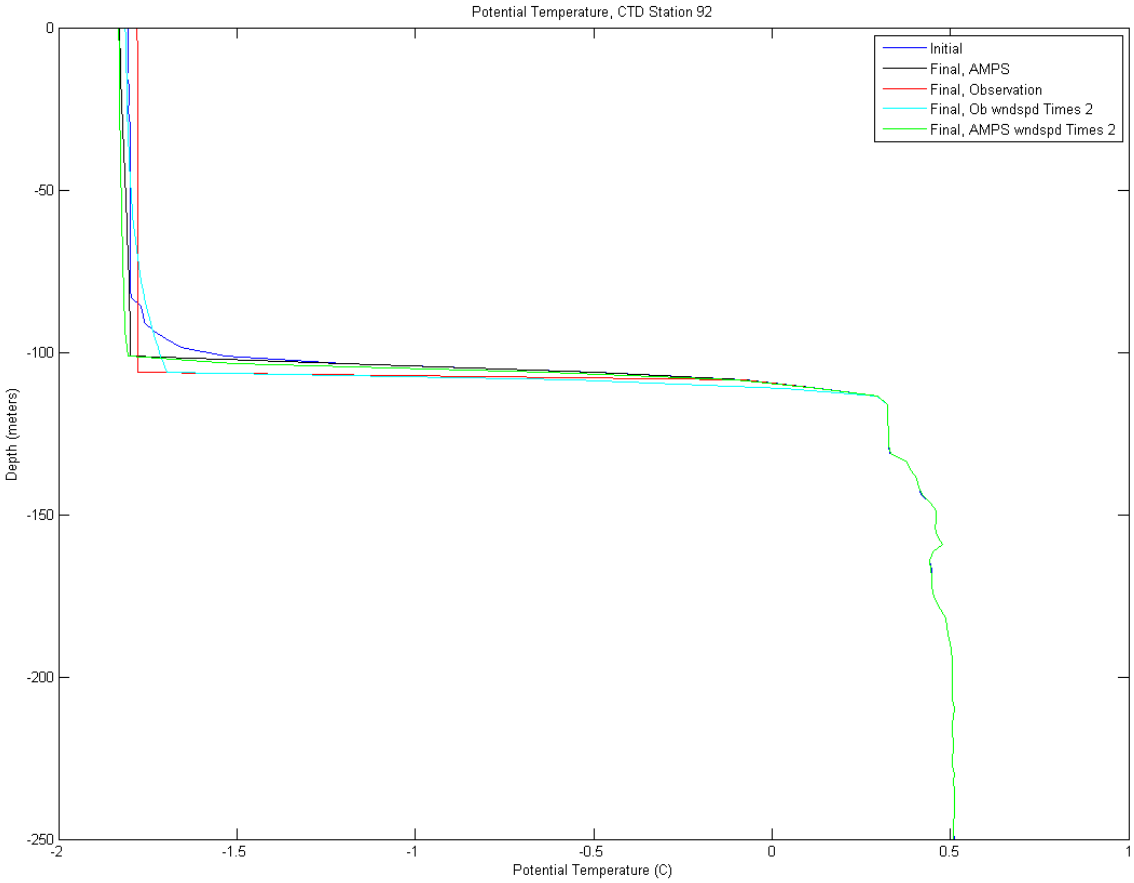

Figure 80. Potential temperature profiles for CTD station 92. Profiles shown are CTD initial (blue), and ocean model prediction seven days later (with AMPS forcing (black), observed forcing (red), AMPS wind speed increased by factor of two (green), and observed wind speed increased by factor of two (cyan)).

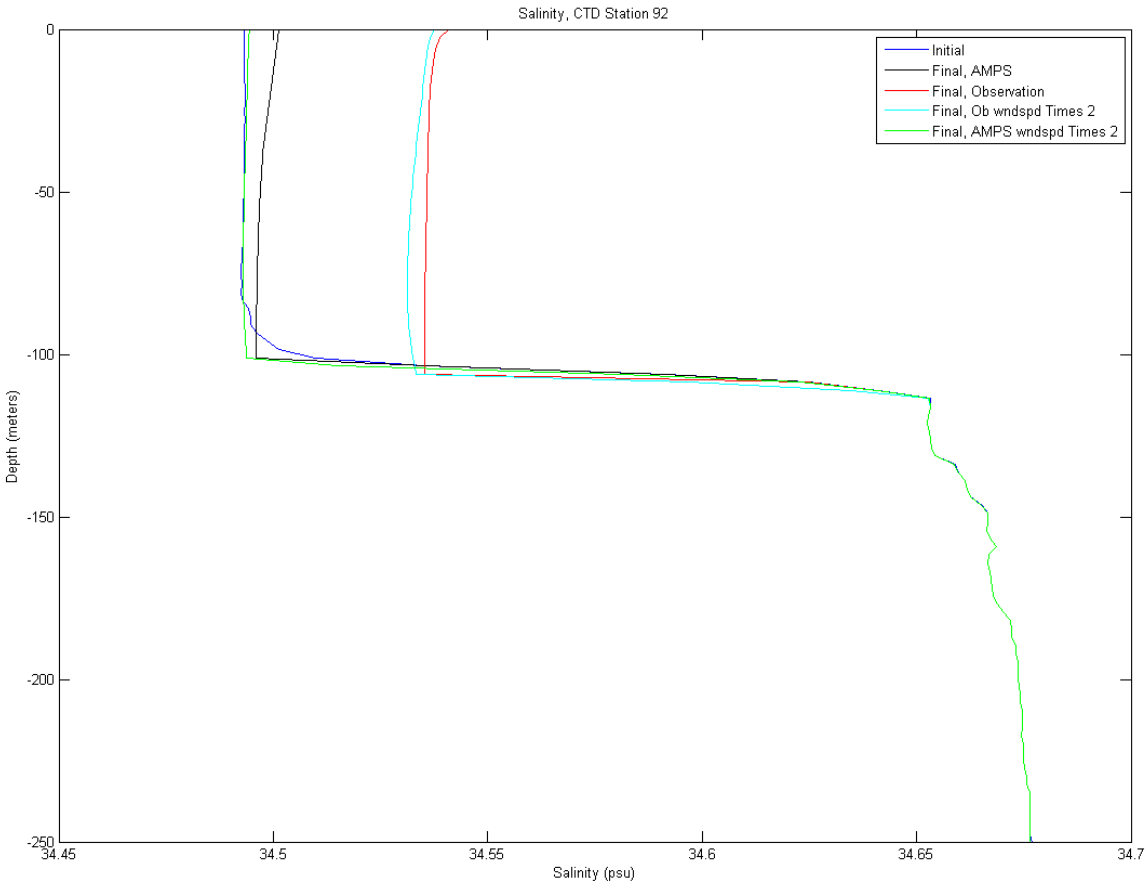

Figure 81. Salinity profiles for CTD station 92. Profiles shown are CTD initial (blue), and ocean model prediction seven days later (with AMPS forcing (black), observed forcing (red), AMPS wind speed increased by factor of two (green), and observed wind speed increased by factor of two (cyan)).

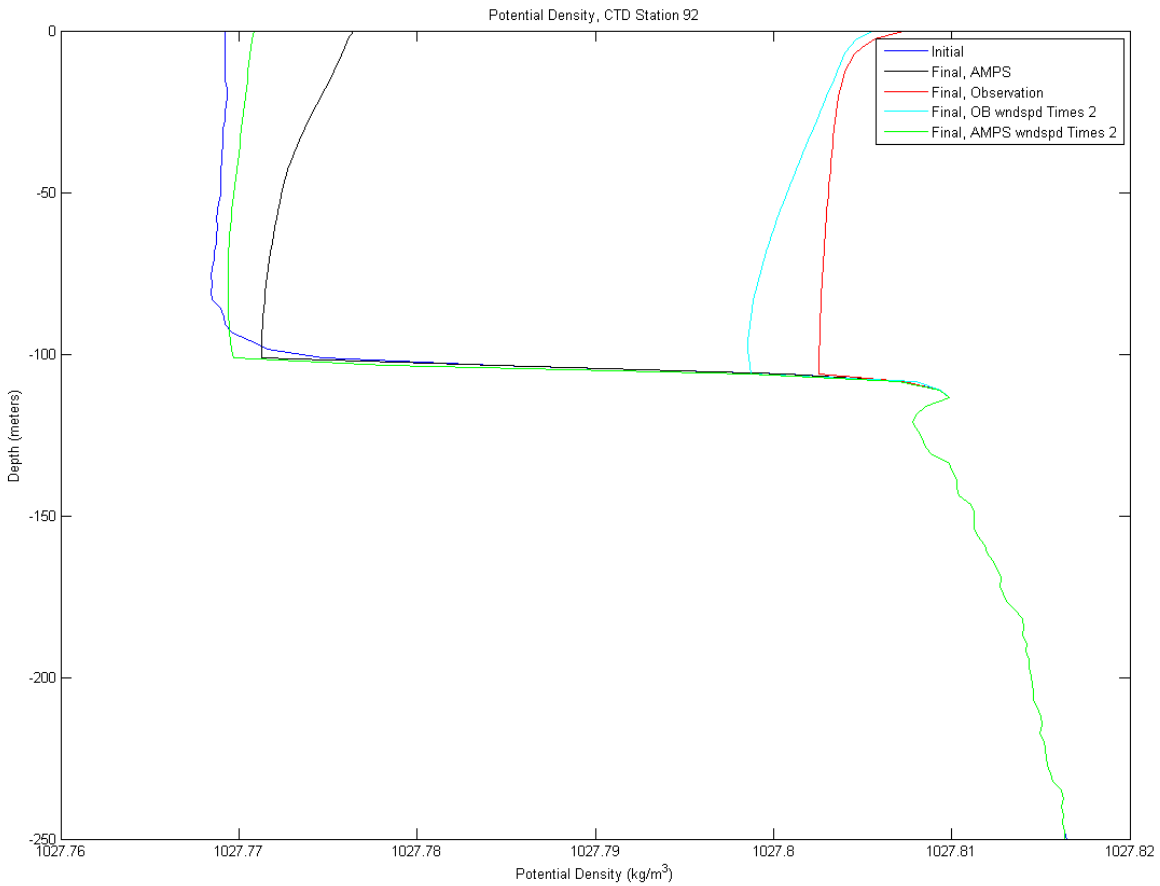

Figure 82. Potential density profiles for CTD station 92. Profiles shown are CTD initial (blue), and ocean model prediction seven days later (with AMPS forcing (black), observed forcing (red), AMPS wind speed increased by factor of two (green), and observed wind speed increased by factor of two (cyan)).

E. OCEAN MODEL CONCLUSIONS

Overall, it was found that observed forcing conditions compared to AMPS forcing conditions (whether actual observed or increased) led to greater change in the water column. The most dramatic example of this was at CTD station 92 (least stable water column), where weak AMPS forcing resulted in nearly no change in the stability, while observed conditions resulted in much more instability. It was also noted that at all three CTD stations, not one of the four scenarios was able to overcome the pycnocline and drive the water column to complete instability.

At CTD station 1, AMPS forecast and observed forcing was found to result in weak temperature fluxes in the water column, allowing for more ice growth. These values were 6 cm for AMPS forcing and 24 cm for observed forcing. The two increased forcing scenarios resulted in stronger temperature fluxes and decrease in ice thickness of 6.5 cm for AMPS increased forcing, and 9.5 cm for observed increased forcing.

At CTD station 65 wind forcing did not result in temperature fluxes strong enough to initiate ice melt. In all scenarios, the ocean model predicted ice thickness increases of 13 cm for AMPS forcing, 15 cm for AMPS increased forcing, 26 cm for observed forcing, and 28 cm for observed increased forcing. While the temperature fluxes did not cause ice melt, for increased forcing scenarios they did serve to limit ice growth, with increased forcing scenario ice thickness only 2 cm more than AMPS and observed.

At CTD station 92, weak AMPS forcing led to weak temperature flux and little to no change in model predicted ice thickness. An increase of only 1 cm was seen for AMPS forcing and decrease of only 0.5 cm for AMPS increased forcing. Both observed scenarios resulted in stronger temperature fluxes, but not enough to promote ice melt. Model predicted ice thickness showed an increase of 15 cm for observed forcing and 13 cm for observed increased forcing.

Average change in potential density difference across the pycnocline at CTD stations 1, 65, and 92 were 0.075 kg/m^3, 0.06 kg/m^3, and 0.04 kg/m^3 respectively. As can be seen in Figure 25, wind speed decreased at each of these stations, with the weakest values at station 92. If forcing at CTD station 92 had been comparable to the other two CTD stations, there is a good possibility that compete instability would have been achieved resulting in overturning of the water column and deep convection.

THIS PAGE INTENTIONALLY LEFT BLANK

IV. CONCLUSION, SUMMARY, AND RECOMMENDATIONS

The purpose of this research was to explore the usefulness of NWP forecast data as an input into a simple ocean model, and the feasibility of using the ocean model output as a planning tool during reactive situations.

The first step to accomplish this was to compare archived AMPS forecast model data with observed conditions during collected during the 2005 MaudNESS deployment to the Maud Rise area in the eastern Weddell Sea. Comparisons consisted of time series and statistical analysis.

AMPS was found to have no skill in forecasting downwelling long wave radiation and relative humidity. It is believed that this was due to poor handling of cloud and moisture parameters. Setting relative humidity with respect to ice to saturation, and converting to relative humidity was found to produce slightly more accurate relative humidity values. It was also noted that AMPS consistently over-forecast near surface air temperature, which led to high values for specific humidity.

AMPS surface pressure, near surface wind speed and direction, and downwelling short wave radiation all performed well. This led to the conclusion that, while there were problems with downwelling long wave radiation and relative humidity, AMPS seemed to well represent the overall synoptic situation.

AMPS latent and sensible heat flux forecast skill is undetermined. This is due to the lack of observed surface temperature which led to the assumption (for bulk methods used to calculate observed heat fluxes) that surface temperature was equal to near surface air temperature. Comparison of AMPS and observed heat fluxes after this assumption resulted in no correlation between the two (with AMPS values appearing to be over-forecast). When AMPS bulk parameters (relative humidity, wind speed, air temperature, and surface pressure) were used to calculate heat fluxes using the bulk method, AMPS and observed values showed some correlation. The AMPS bulk method showed skill in

the latent heat forecast, despite no relative humidity skill, because of the dependence of latent heat flux on specific humidity difference and wind speed, which were predicted by AMPS with skill.

The next step was to use AMPS forecasts and observed conditions as input into a simple one dimensional ocean model. This model was initialized with three different temperature and salinity profiles from CTD casts performed during MaudNESS. CTD station 1 was the farthest away from the Maud Rise and in the most stable water column. CTD station 65 was located over the Rise (in the Taylor column) in a marginally stable water column. The final station was CTD station 92, located to the southwest of the Maud Rise in the "warm pool', and least stable water column.

At every station, observed conditions (both actual and increased) resulted in the least stable ocean model output. The most dramatic example was at CTD station 92, where weak AMPS forcing resulted in almost no change in potential density profile, while observed conditions nearly resulted in eliminating the potential density difference across the pycnocline.

One trend noticed, was the stabilizing effect of ice melt on the water column, particularly in the increased forcing scenarios at CTD stations 1 and 65 shown in Figures 56 - 59 c. and d., 61, 65 - 68 c. and d., and 70. It was found that a strong wind event would begin mixing warm, relatively salty water into the mixed (or upper) layer, resulting in ice melt. The fresh water from the ice melt would then cause the upper layer to decrease in salinity and would curtail mixing, allowing freezing to resume and start the process over.

It was known that a simple one dimensional model could not accurately describe an area with such complicated variability as the Maud Rise region of the Weddell Sea, and was not the purpose of this study. As a sensitivity indicator, the ocean model proved extremely valuable. The utility of such an ocean model using NWP forecast model guidance for short term, reactive situations is entirely feasible, and should be explored for

mid latitude open oceans (for example to study effects on sound speed profiles and ASW applications). For long term situations, or where high accuracy is important, a more complex model would be required.

It is recommended that further studies be conducted on modeled versus observed latent and sensible heat fluxes in polar regions with accurate observed surface temperatures. Also more research should be done on the utility of setting relative humidity with respect to ice to saturation in polar NWP models, which could result in a simpler, cheaper, and more accurate method of calculating relative humidity in a polar environment than current NWP model parameterizations provide

In addition to using the Polar MM5, AMPS is also being run with the Weather Research and Forecasting Model (WRF). If the opportunity presents itself (e.g., additional expeditions to the Maud Rise/Weddell Sea area), similar research should be conducted comparing AMPS WRF to observed conditions.

THIS PAGE INTENTIONALLY LEFT BLANK

LIST OF REFERENCES

Andreas, E. L., P. S. Guest, P. O. G. Persson, C. W. Fairall, T. W. Horst, R. E. Moritz, and S. R. Semmer, 2002: Near-Surface Water Vapor over Polar Sea Ice is Always Near Ice Saturation. *J. Geophys. Res.,* **107,** SHE 8-1 - SHE 8-15

Bromwich, D. H., A. J. Monaghan, K. W. Manning, and J. G. Powers, 2005: Real-Time Forecasting for the Antarctic: An Evaluation of the Antarctic Mesoscale Prediction System (AMPS). *Mon. Wea. Rev.,* **133,** 579-603.

McPhee, M. G., 1992: Turbulent Heat Flux in the Upper Ocean Under Sea Ice. *J. Geophys. Res.,* **97,** 5365-5379.

McPhee, M. G., C. Kottmeier, and J. H. Morison, 1999: Ocean Heat Flux in the Central Weddell Sea During Winter. *J. Phys. Oceanogr.,* **29,** 1166-1179.

McPhee, M. G., 2000: Marginal Thermobaric Stability in the Ice-Covered Upper Ocean over Maud Rise. *J. Phys. Oceanogr.,* **30,** 2710-2722.

Muench, R. D., J. H. Morison, L. Padman, D. Martinson, P. Schlosser, B. Huber, and R. Hohmann, 2001: Maud Rise Revisited. *J. Geophys. Res.,* **106,** 2423-2440.

THIS PAGE INTENTIONALLY LEFT BLANK

INITIAL DISTRIBUTION LIST

1. Defense Technical Information Center
   Ft. Belvoir, Virginia

2. Dudley Knox Library
   Naval Postgraduate School
   Monterey, California

3. Professor Peter S. Guest
   Naval Postgraduate School
   Monterey, California

4. Professor Timothy P. Stanton
   Naval Postgraduate School
   Monterey, California

5. Dr. Miles McPhee
   McPhee Research Company
   Naches, Washington

6. Mr. Kevin Manning
   Mesoscale and Microscale Meteorology Division
   Nation Center for Atmospheric Research
   Boulder, Colorado